SPRINGER BRIEFS IN GEOGRAPHY

Xiaoqiu Chen

Spatiotemporal Processes of Plant Phenology

Simulation and Prediction

Springer

SpringerBriefs in Geography

SpringerBriefs in Geography presents concise summaries of cutting-edge research and practical applications across the fields of physical, environmental and human geography. It publishes compact refereed monographs under the editorial supervision of an international advisory board with the aim to publish 8 to 12 weeks after acceptance. Volumes are compact, 50 to 125 pages, with a clear focus. The series covers a range of content from professional to academic such as: timely reports of state-of-the art analytical techniques, bridges between new research results, snapshots of hot and/or emerging topics, elaborated thesis, literature reviews, and in-depth case studies.

The scope of the series spans the entire field of geography, with a view to significantly advance research. The character of the series is international and multidisciplinary and will include research areas such as: GIS/cartography, remote sensing, geographical education, geospatial analysis, techniques and modeling, landscape/regional and urban planning, economic geography, housing and the built environment, and quantitative geography. Volumes in this series may analyze past, present and/or future trends, as well as their determinants and consequences. Both solicited and unsolicited manuscripts are considered for publication in this series.

SpringerBriefs in Geography will be of interest to a wide range of individuals with interests in physical, environmental and human geography as well as for researchers from allied disciplines.

More information about this series at http://www.springer.com/series/10050

Xiaoqiu Chen

Spatiotemporal Processes of Plant Phenology

Simulation and Prediction

Springer

Xiaoqiu Chen
College of Urban and Environmental Sciences
Peking University
Beijing
China

ISSN 2211-4165 ISSN 2211-4173 (electronic)
SpringerBriefs in Geography
ISBN 978-3-662-49837-8 ISBN 978-3-662-49839-2 (eBook)
DOI 10.1007/978-3-662-49839-2

Library of Congress Control Number: 2016954554

Printed on acid-free paper

This Springer imprint is published by Springer Nature
The registered company is Springer-Verlag GmbH Germany
The registered company address is: Heidelberger Platz 3, 14197 Berlin, Germany

This book is dedicated to my late parents, Guiying Zhang and Zhichun Chen, who nurtured my early interest in plant and nature. It is also a memorial of my 37-year academic career in phenological observation and research.

Foreword

I was honored and delighted when my good friend Xiaoqiu Chen asked me to write the foreword for this book. As a researcher who has devoted my career to studying the interactions of plant life cycle events (phenology) with land surface and atmospheric processes (including the impacts of changing climates on the timing of these seasonal transitions), I have long advocated for the need to develop and better integrate simulations of spatiotemporal processes into biophysical research efforts. Simply stated, in order for phenological research to move forward, we must develop and deploy a "next generation" of more realistic phenological models, especially at continental scales.

In recent years, there has been a growing realization that integration of spatial and temporal variations into new phenological models is essential. Xiaoqiu has done an excellent job in this volume by providing a comprehensive overview of cutting-edge techniques useful for building and integrating phenological models from both plant-based and remote sensing data at multiple scales. Such information will prove to be an invaluable platform for advancing future global change and large-scale ecological research. Thus, I anticipate adding this volume to my personal technical reference library and look forward to consulting it often in the years ahead. I also expect that new students and established phenological scholars will want to do the same.

September 2016

Mark D. Schwartz
Distinguished Professor of Geography
University of Wisconsin-Milwaukee
Milwaukee WI, USA

Acknowledgements

I would especially like to thank Prof. Guodong Yang, who leaded me into the field of phenology in 1979. My graduate students, Weiqi Zhang, Weiguang Lang, and Xiaofang Yang, digitized the phenological records at the Beijing Botanical Garden and drew the illustrations. I am also very thankful to Prof. Mark Schwartz at the University of Wisconsin–Milwaukee, for reviewing and editing the manuscript. This work was funded by the National Natural Science Foundation of China under grant nos 49771076, 40371042, 40671028, 40871029, 41071027, and 41471033.

Contents

Chapter 1
Plant Phenology of Natural Landscape Dynamics

Abstract From the perspectives of natural landscape dynamics, plant phenology is the study of the timing (and quantity) of annually recurring plant growth and reproductive phenomena, as well as the drivers of these events associated with endogenous and exogenous forces. Conventional plant phenology usually serves as time steps and markers of vegetation growth and reproductive processes within a year and among different years, while modern plant phenology can serve as a key link between climate change and biogeochemical cycles at seasonal and interannual scales.

Keywords Natural landscape dynamics · Phenological phenomena · Plant phenology · Integrative indicator · Key link between climate change and biogeochemical cycles

1.1 Phenological Phenomena and Plant Phenology

In China, one of the earliest phenological records appeared in "The Book of Poetry" during 1100 to 600 B.C. It said that "polygala seed matures in April, cicada sings in May, beating the jujube in August, reaping the rice in October" (Yu 2012). Here, "polygala seed maturity", "cicada sing", "beating the jujube", and "reaping the rice" are all phenological phenomena. Their occurrences have obvious periodicity and rhythmicity. Thus, phenological phenomena can be defined as annually recurrent and macroscopic natural and human phenomena on the Earth's surface. According to their properties, phenological phenomena include: (1) abiotic phenomena, such as frost, snow, soil freezing-thawing, river and lake freezing-melting, thunder, lightning, etc.; (2) biotic phenomena, such as budburst, leaf unfolding, flowering, fruit or seed maturing and shedding, leaf coloration, leaf fall of plants, and first and last observance or singing of birds, insects and other animals, etc.; and (3) human life phenomena, such as farming activities, seasonal tours and sightseeing, seasonal allergic disease and epidemic disease, etc. These phenological phenomena interact and are interrelated. Their occurrence reflects not only the current status, but also

X. Chen, *Spatiotemporal Processes of Plant Phenology*,
SpringerBriefs in Geography, DOI 10.1007/978-3-662-49839-2_1

the accumulation state of environmental conditions, especially weather and climate conditions over a past time period. Thus, phenological phenomena can be regarded as sensitive indicators and integrators of natural landscape dynamics.

Plant phenology is the study of the timing (and quantity) of annually recurring plant growth and reproductive phenomena, as well as the drivers of these events associated with endogenous and exogenous forces. Within a year, the timing and quantity of plant phenological phenomena show distinct seasonality. With regard to plant phenology of ecosystem processes, studies deal with individual plants, populations, and communities. From the perspectives of natural landscape dynamics, the field of study also includes different spatial scales, namely local, regional, hemispherical, and global scales. Therefore, plant phenology provides a unified measure of the timing and quantity of plant growth and reproductive phenomena at different vegetation units and spatial scales. A central purpose of plant phenological studies is to discover temporal rhythmicity and spatial patterns within the timing and quantity of plant phenological phenomena, as well as their physical, chemical and biological mechanisms. Basic tasks of plant phenological studies include the following aspects: (1) observing and recording the timing and quantity of plant phenological phenomena visually, as well as with digital camera, and satellite remote sensing, etc.; (2) examining and correcting visual phenological records, as well as phenological data from photography and satellite remote sensing; (3) revealing spatiotemporal characteristics of the timing and quantity of plant phenological phenomena and their endogenous and exogenous causes; and (4) simulating and predicting spatiotemporal patterns of the timing and quantity of plant phenological phenomena.

1.2 Integrative Indicator of Natural Landscape Dynamics

Natural landscape dynamics include circadian rhythms, seasonal rhythms, circannual rhythms and multi-year rhythms. Because vegetation is the integrative indicator of natural landscape features, plant phenology becomes the integrative indicator of natural landscape dynamics at seasonal and interannual scales. Conventional plant phenology usually serves as time steps and markers of vegetation growth and reproductive processes within a year and among different years, which are mainly controlled by various environmental factors, especially temperature, water availability, and photoperiod. At local scales, phenological occurrence dates of individual plants and communities can indicate seasonal rhythms of the natural landscape. Using phenological observation data from the Beijing Botanical Garden, twelve phenological seasons were identified by means of frequency and cumulative frequency thresholds of plant phenological occurrence dates in every five-day period throughout the year (Chen and Cao 1999). Each phenological season represents a specific seasonal aspect stage of the natural landscape, which has typical seasonal aspect characteristics and indicative phenophases (Table 1.1). At regional and global scales, vegetation phenological timing metrics based on

Table 1.1 Phenological seasons, seasonal aspect characteristics and indicative phenophases at the Beijing Botanical Garden (1979–1987; Yang and Chen 1995)

Phenological seasons	Average start–end date (m/d)	Seasonal aspect characteristics	Indicative phenophases at the start of seasons
Early spring	2/25–3/21	Grass green-up and tree budburst	Budburst of *Populus tomentosa*
Midspring	3/22–4/30	Flowers blooming in a riot of color	First flowering of *Jasminum nudiflorum*
Late spring	5/1–5/15	Flourishing leaves and withering flowers	50 % leaf unfolding of *Paulownia tomentosa*
Early summer	5/16–6/14	Prosperous flowers with green leaves	First flowering of *Aesculus chinensis*
Midsummer	6/15–8/8	A few red flowers in the midst of thick foliage	First flowering of *Campsis radicans*
Late summer	8/9–9/2	Dark green canopy but lack of flowers	The end of the flowering of *Vitex negundo* var. heterophylla
Early autumn	9/3–9/27	Autumn leaf coloring and rich fruit ripening	Fruit maturing of *Syringa pekinensis*
Midautumn	9/28–10/17	Gorgeous leaf coloring and leaf fall starting	First leaf coloration of *Forsythia suspensa*
Late autumn	10/18–11/21	Falling leaves rustling in the wind	First leaf fall of *Populus alba*
Early winter	11/22–12/6	Withered leaves	The end of leaf fall of *Salix matsudana* var. tortuosa
Midwinter	12/7–2/4[a]	Bare canopy of deciduous trees	The end of leaf fall of *Chimonanthus praecox*
Late winter	2/5[a]–2/24[a]	Spring signal appearance	Bud swelling of *Chimonanthus praecox*

[a]Date of the next year

satellite sensor-derived vegetation indices can also display seasonal rhythms of the natural landscape (Myneni et al. 1997; Zhang et al. 2003).

In addition, plant phenology can serve as a key link between climate change and biogeochemical cycles at seasonal and interannual scales. It is well known that the vegetation growing season is usually defined as the number of days between the budburst/leaf unfolding date in spring and the leaf coloration/leaf fall date in autumn (Chen and Xu 2012). Thus, plant phenological occurrence dates are crucial biological indices for determining growing season start and end dates. Over recent decades, scientists have found new relevance for phenological studies related to global climate change. In terms of interactions among terrestrial biological processes and atmospheric physical processes, since vegetation growing season start and end dates are mainly influenced by seasonal thermal and moisture conditions, they are regarded as sensitive, easily observable, and integrative indicators of rapid ecosystem responses to climate change (Chen 1995; Menzel and Fabian 1999).

On the other hand, vegetation growing season duration represents the green leaf period to a certain extent and therefore, its variation could regulate land surface temperature and moisture regimes by altering albedo, latent and sensible heat exchange, and turbulence, etc. (Schwartz 1996; Peñuelas et al. 2009). Considering interactions among terrestrial biological processes and atmospheric chemical processes, variation in the vegetation growing season influence the seasonal pattern of atmospheric CO_2 concentrations (Keeling et al. 1996) and the total annual emission of biogenic volatile organic compounds (BVOCs, Peñuelas et al. 2009), which contribute to many complex processes associated with global climate change. Further, elevated CO_2 might also influence the vegetation growing season, for example by delaying flowering and greening in grasses (Cleland et al. 2006). Based on the above evidence, variation in the vegetation growing season may influence thermal and moisture regimes, seasonal carbon cycle and aerosol formation, etc., by coupling physical, chemical and biological processes among land surfaces and the atmosphere. Therefore, revealing spatiotemporal patterns of the vegetation growing season at regional scales would be helpful for assessing responses and feedbacks of vegetation dynamics to climate change.

Overall, because the vegetation growing season is approximately equivalent to the photosynthetic period, carbon-uptake period, and transpiration period (Barr et al. 2009), climate change induced vegetation growing season shifts may influence the exchange capacities of carbon, water, and energy among land surfaces and the atmosphere, and consequently result in ecosystem productivity variations. The former in turn will affect the global carbon balance and climate change (Fig. 1.1).

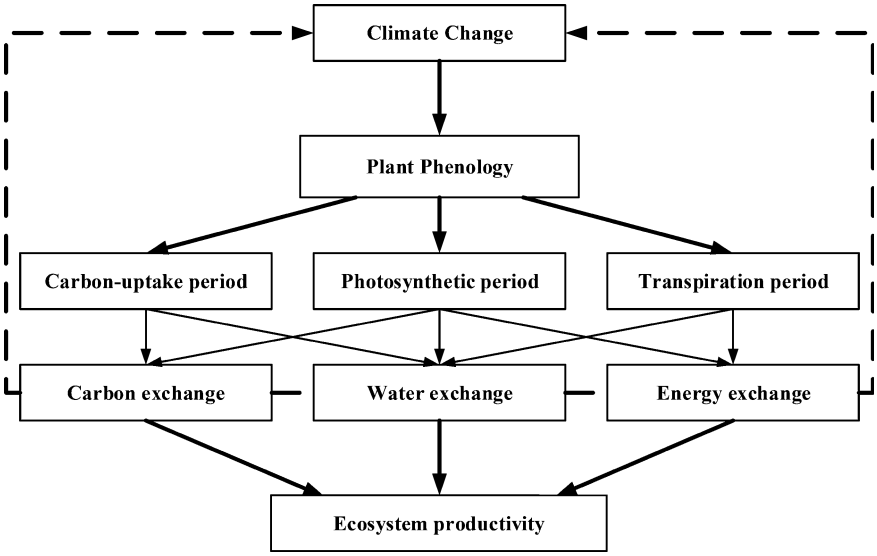

Fig. 1.1 Interrelationship among plant phenology, climate change, biogeochemical cycles, and ecosystem productivity

References

Chen XQ (1995) Phänologische und klimatologische Raumgliederung Westdeutschlands. Geogr Runds 47:312–317

Chen X, Cao Z (1999) Frequency distribution pattern of plant phenophases and its application to season determination (in Chinese). Sci Geogr Sin 19(1):21–27

Chen XQ, Xu L (2012) Phenological responses of *Ulmus pumila* (Siberian Elm) to climate change in the temperate zone of China. Int J Biometeorol 56:695–706

Cleland EE, Chiariello NR, Loarie SR, Mooney HA, Field CB (2006) Diverse responses of phenology to global changes in a grassland ecosystem. Proc Natl Acad Sci USA 103:13740–13744

Barr A, Black TA, McCaughey H (2009) Climatic and phenological controls of the carbon and energy balances of three contrasting boreal forest ecosystems in western Canada. In: Noormets A (ed) Phenology of ecosystem processes: Applications in global change research. Springer, Dordrecht, pp 3–34

Keeling CD, Chin JFS, Whorf TP (1996) Increased activity of northern vegetation inferred from atmospheric CO_2 measurements. Nature 382:146–149

Menzel A, Fabian P (1999) Growing season extended in Europe. Nature 397:659

Myneni RB, Keeling CD, Tucker CJ, Asrar G, Nemani RR (1997) Increased plant growth in the northern high latitudes from 1981 to 1991. Nature 386:698–702

Peñuelas J, Rutishauser T, Filella I (2009) Phenology feedbacks on climate change. Science 324:887–888

Schwartz MD (1996) Examining the spring discontinuity in daily temperature ranges. J Clim 9:803–808

Yang G, Chen X (1995) Phenological calendars and their applications in the Beijing area (in Chinese). Capital Normal University Press, Beijing

Yu GY (2012) Selected poems from the Book of Poetry (in Chinese). Zhonghua Book Company, Beijing

Zhang X, Friedl MA, Schaaf CB, Strahler AH, Hodges JCF, Gao F, Reed BC, Huete A (2003) Monitoring vegetation phenology using MODIS. Remote Sens Environ 84:471–475

Chapter 2
Temporal Rhythmicity of Plant Phenology

Abstract Plant phenological observations show that plant growth and reproduction obey a certain temporal rhythmicity, which is a macroscopic and integrative reflection of local and regional natural landscape dynamics. The most obvious temporal rhythmicities of plant phenology are displayed as sequential and correlative rhythm, circannual rhythm, multi-year rhythm, circadian rhythm, and overlap rhythm. Temporal rhythmicity of plant phenology is mainly attributed to climatic rhythmicity, photoperiod, and response properties of phenological phenomena to weather and climate.

Keywords Sequential and correlative rhythm · Circannual rhythm · Multi-year rhythm · Circadian rhythm · Overlap rhythm

2.1 Sequential and Correlative Rhythm

Plant phenology sequential and correlative rhythm is defined as follows:

> The occurrence dates of various plant phenological phenomena obey a certain time sequence within a year, and synchronously advance or postpone among years.

The time sequence depends highly on geographical locations and specific plant communities. External causes of the sequential and correlative rhythm of plant phenology are seasonal insolation induced weather and climatic seasonal rhythms, including temperature, precipitation, photoperiod, humidity, wind, etc. These meteorological factors evolve along the time sequence within a year and fluctuate among years, which form the environmental background of sequential and correlative rhythm of plant phenology. With regard to plant phenological adaptation and response to climate change, if a species is to thrive and extend its range in a certain region, it must be able to coordinate its life cycle with the progression of periodic phenomena in its environment (Larcher 1975). Because a plant phenological phenomenon occurrence reflects the accumulation of environmental conditions (especially weather and climatic conditions) over a past time period, continuous accumulation of climatic variables along the time sequence will subsequently

X. Chen, *Spatiotemporal Processes of Plant Phenology*,
SpringerBriefs in Geography, DOI 10.1007/978-3-662-49839-2_2

trigger occurrence of various phenological phenomena. Sequential and correlative rhythm can be statistically expressed by correlation coefficient as follows:

$$r = \frac{\sum_{i=1}^{n}(x_i - \overline{x})(y_i - \overline{y})}{\sqrt{\sum_{i=1}^{n}(x_i - \overline{x})^2}\sqrt{\sum_{i=1}^{n}(y_i - \overline{y})^2}}$$

where x_i and y_i denote the occurrence dates of two arbitrary phenophases in year i; $\bar{x}$ and $\bar{y}$ denote the multi-year mean occurrence dates of the two phenophases; n is the number of years. If x_i and y_i have significant positive correlation, sequential and correlative rhythm exists between them. The larger the correlation coefficient is, the stronger the sequential and correlative rhythm is. Contrarily, if they have non-significant positive correlation, only sequential rhythm but not correlative rhythm exists between them. Table 2.1 and Fig. 2.1 show an example of sequential and correlative rhythm of plant phenology in the Beijing Botanical Garden. Other examples of sequential and correlative rhythm of plant phenology have also been reported in Germany (Pfau 1964; Menzel 2003). Generally speaking, as the time interval between two phenological occurrence dates expands, sequential and correlative rhythm may become weaker due to the decrease of continuity of weather processes influencing the two phenological occurrence dates (Fig. 2.2).

2.2 Circannual Rhythm

Plant phenology circannual rhythm can be expressed as:

> The occurrence dates of various plant phenological phenomena have a recurrence interval of approximate one year.

Table 2.1 Correlation coefficients between first flowering dates in the Beijing Botanical Garden (1979–2013)

Species	*Pd*	*Fs*	*Md*	*Cs*	*So*	*Rx*	*Pp*
Jn	0.826*	0.803*	0.780*	0.636*	0.661*	0.703*	0.546*
Pd		0.766*	0.805*	0.572*	0.697*	0.669*	0.494*
Fs			0.823*	0.589*	0.736*	0.720*	0.551*
Md				0.658*	0.819*	0.770*	0.653*
Cs					0.641*	0.715*	0.731*
So						0.613*	0.644*
Rx							0.739*

Data source Personal field observations conducted by Xiaoqiu Chen and Guodong Yang
*$P < 0.01$
Jn: *Jasminum nudiflorum*; *Pd*: *Prunus davidiana*; *Fs*: *Forsythia suspensa*; *Md*: *Magnolia denudata*; *Cs*: *Chaenomeles speciosa*; *So*: *Syringa oblata*; *Rx*: *Rosa xanthina*; *Pp*: *Philadelphus pekinensis*

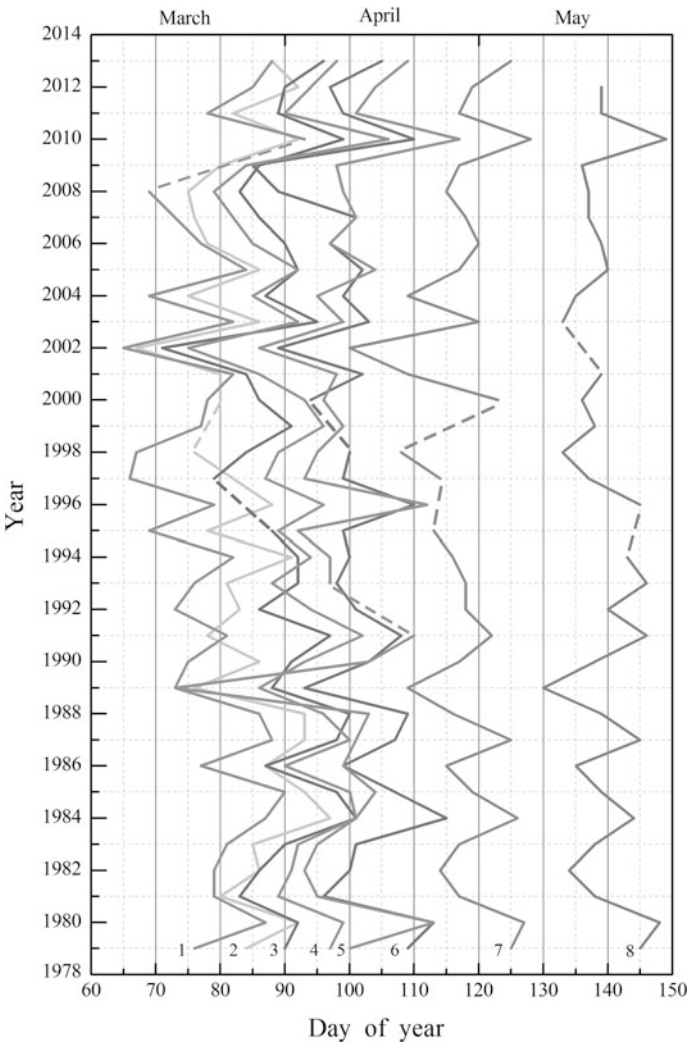

Fig. 2.1 Plots of sequential and correlative rhythm of the first flowering dates in the Beijing Botanical Garden (1979–2013). *1 Jasminum nudiflorum*; *2 Prunus davidiana*; *3 Forsythia suspensa*; *4 Magnolia denudata*; *5 Chaenomeles speciosa*; *6 Syringa oblata*; *7 Rosa xanthina*; *8 Philadelphus pekinensis* (*Data source* Personal field observations conducted by Xiaoqiu Chen and Guodong Yang)

Since the recurrence interval is usually less dependent on geographical locations and specific plant species, circannual rhythm is the essential characteristic of plant phenological phenomena. External causes of plant phenology's circannual rhythm are the Earth's revolution-induced weather and climatic annual cycles, including temperature, precipitation, photoperiod, humidity, wind, etc. Circannual rhythm of plant phenology can be measured by multi-year mean value ($\bar{x}$), standard deviation

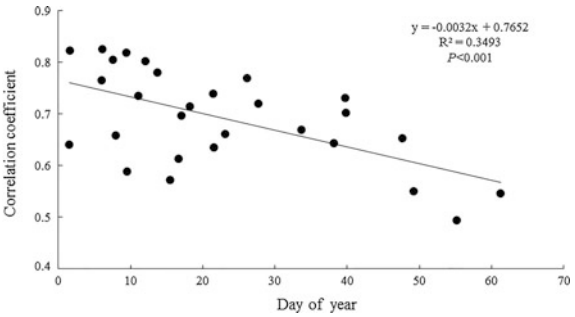

Fig. 2.2 Relationship between correlation coefficient and corresponding average time interval among first flowering dates

(*SD*), and range (*R*; difference between maximum value and minimum value) of the recurrence interval. Table 2.2 shows circannual rhythm of individual plant phenophases in the Beijing Botanical Garden. On average, the recurrence intervals of all plant phenophases are about 365 days, and the standard deviation (SD) of the recurrence intervals display a decreasing tendency from midspring to early summer. Namely, circannual rhythm of plant phenology is stronger for later phenophases than earlier phenophases in the first half-year.

Further statistical analysis indicated that the first date for the daily mean air temperature to steadily pass 0, 5, and 10 °C characterizes also circannual rhythm (Table 2.3). It is worth noting that the mean recurrence intervals are also about 365 days, but the SD and R values of the recurrence intervals are much larger than those of spring plant phenology. This shows that circannual rhythm of spring plant phenology can reflect annual cycle of threshold daily mean air temperatures to a large extent, and spring plant phenology is a more stable indicator in displaying circannual rhythm of natural landscape dynamics than air temperature.

2.3 Multi-year Rhythm

Multi-year rhythm of plant phenology means that long time series of some plant phenological occurrence dates have a quasi-periodicity over one year. That is, notably early or late years in plant phenological occurrence dates appear at regular intervals. It should be noted that this kind of rhythm is not strictly periodic and depends highly on geographic location, time series length, and plant species. So far, the most famous example in plant phenology multi-year rhythm was reported by Margary (1926). He analyzed the annual mean flowering and leafing dates of seven plants from the Marsham phenological record (over 1736–1925 in Norfolk, England), and found the mean periods between early years or late years were 12.2 years for unsmoothed time series and 12.1 years for smoothed time series. Further analysis indicated that flowering and leafing dates and mean temperature during January to May showed an apparent correlation between earliness/lateness and warmness/coldness, and similar mean periods between 11.8 and 12.2 years. In addition, the flowering and leafing dates and sunspot numbers showed a moderate

Table 2.2 Circannual rhythm of the first flowering dates from midspring to early summer in the Beijing Botanical Garden (1979–2013)

Period	*Jn*	*Pd*	*Fs*	*Md*	*Cs*	*So*	*Rx*	*Pp*
1979–1980	376	373	367	367	378	369	367	368
1980–1981	358	354	357	356	349	349	356	356
1981–1982	365	371	368	367	362	369	362	361
1982–1983	367	364	369	366	367	366	368	369
1983–1984	371	377	376	374	371	–	374	371
1984–1985	369	362	363	365	369	–	359	361
1985–1986	352	359	354	355	360	357	361	361
1986–1987	376	371	376	375	367	373	375	375
1987–1988	363	365	367	361	367	367	356	359
1988–1989	353	349	354	356	–	350	359	–
1989–1990	367	375	368	372	–	375	373	–
1990–1991	371	357	371	374	372	370	370	373
1991–1992	357	370	354	357	–	358	361	359
1992–1993	369	364	372	360	–	363	366	372
1993–1994	371	375	365	371	365	367	363	362
1994–1995	352	352	361	360	360	364	362	–
1995–1996	375	375	–	372	385	376	–	–
1996–1997	353	360	–	357	347	355	–	358
1997–1998	366	359	370	367	367	366	359	361
1998–1999	375	–	372	372	369	–	–	370
1999–2000	366	–	360	362	362	–	–	363
2000–2001	370	366	364	359	368	374	352	369
2001–2002	348	–	–	–	353	352	–	–
2002–2003	382	–	–	–	378	379	–	–
2003–2004	352	354	357	358	361	361	354	367
2004–2005	381	377	371	373	375	369	374	371
2005–2006	358	357	363	358	358	360	368	364
2006–2007	361	363	361	362	369	369	363	363
2007–2008	361	364	362	362	363	353	362	365
2008–2009	–	371	369	371	365	–	368	365
2009–2010	–	377	378	–	–	–	376	–
2010–2011	–	355	355	–	–	354	354	–
2011–2012	372	375	366	369	368	363	367	365
2012–2013	369	362	372	370	371	374	372	–
$\bar{x}$ (days)	365.4	365.1	365.4	364.9	365.9	364.4	364.3	365.1
SD (days)	9.0	8.3	6.8	6.4	8.2	8.3	6.8	5.1
R (days)	34	28	24	20	38	30	24	19

Data source Personal field observations conducted by Xiaoqiu Chen and Guodong Yang
Jn: *Jasminum nudiflorum*; *Pd*: *Prunus davidiana*; *Fs*: *Forsythia suspensa*; *Md*: *Magnolia denudata*; *Cs*: *Chaenomeles speciosa*; *So*: *Syringa oblata*; *Rx*: *Rosa xanthina*; *Pp*: *Philadelphus pekinensis*

Table 2.3 Mean recurrence interval and its variation of the first date for the daily mean air temperature to steadily pass 0, 5, and 10 °C in Beijing (1979–2013)

Statistical indicator	First date ≥ 0 °C	First date ≥ 5 °C	First date ≥ 10 °C
$\bar{x}$ (days)	365.7	365.2	365.1
SD (days)	14.1	13.5	8.8
R (days)	57	49	37

connection between earliness and maximum in nine times of fifteen and between lateness and minimum at the same degree. The period of sunspot numbers was 11.2 years. Nowadays, spectrum analysis and wavelet analysis are usually used for identifying phenological periodicity. A singular spectrum analysis has been implemented to delineate periodicity of flowering dates of four eucalypt species from 1940 to 1971 in Australia and a 4-year cycle was detected in *Eucalyptus tricarpa* (Hudson and Keatley 2010). Using first flowering time series of the eight plant species in the Beijing Botanical Garden from 1979 to 2013 (Fig. 2.1), a wavelet analysis was carried out for identifying the multi-year rhythm. Results showed that a 12-year major cycle exists in these phenological time series (Fig. 2.3), which is coincident with the major cycle in average air temperature during March to May in Beijing. Thus, multi-year rhythm of spring plant phenology can reflect periodic variation of air temperature to a certain extent.

2.4 Circadian Rhythm

Plant phenology circadian rhythm can be described as follows:

> The occurrence time of some plant phenological phenomena show a recurrence interval within 24 h at a specific site, which reflects the effect of photoperiod on plant phenological phenomena.

Studies showed that some leguminous plants and their seedlings open their leaves during the day and close them at night (Piltz and Bever 1970). Carolus Linnaeus (1707–1778) found that flowers of some plants opened and closed periodically at different hours of the day and that these times varied from species to species. Thus, he proposed a flower clock to show the time. Namely, cultivating these plants in a round flower bed according to time sequence of flowering within a day, they constituted a kind of flower clock (Riedman 1982; Foster and Kreitzman 2004). The flower clock was a garden plan hypothesized by Carolus Linnaeus, which would take advantage of several plants that open or close their flowers at particular times of the day to accurately indicate the time. Nevertheless, although many plants exhibit a strong circadian rhythm, few have been observed to open their flowers at a precise solar time. Therefore, the accuracy of such a clock is diminished because flowering time is also affected by weather and seasonal factors. In addition, the flowering times recorded by Linnaeus would also be subject to differences in daylight due to latitude (Gardiner 1987).

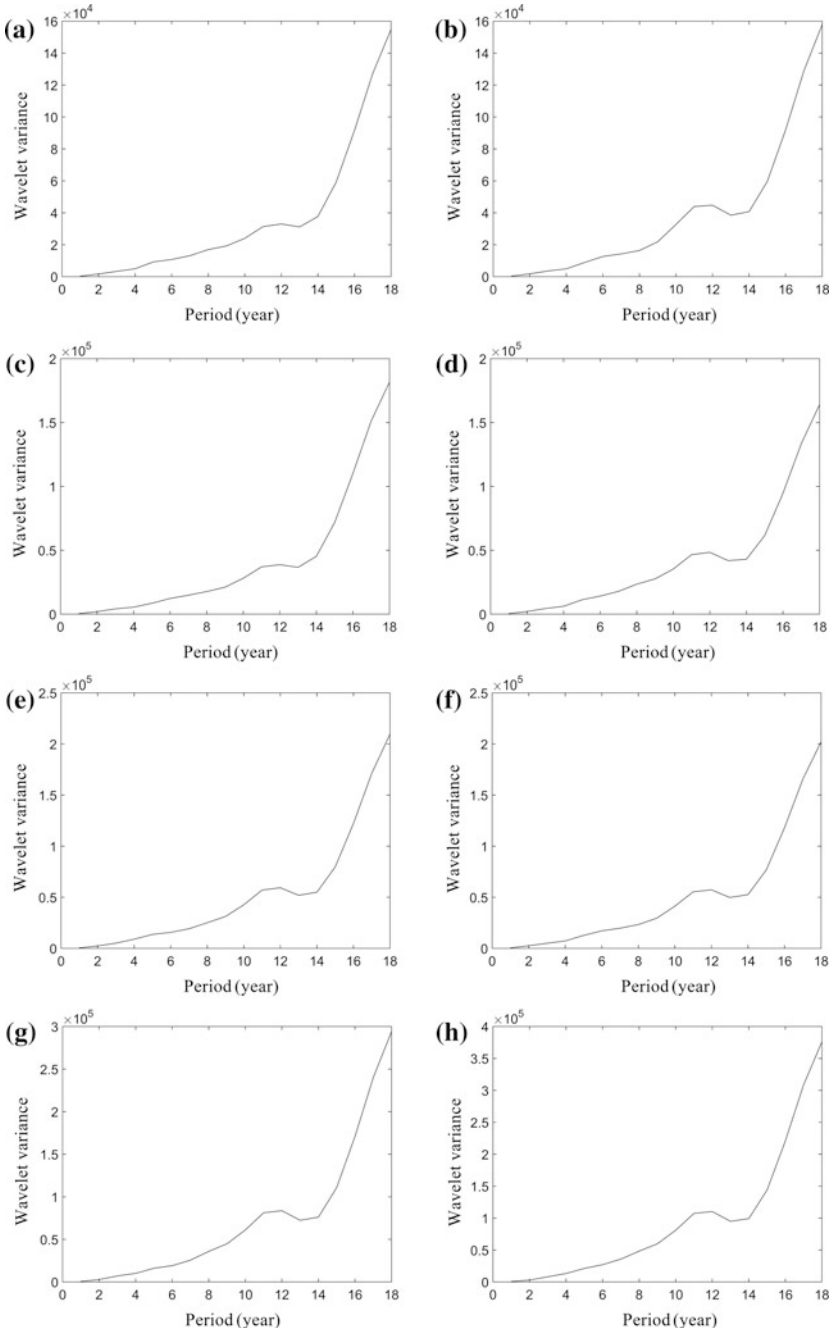

Fig. 2.3 Wavelet variance diagram of the first flowering dates in the Beijing Botanical Garden. **a** *Jasminum nudiflorum*; **b** *Prunus davidiana*; **c** *Forsythia suspensa*; **d** *Magnolia denudata*; **e** *Chaenomeles speciosa*; **f** *Syringa oblata*; **g** *Rosa xanthina*; **h** *Philadelphus pekinensis*

2.5 Overlap Rhythm

Plant phenology overlap rhythm means that some plant phenological phenomena occur roughly at the same time each year. The biological cause of overlap rhythm is that occurrence of the overlapping phenological phenomena needs approximately the same amount of accumulation of environmental conditions. Plant phenology overlap rhythm can be measured by comparing average occurrence dates, standard deviations, and the earliest and latest occurrence dates of two or more phenophases. Obviously, the smaller the difference of these statistical indicators between two phenophases is, the more synchronous the plant phenology overlap rhythm. Based on overlap rhythm between two plant phenophases, the missing data in a phenological time series can be estimated using the observed data of another phenological time series (Schnelle 1955). From the perspective of the food chain, overlapping rhythms between plant and animal phenophases may reflect direct ecological relationships. For example, whenever pears blossom, adults of *Hoplocampa pyricola* lays eggs on the sepals of flowers in areas around Beijing. During the young fruit stage, larva of *H. pyricola* hatches and drills into young fruits, making them turn black and fall off (Yang and Chen 1995). Therefore, understanding overlapping rhythms of plant and insect phenology may also be beneficial for preventing and controlling pests.

Moreover, global climate warming and growing season shifts can alter the overlapping rhythms of producers, consumers, and decomposers, leading to asynchronies resulting in trophic mismatches, which may disrupt ecosystem interactions and food chains (Visser et al. 1998; Both and Visser 2001; Visser and Holleman 2001; Warren et al. 2001; Walther et al. 2002; Strode 2003).

References

Both C, Visser ME (2001) Adjustment to climate change is constrained by arrival date in a long-distance migrant bird. Nature 411:296–298

Foster R, Kreitzman L (2004) Rhythms of life: The biological clocks that control the daily lives of every living thing. Profile Books Ltd., Great Britain

Gardiner BG (1987) Linnaeus' Floral Clock. The. Linnean 3(1):26–29

Hudson IL, Keatley MR (2010) Singular spectrum analysis: climatic niche identification. In: Hudson IL, Keatley MR (eds) Phenological research: Methods for environmental and climate change analysis. Springer, Dordrecht, pp 393–424

Larcher W (1975) Physiological plant ecology. Springer, Berlin

Margary ID (1926) The Marsham phenological record in Norfolk, 1736-1925, and some others. Quarterly Journal of the Royal Meteorological Society 22:27–54

Menzel A (2003) Plant phenological anomalies in Germany and their relation to air temperature and NAO. Climatic Change 57:243–263

Pfau R (1964) Varianz- und Korrelationsanalytische Untersuchungen an Phänologischen Phasen im Naturraum 06 (unterbayerisches Hügelland). Meteor Runds 17(4):113–122

Piltz A, Bever RV (1970) Time without clocks. Crosset & Dunlap, New York

Riedman SR (1982) Biological clocks. Fitzhenry & Whiteside Ltd., Toronto

Schnelle F (1955) Pflanzen-Phänologie. Akademische Verlagsgesellschaft, Geest & Portig K.-G., Leipzig

Strode PK (2003) Implications of climate change for North American wood warblers (Parulidae). Global Change Biol 9:1137–1144

Visser ME, Holleman LJM (2001) Warmer springs disrupt the synchrony of oak and winter moth phenology. Proc. R. Soc. Lond. B 268:289–294

Visser ME, van Noordwijk AJ, Tinbergen JM, Lessells CM (1998) Warmer springs lead to mistimed reproduction in great tits (*Parus major*). Proc. R. Soc. Lond. B 265:1867–1870

Walther GR, Post E, Convey P, Menzel A, Parmesan C, Beebee TJ, Fromentin J-M, Hoegh-Guldberg O, Bairlein F (2002) Ecological responses to recent climate change. Nature 416:389–395

Warren M, Hill J, Thomas J, Asher J, Fox R, Huntley B, Roy D, Telfer M, Jeffcoate S, Harding P (2001) Rapid responses of British butterflies to opposing forces of climate and habitat change. Nature 414:65–69

Yang G, Chen X (1995) Phenological calendars and their applications in the Beijing area (in Chinese). Capital Normal University Press, Beijing

Chapter 3
Spatial Pattern of Plant Phenology

Abstract Plant phenological observations show that occurrence dates of plant growth and reproduction stages are different at different locations, which is mainly a macroscopic and integrative reflection of climatic spatial heterogeneity. Early studies on spatial differences of plant phenology focused on geographical dependence of phenological spatial differences. Typical geographical models of plant phenology were shown as multiple linear regression equations between multi-year mean phenological occurrence dates at individual sites and geo-location parameters (latitude, longitude, and elevation). More recent studies attempt to reveal the relationship between phenological and climatic spatial patterns. Because air temperature is the most important factor influencing spatial variation of plant phenology, multi-year mean monthly temperatures at individual sites (replacing geo-location parameters) have be used as the independent variable for fitting spatial patterns of plant phenological occurrence dates.

Keywords Phenological spatial difference · Bioclimatic law · Multiple linear regression equation · Geo-location parameters · Climatic attribution · Multi-year mean monthly temperature

3.1 Geographical Dependence of Phenological Spatial Differences

Based on early 20th century investigations in the eastern US, Hopkins proposed a "Bioclimatic Law" to estimate the offset in onset of spring as a function of latitude, longitude, and elevation. He wrote:

> Other things being equal, this variation is at the rate of four days for each degree of latitude, five degrees of longitude and 400 ft of altitude. Therefore, from any given place, as related to extensive regions, an entire country, or a continent, the variation in a given periodical event is (at the rate stated) later northward, eastward and upward in the spring and early summer and the reverse in the late summer and during autumn (Hopkins 1919).

X. Chen, *Spatiotemporal Processes of Plant Phenology*,
SpringerBriefs in Geography, DOI 10.1007/978-3-662-49839-2_3

There is no doubt that this "Bioclimatic Law" was an important milestone in revealing geographical attribution of phenological spatial differences. Nevertheless, the geographical pattern and spatial changing rate of plant phenology is diverse and highly dependent on specific regions, years, and phenological phenomena. Subsequently, Nakahara (1948) derived a multiple linear regression equation between multi-year mean flowering date (y) of *Prunus yedoensis* at individual sites and geo-location parameters, such as latitude (ϕ), longitude (λ) and elevation (h). Park-Ono et al. (1993) modified this model (using 37 years of phenological data, 1953–1989) as follows:

$$y = 92.56 + 4.77(\phi - 35^\circ) - 0.59(\lambda - 135^\circ) + 1.28h \tag{3.1}$$

The equation shows that the multi-year mean flowering date of *P. yedoensis* was delayed at a rate of 4.77 days per latitudinal degree northward, 0.59 days per longitudinal degree westward and 1.28 days per 100 m upward. Based on this kind of regression equation, average flowering date isophanes of *P. yedoensis* could be drawn (Momose 1974).

Following the above study, such multiple linear regression equations were also constructed in other regions of the world. The general model for China was described as follows (Gong and Jian 1983):

$$y = a + b(\phi - 30^\circ) + c(\lambda - 110^\circ) + dh \tag{3.2}$$

Table 3.1 indicates that from spring to summer the representative phenophases tended to be delayed by 0.49–5.61 days per latitudinal degree northward, 0.07–1.10 days per longitudinal degree eastward, and 0.32–1.54 days per 100 m upward. In autumn, however, the last three phenophases tended to advance by 2.39–3.81 days per latitudinal degree northward, 0.02 to 0.36 days per longitudinal degree eastward, and 0.06–0.77 days per 100 m upward.

On the basis of multiple linear regression equations between plant phenological occurrence dates in multi-year mean and extreme years, and geo-location parameters, phenological maps of Europe were drawn showing spatial patterns of beginning date, end date and length of the growing season during 1961–1998 and in the warm year 1990 (Rötzer and Chmielewski 2001).

3.2 Climatic Attribution of Phenological Spatial Differences

Overall, the above geographical models of plant phenology have two major disadvantages: (1) geo-location parameters are not climatic factors, so that they neither explain the essential environmental causes nor detect the climatic differences driving plant phenology spatial variations; and (2) since geo-location parameters are constant at a given site, multiple linear regression equation cannot represent the

Table 3.1 Spatial changing rates of plant phenological occurrence dates in China (Gong and Jian 1983)

Species	Phenophase	b (day/degree)	c (day/degree)	d (day/100 m)
Prunus persica	bud swelling	+5.61	+0.92	+1.25
Ulmus pumila	bud swelling	+4.16	+0.53	+0.59
Salix babylonica	budburst	+3.88	+0.78	+0.97
Ulmus pumila	first flowering	+3.55	+0.37	+0.90
Prunus davidiana	first flowering	+3.28	+0.55	+0.81
Thuja orientalis	first flowering	+4.73	+0.87	+0.36
Prunus armeniaca	first flowering	+3.74	+0.78	+1.54
Prunus persica	first flowering	+3.98	+0.71	+1.36
Salix babylonica	first flowering	+3.62	+0.71	+0.38
Morus alba	first flowering	+3.09	+0.36	+0.72
Juglans regia	first flowering	+2.53	+0.73	+1.37
Wisteria sinensis	first flowering	+2.40	+1.10	+0.73
Castanea mollissima	first flowering	+2.02	+0.90	+1.00
Albizzia julibrissin	first flowering	+2.53	+0.07	+0.60
Firmiana simplex	first flowering	+1.06	+0.36	−0.33
Sophora japonica	first flowering	+0.72	+0.19	+0.32
Lagerstroemia indica	first flowering	+0.49	+0.25	+0.53
Osmanthus fragrans	first flowering	−2.39	−0.02	−0.06
Chrysanthemum indicum	first flowering	−3.81	−0.08	−0.69
Ulmus pumila	the end of defoliation	−3.62	−0.36	−0.77

+: The occurrence date delays from south to north, from west to east, from low elevation to high elevation

−: The occurrence date advances from south to north, from west to east, from low elevation to high elevation

interannual variation of plant phenologcal spatial pattern related to climate change. Because air temperature is the most important factor influencing spatial and temporal variations of plant phenology (Chen 1994; Chmielewski and Rötzer 2001; Schwartz and Chen 2002; Menzel 2003; Gordo and Sanz 2010; Chen and Xu 2012), the spatial series of multi-year mean monthly temperature at individual sites (replacing geo-locations) were used for fitting the spatial pattern of growing season beginning date (BGS) and end date (EGS) derived from surface phenological data and remote sensing data (Chen et al. 2005). The results show that spatial series of multi-year mean BGS date correlates negatively ($P < 0.001$) with spatial series of multi-year mean temperature from March to May across temperate eastern China. The multinomial fitting (Fig. 3.1) shows that the dependence of BGS date on multi-year mean temperature is much stronger at sites with March-May temperature above 0 °C (linear correlation coefficient $r = -0.8276$, $n = 51$, $P < 0.001$) than at sites with March-May temperature below 0 °C (linear correlation coefficient

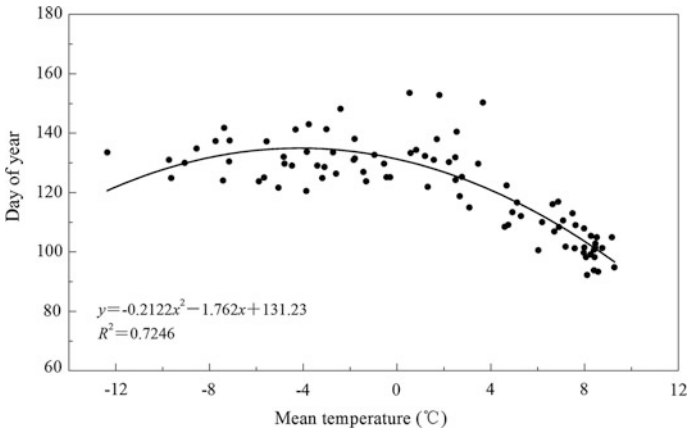

Fig. 3.1 Spatial relationships between March–May mean temperatures and average growing season beginning dates from 1982 to 1993 [Reprinted from Chen et al. (2005), with permission from John Wiley and Sons]

r = −0.0454, n = 36, $P > 0.1$). The negative correlation indicates that the higher the multi-year mean temperature during March and May at a site, the earlier the average growing season beginning time. In contrast, spatial series of multi-year mean EGS date correlates positively ($P < 0.001$) with spatial series of multi-year mean temperature from August to October across temperate eastern China. The positive correlation indicates that the higher the multi-year mean temperature during August and October at a site, the later the average growing season end time (Fig. 3.2).

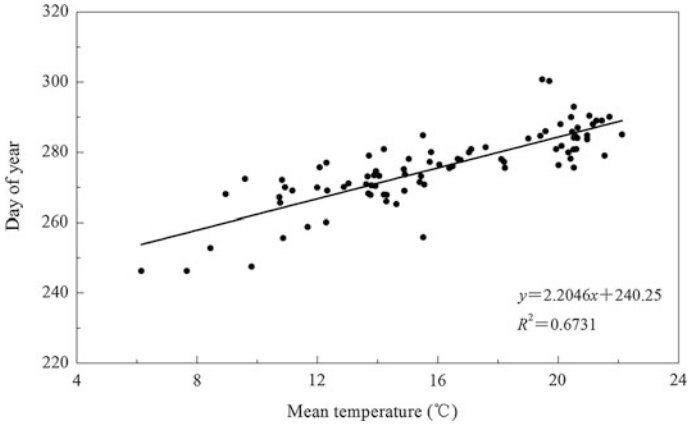

Fig. 3.2 Spatial relationships between August-October mean temperatures and average growing season end dates from 1982 to 1993 [Reprinted from Chen et al. (2005), with permission from John Wiley and Sons]

References

Chen XQ (1994) Untersuchung zur zeitlich-räumlichen Ähnlichkeit von phänologischen und klimatologischen Parametern in Westdeutschland und zum Einfluß geoökologischer Faktoren auf die phänologische Entwicklung im Gebiet des Taunus. Selbstverlag des Deutschen Wetterdienstes, Offenbach am Main

Chen XQ, Xu L (2012) Phenological responses of *Ulmus pumila* (Siberian Elm) to climate change in the temperate zone of China. Int J Biometeorol 56(4):695–706

Chen XQ, Hu B, Yu R (2005) Spatial and temporal variation of phenological growing season and climate change impacts in temperate eastern China. Glob Change Biol 11(7):1118–1130

Chmielewski FM, Rötzer T (2001) Response of tree phenology to climate change across Europe. Agr Forest Meteorol 108(2):101–112

Gong G, Jian W (1983) On the geographical distribution of phenodate in China. Acta Geographica Sinica 38(1):33–40

Gordo O, Sanz JJ (2010) Impact of climate change on plant phenology in Mediterranean ecosystems. Glob Change Biol 16(3):1082–1106

Hopkins AD (1919) The bioclimatic law as applied to entomological research and farm practise. The Scientific Monthly 8(6):496–513

Menzel A (2003) Plant phenological anomalies in Germany and their relation to air temperature and NAO. Clim Change 57(3):243–263

Momose N (1974) Atlas of animal and plant phenology of Japan (in Japanese). Marunouchi Shuppan Book Co., Tokyo

Nakahara M (1948) Phenology (in Japanese). Kawadesyobo Press, Tokyo

Park-Ono HS, Kawamura T, Yoshino M (1993) Relationships between flowering date of cherry blossom (*Prunus yedoensis*) and air temperature in East Asia. Proceedings of the 13th International Congress of Biometeorology, Calgary

Rötzer T, Chmielewski FM (2001) Phenological maps of Europe. Clim Res 18:249–257

Schwartz MD, Chen XQ (2002) Examining the onset of spring in China. Clim Res 21:157–164

Chapter 4
Statistical Simulation of Plant Phenology Temporal Variation

Abstract To simulate temporal variation of plant phenology, daily mean air temperature-based temporal phenology models were constructed using *Taraxacum mongolicum* first leaf unfolding and common leaf coloration data at 52 stations within eastern China's temperate zone from 1990 to 2009, and *Ulmus pumila* first leaf unfolding and leaf fall end data at 46 stations across China's temperate zone from 1986 to 2005. Results show that the new model is more precise and rational in detecting responses of plant phenology to temperature than conventional monthly mean air temperature-based phenology models. Both *T. mongolicum* and *U. pumila* phenology shows a consistent response to temperatures at local and regional scales. Namely, first leaf unfolding date has a significantly negative response to spring temperature, while common leaf coloration and leaf fall end dates have a significantly positive response to autumn temperature. Moreover, a 1 °C increase in spring temperature may cause a larger advancement of first leaf unfolding date at warmer locations than at colder locations for both *T. mongolicum* and *U. pumila*, whereas a 1 °C increase in autumn temperature may induce a larger delay of leaf fall end date at warmer locations than at colder locations for *U. pumila*. Therefore, future regional climate warming may enhance sensitivity of plant phenological response to temperature, especially in the colder regions where the greatest climate warming is expected.

Keywords Daily mean air temperature-based temporal phenology model · Optimum length period · Phenological response to temperature · Spatial differentiation of sensitivity

4.1 Introduction

According to the phenological rhythmicity described in Chap. 2, occurrence dates of various plant phenological phenomena obey a certain time sequence within a year, and synchronously advance or postpone among years. For a given phenological phenomenon, its occurrence dates have circannual and multi-year rhythms.

X. Chen, *Spatiotemporal Processes of Plant Phenology*,
SpringerBriefs in Geography, DOI 10.1007/978-3-662-49839-2_4

Thus, temporal variations at seasonal, interannual, and multi-year scales are the striking characteristics of phenological occurrence dates. To investigate climatic attributions of the temporal variation of phenological occurrence dates, both statistical and process-based models can be employed. Because air temperature is the most important climate driver of phenological occurrence dates for plant species living in humid and semihumid areas, numerous statistical studies use air temperature as the climatic factor to simulate phenological time series (Chen 1994; Chmielewski and Rötzer 2001; Matsumoto et al. 2003; Menzel 2003; Gordo and Sanz 2010; Chen and Xu 2012). In this chapter, a daily mean air temperature-based statistical model and its applications in simulating long-term phenological time series are introduced.

4.2 Model Description

The conventional approach for examining plant phenological response to air temperature was to create a linear regression equation between a phenological event occurrence date and mean air temperature within several months during and before the average phenological event occurrence date (Chen 1994; Sparks et al. 2000; Menzel 2003; Gordo and Sanz 2010). Nevertheless, using current and preceding monthly mean air temperature as the independent variable may not be precise sufficiently, as a phenological event occurrence date is not likely caused by the integral monthly mean temperature exactly, but by daily mean temperature during a certain length period (LP, days). Thus, an alternative method has been proposed (Chen and Xu 2012). The basic hypothesis of the new method is that the year-to-year variation of a phenological event occurrence date at a station is mainly controlled by year-to-year variation of daily mean temperature within a particular LP during and before its occurrence date at the station. The computation process is implemented through following steps. First, the entire interval between the earliest and latest date of a phenological time series at a station is defined as the basic LP (bLP), and then the daily mean temperature time series during bLP + mLP are computed. Here, mLP is a moving length period prior to the earliest date of the phenological timing series, which moves with a step length of 1 day. The maximum mLP is restricted to 60 days because daily mean temperature prior to this period is usually assumed to have limited effects on a phenological event occurrence date in temperate areas (Chen 1994; Sparks et al. 2000; Menzel 2003). The LP is therefore defined as follows:

$$LP = bLP + mLP \tag{4.1}$$

Further, correlation coefficients between phenological time series and daily mean air temperature time series during the different LPs are calculated at the station, and the optimum LP corresponding to the largest correlation coefficient between

phenological time series and daily mean air temperature time series is obtained at the station. Taking the daily mean air temperature during the optimum LP as the independent variable and the phenological event occurrence date as the dependent variable, the daily mean air temperature-based temporal phenology model can be determined:

$$Phenodate = a + bT_{optimum} \tag{4.2}$$

where *Phenodate* denotes the phenological event occurrence date in different years; $T_{optimum}$ denotes the daily mean air temperature during the optimum LP in different years; a is the intercept; b is the regression coefficient.

4.3 Model Applications

In order to validate the feasibility and accuracy of this new phenology model form in revealing temporal response of plant phenology to daily mean air temperature, the optimum spring/autumn LPs were calculated for *Taraxacum mongolicum* first leaf unfolding date (beginning date of the growing season, BGS) and common leaf coloration date (end date of the growing season, EGS) at 52 stations across eastern China's temperate zone from 1990 to 2009 (Fig. 4.1; Chen et al. 2015) and for *Ulmus pumila* first leaf unfolding date (BGS) and leaf fall end date (EGS) at 46 stations across China's temperate zone from 1986 to 2005 (Fig. 4.2; Chen and Xu 2012), respectively.

For *T. mongolicum* (Chen et al. 2015), the optimum spring LPs range from 17 to 78 days, while the optimum autumn LPs are between 15 and 104 days at the 52 stations (Fig. 4.3). The daily mean air temperature-based temporal phenology models were constructed between BGS date and the optimum spring LP temperature ($P < 0.05$) at 51 stations (98 %) and between EGS date and the optimum autumn LP temperature ($P < 0.05$) at only 17 stations (33 %). The regression model slopes indicate that a higher optimum spring LP temperature triggers an earlier BGS date at rates of −1.25 to −6.67 days $°C^{-1}$, while a higher optimum autumn LP temperature induces a later EGS date at rates of 1.59 to 7.85 days $°C^{-1}$ (Table 4.1).

Moreover, daily mean air temperature-based temporal phenology models were also created between the regional mean *T. mongolicum* BGS/EGS date and regional daily mean temperature during the optimum spring/autumn LP (based on the 52 stations) from 1990 to 2009 ($P < 0.001$). The regional mean optimum spring and autumn LPs are 46 and 47 days, respectively. The regression model slopes show that a 1 °C increase in the regional mean optimum spring LP temperature causes an advancement of 2.1 days in the regional mean BGS date, while a 1 °C increase in the regional mean optimum autumn LP temperature induces a delay of 2.3 days in the regional mean EGS date (Fig. 4.4).

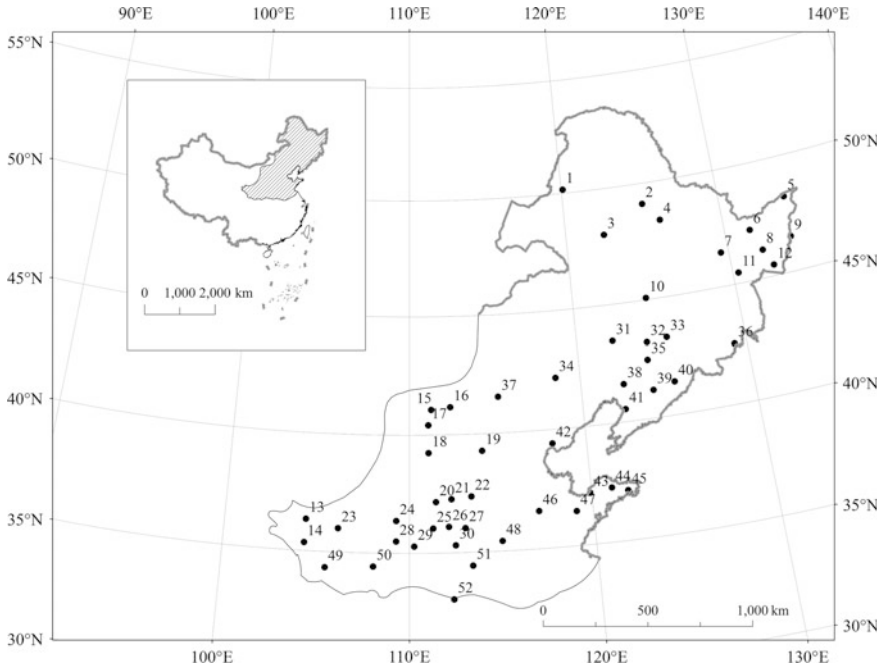

Fig. 4.1 Location of phenological stations of *Taraxacum mongolicum* with long-term observation data (more than 15 years) across eastern China's temperate zone [Reprinted from Chen et al. (2015), with permission from Springer]

A further correlation analysis between regression model slope (Table 4.1) and long-term annual mean temperature over the 52 stations shows that location-specific BGS-temperature regression slope correlates negatively with location-specific annual mean temperature ($P < 0.05$), which implies that the negative response of BGS to the spring LP temperature was stronger at warmer locations than at colder locations, namely, a 1 °C increase in the optimum spring LP temperature may cause a larger advancement of BGS at warmer locations than at colder locations. In contrast with BGS, location-specific EGS-temperature regression slope does not correlate significantly with location-specific annual mean temperature.

For *U. pumila* (Chen and Xu 2012), the optimum spring LPs range from 19 to 102 days and the optimum autumn LPs are between 15 and 99 days at the 46 stations (Fig. 4.5). The daily mean air temperature-based temporal phenology models were constructed between BGS date and the optimum spring *LP* temperature ($P < 0.05$) at 41 stations (89 %). On average, a 1 °C increase in the optimum spring *LP* temperature advances BGS dates between 1.02 and 7.63 days (Table 4.2). However, the daily mean air temperature-based temporal phenology models were created between EGS date and the optimum autumn *LP* temperature

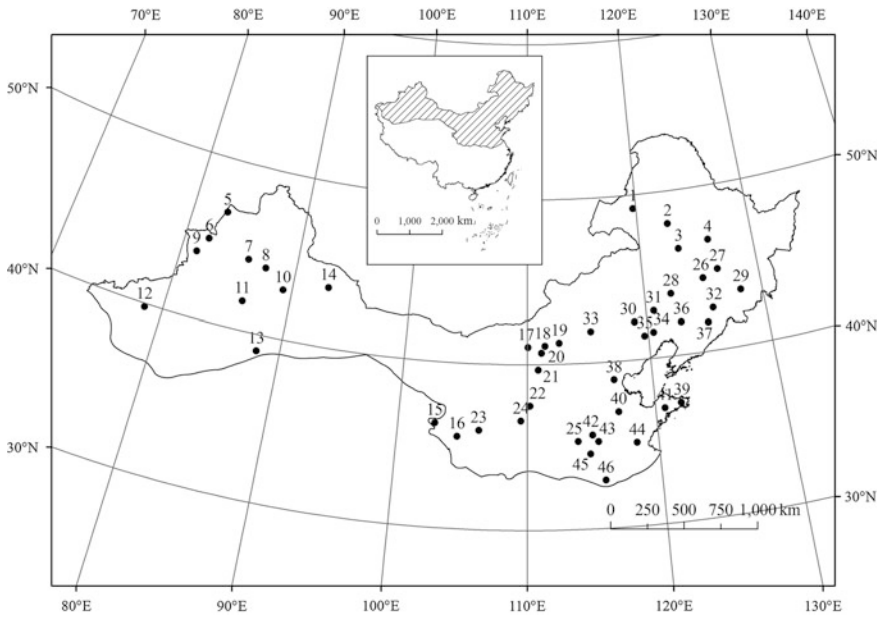

Fig. 4.2 Location of phenological stations of *Ulmus pumila* with long-term observation data (more than 16 years) across China's temperate zone [Reprinted from Chen and Xu (2012), with permission from Springer]

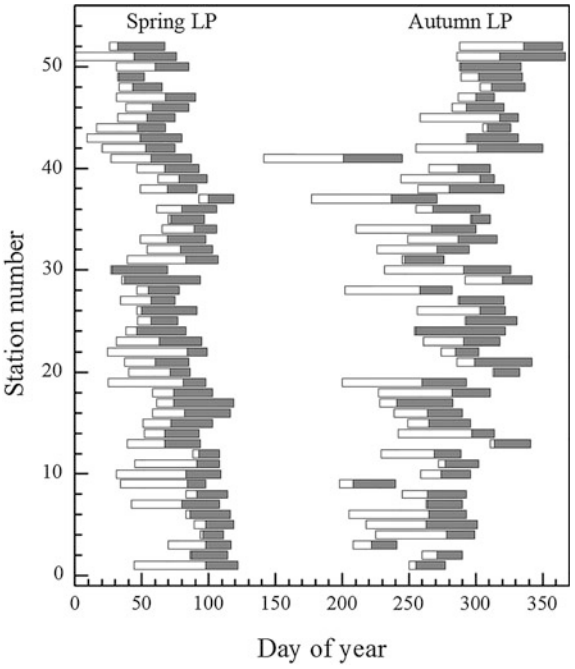

Fig. 4.3 Optimum spring LP [*black bars* basic LP (bLP), *gray bars* moving LP (mLP)] and autumn LP (*black bars* bLP, *gray bars* mLP) corresponding to *Taraxacum mongolicum* BGS and EGS at each station [Reprinted from Chen et al. (2015), with permission from Springer]

Table 4.1 Regression analyses between BGS date and spring LP temperature and between EGS date and autumn LP temperature for *Taraxacum mongolicum* at each station (Chen et al. 2015)

Station number	BGS		EGS	
	R^2	Slope (days °C^{-1})	R^2	Slope (days °C^{-1})
1	0.23	−2.29*	0.18	+1.57
2	0.29	−2.20*	0.07	+0.91
3	0.26	−1.50*	0.45	+3.79**
4	0.46	−1.27***	0.03	+1.19
5	0.45	−2.66**	0.04	+3.10
6	0.26	−2.50*	0.15	+6.37
7	0.55	−2.78***	0.00	−0.04
8	0.32	−2.07**	0.07	+2.50
9	0.40	−1.25**	0.09	−3.24
10	0.27	−1.78*	0.06	+1.55
11	0.37	−1.53*	0.00	−0.14
12	0.46	−1.97***	0.12	+2.93
13	0.73	−5.60***	0.12	+1.66
14	0.75	−4.98***	0.23	+3.98
15	0.48	−4.32***	0.35	+5.04**
16	0.34	−3.39**	0.28	+3.81*
17	0.40	−6.67**	0.25	−5.93
18	0.37	−4.07**	0.09	+3.48
19	0.45	−1.78**	0.50	+7.26**
20	0.21	−1.72*	0.25	+1.68*
21	0.43	−3.35**	0.01	−1.58
22	0.28	−1.48*	0.45	+3.02***
23	0.32	−4.10*	0.06	−2.03
24	0.63	−5.47***	0.21	+10.03
25	0.46	−2.29***	0.01	−0.83
26	0.55	−4.66***	0.00	−0.18
27	0.38	−2.21**	0.07	+2.17
28	0.35	−2.70**	0.02	+1.94
29	0.31	−5.95*	0.10	+2.29
30	0.35	−4.77**	0.28	+5.73*
31	0.25	−2.68*	0.50	+6.58***
32	0.44	−2.42***	0.08	+3.45
33	0.62	−2.85***	0.10	+2.56
34	0.59	−2.73***	0.08	−2.13
35	0.48	−2.37***	0.00	+0.07
36	0.40	−2.88**	0.18	+4.79
37	0.55	−2.34***	0.29	+7.09*
38	0.37	−1.99**	0.00	+0.35

(continued)

Table 4.1 (continued)

Station number	BGS		EGS	
	R^2	Slope (days °C^{-1})	R^2	Slope (days °C^{-1})
39	0.25	−1.66*	0.02	+0.52
40	0.77	−3.66***	0.28	+2.92*
41	0.23	−2.65*	0.27	+7.33*
42	0.56	−3.26***	0.43	+7.85**
43	0.44	−5.27***	0.00	−0.24
44	0.29	−1.54*	0.05	−0.50
45	0.72	−3.33***	0.17	+2.08
46	0.70	−3.30***	0.26	+3.10*
47	0.15	−1.47	0.34	+1.59**
48	0.32	−2.48**	0.24	+2.41*
49	0.44	−1.56**	0.05	+1.65
50	0.30	−2.80*	0.21	+7.33*
51	0.28	−3.59*	0.26	+6.08*
52	0.46	−3.96***	0.01	−1.13

*$P < 0.05$; **$P < 0.01$; ***$P < 0.001$

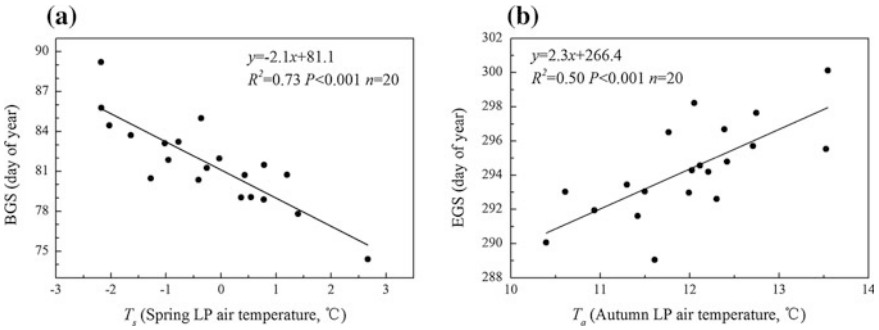

Fig. 4.4 Regression analyses between **a** regional mean beginning date of the growing season (BGS) and regional spring length period (LP) temperature (T_s), **b** regional mean end date of the growing season (EGS) and regional autumn LP temperature (T_a) for *Taraxacum mongolicum* from 1990 to 2009 [Reprinted from Chen et al. (2015), with permission from Springer]

($P < 0.05$) at only 12 stations (26 %), where a 1 °C increase in the optimum autumn *LP* temperature delays EGS dates between 1.96 and 7.65 days (Table 4.2).

Across the entire China's temperate zone, regional mean regression models were constructed between the regional mean BGS/EGS time series and the regional mean optimum spring/autumn *LP* temperature time series (based on the 46 stations) during 1986–2005. The regional mean optimum spring and autumn LPs are 73 and

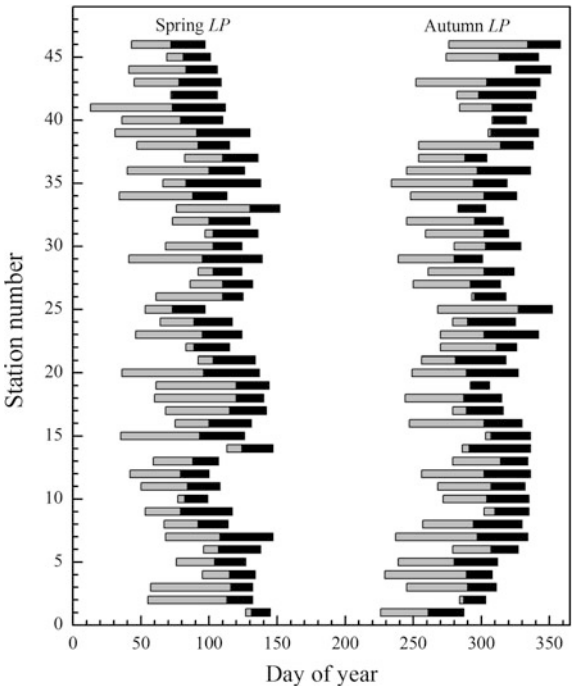

Fig. 4.5 Optimum spring LP [*black bars* basic LP (bLP), *gray bars* moving LP (mLP)] and autumn LP (*black bars* bLP, *gray bars* mLP) corresponding to *Ulmus pumila* BGS and EGS at each station [Reprinted from Chen and Xu (2012), with permission from Springer]

65 days, respectively. Similar to individual stations, a 1 °C increase in the regional mean optimum spring *LP* temperature induces an advancement of 2.8 days in the regional mean BGS date and a 1 °C increase in the regional mean optimum autumn *LP* temperature causes a delay of 2.1 days in the regional mean EGS date (Fig. 4.6).

In addition, a correlation analysis between regression model slope (Table 4.2) and long-term annual mean temperature over the 46 stations indicates that location-specific BGS-temperature regression slope correlates significantly negative with location-specific annual mean temperature ($P < 0.1$), while location-specific EGS-temperature regression slope correlates significantly positive with location-specific annual mean temperature ($P < 0.05$). Thus, either the negative response of BGS to the spring *LP* temperature or the positive response of EGS to the autumn *LP* temperature was stronger at warmer locations than at colder locations. That is, a 1 °C increase in the optimum spring LP temperature may cause a larger advancement of BGS at warmer locations than at colder locations, whereas a 1 °C increase in the optimum autumn LP temperature may induce a larger delay of EGS at warmer locations than at colder locations.

The above two case studies demonstrate that the daily mean air temperature-based temporal phenology model can not only be used to fit tree phenology but also to fit herb phenology. BGS/EGS date of both *T. mongolicum* and *U. pumila* has a coincident response to the optimum LP temperature at local and regional scales. That is,

Table 4.2 Regression analyses between BGS date and spring LP temperature and between EGS date and autumn LP temperature for *Ulmus pumila* at each station (Chen and Xu 2012)

Station number	BGS		EGS	
	R^2	Slope (days °C^{-1})	R^2	Slope (days °C^{-1})
1	0.58	−1.95***	0.03	−0.88
2	0.14	−1.28	0.13	−0.70
3	0.74	−2.47***	0.25	1.96*
4	0.31	−1.65*	0.12	1.83
5	0.35	−1.46**	0.12	1.83
6	0.18	−2.54*	0.30	2.08*
7	0.42	−4.12**	0.21	3.17*
8	0.67	−2.28***	0.17	3.13
9	0.55	−4.35***	0.04	−0.83
10	0.21	−1.02*	0.36	4.50**
11	0.72	−4.63***	0.04	1.78
12	0.31	−2.79*	0.22	7.65*
13	0.46	−2.62**	0.17	2.66
14	0.48	−3.18***	0.18	−2.09
15	0.26	−4.61*	0.08	−1.92
16	0.67	−6.37***	0.15	3.92
17	0.18	−2.25	0.06	1.21
18	0.69	−3.99***	0.18	3.18
19	0.32	−2.48**	0.12	0.56
20	0.25	−4.38*	0.07	3.26
21	0.27	−2.27*	0.08	2.86
22	0.62	−3.36***	0.15	1.72
23	0.64	−4.00***	0.01	−1.35
24	0.56	−4.20***	0.06	−2.05
25	0.58	−2.73***	0.06	1.97
26	0.36	−1.61**	0.04	−0.71
27	0.37	−2.33**	0.18	2.77
28	0.48	−2.51***	0.26	2.67*
29	0.14	−2.18	0.50	5.20***
30	0.56	−3.55***	0.09	1.36
31	0.55	−3.97***	0.28	2.22*
32	0.58	−4.17***	0.10	1.89
33	0.62	−3.94***	0.06	0.84
34	0.66	−2.98***	0.37	4.34**
35	0.44	−7.63**	0.03	1.52
36	0.21	−2.64*	0.29	4.76*
37	0.45	−3.39**	0.04	0.95
38	0.42	−3.29**	0.10	2.54

(continued)

Table 4.2 (continued)

Station number	BGS		EGS	
	R^2	Slope (days °C^{-1})	R^2	Slope (days °C^{-1})
39	0.18	−4.17	0.08	2.75
40	0.66	−5.10***	0.28	2.30*
41	0.11	−2.69	0.01	0.58
42	0.67	−6.58***	0.10	4.35
43	0.72	−5.88***	0.16	6.29
44	0.74	−4.46***	0.17	2.12
45	0.79	−2.94*	0.40	6.42**
46	0.29	−2.68*	0.06	−1.74

*$P < 0.05$; **$P < 0.01$; ***$P < 0.001$

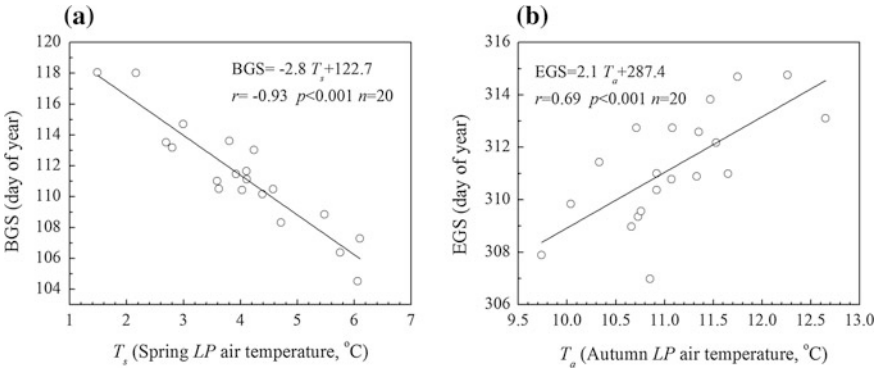

Fig. 4.6 Regression analyses between **a** regional mean beginning date of the growing season (BGS) and regional spring length period (LP) temperature (T_s), **b** regional mean end date of the growing season (EGS) and regional autumn LP temperature (T_a) for *Ulmus pumila* from 1986 to 2005 [Reprinted from Chen and Xu (2012), with permission from Springer]

BGS displays a significantly negative response to optimum spring LP temperature, while EGS indicates a significantly positive response to optimum autumn LP temperature. Moreover, the sensitivity of plant phenology response to temperature fall in similar ranges.

Generally speaking, the spatial differentiation of sensitivity of plant phenological response to temperature may essentially be caused by the long-term adaptation of plant phenology to local and regional climate. However, as rapid climate change is likely to disturb this adaptation (Kramer 1996), future regional climate warming may enhance sensitivity of plant phenological response to temperature, especially in the colder regions where the greatest climate warming is expected (IPCC 2007).

References

Chen XQ (1994) Untersuchung zur zeitlich-räumlichen Ähnlichkeit von phänologischen und klimatologischen Parametern in Westdeutschland und zum Einfluß geoökologischer Faktoren auf die phänologische Entwicklung im Gebiet des Taunus. Selbstverlag des Deutschen Wetterdienstes, Offenbach am Main

Chen XQ, Xu L (2012) Phenological responses of *Ulmus pumila* (Siberian Elm) to climate change in the temperate zone of China. Int J Biometeorol 56:695–706

Chen XQ, Tian YH, Xu L (2015) Temperature and geographic attribution of change in the *Taraxacum mongolicum* growing season from 1990 to 2009 in eastern China's temperate zone. Int J Biometeorol 59:1437–1452

Chmielewski FM, Rötzer T (2001) Response of tree phenology to climate change across Europe. Agric For Meteorol 108:101–112

Gordo O, Sanz JJ (2010) Impact of climate change on plant phenology in Mediterranean ecosystems. Glob Change Biol 16:1082–1106

IPCC (2007) Climate change 2007: the physical science basis. In: Solomon S, Qin D, Manning M, Chen Z, Marquis M, Averyt KB, Tignor M, Miller HL (eds) Contribution of working group I to the fourth assessment report of the Intergovernmental Panel on Climate Change. Cambridge University Press, Cambridge

Kramer K (1996) Phenology and growth of European trees in relation to climate change. Dissertation, Landbouw Universiteit Wageningen

Matsumoto K, Ohta T, Irasawa M, Nakamura T (2003) Climate change and extension of the *Ginkgo biloba* L. growing season in Japan. Glob Change Biol 9:1634–1642

Menzel A (2003) Plant phenological anomalies in Germany and their relation to air temperature and NAO. Clim Change 57:243–263

Sparks T, Jeffree E, Jeffree C (2000) An examination of the relationship between flowering times and temperature at the national scale using long-term phenological records from the UK. Int J Biometeorol 44:82–87

Chapter 5
Statistical Simulation of Plant Phenology Spatial Variation

Abstract Daily mean air temperature-based spatial phenology models were fitted and validated using *Ulmus pumila* first leaf unfolding and leaf fall end data at 46 stations within China's temperate zone from 1986 to 2005. Results show that spatial patterns of first leaf unfolding and leaf fall end dates were obviously influenced by spatial patterns of daily mean air temperatures during the optimum spring and autumn length period, respectively. A higher location-specific multi-year mean spring and autumn temperature resulted in an earlier location-specific multi-year mean first leaf unfolding date and a later leaf fall end date. On average, a 1 °C spatial shift in multi-year mean spring and autumn temperatures may cause a spatial shift of −3.1 days and 2.6 days in multi-year mean first leaf unfolding and leaf fall end dates, respectively. Similar spatial relationships were also detected between daily mean temperature and phenological occurrence date in each year. The regression equations indicate that a 1 °C spatial shift in yearly mean spring and autumn temperatures may induce a spatial shift between −4.28 and −2.75 days in yearly first leaf unfolding date, and between 2.17 and 3.16 days in yearly leaf fall end date. Error estimation confirmed the reliability of multi-year mean and yearly spatial phenology models in simulating and predicting spatial patterns of *Ulmus pumila* first leaf unfolding and leaf fall end dates. Further analysis showed that a 1 °C spatial shift in mean spring temperature in warmer years may induce a larger spatial shift in first leaf unfolding date than that in colder years. Thus, future climate warming may enhance sensitivity of the spatial response of first leaf unfolding to temperature.

Keywords Daily mean air temperature-based spatial phenology model · Spatial response · Sensitivity · Spatial extrapolation · Spatial standard deviation

5.1 Introduction

According to the geographical dependence and climatic attribution analyses of phenological spatial difference reported in Chap. 3, spatial differences in occurrence dates of plant phenological phenomena rely highly on geo-location parameters of

X. Chen, *Spatiotemporal Processes of Plant Phenology*,
SpringerBriefs in Geography, DOI 10.1007/978-3-662-49839-2_5

the observation sites (latitude, longitude and elevation). As geo-location parameters are constant at a given site, the multiple linear regression equation can usually describe the statistical relationship between geo-location parameters and phenological occurrence dates on the multi-year average (Nakahara 1948; Gong and Jian 1983; Park-Ono et al. 1993; Rötzer and Chmielewski 2001). To investigate the climatic causes resulting in plant phenology spatial variations, the monthly mean air temperature-based regression equation can be used to fit the spatial series of occurrence dates of a phenological phenomenon either to the multi-year average or for specific years (Chen et al. 2005). However, the regression equation between spatial series of phenological occurrence date and monthly mean temperature may not describe the climatic attribution of plant phenology spatial variations sufficiently, as a phenological event occurrence date may not be triggered by the integral monthly mean temperature, but by daily mean temperature during a certain period. Therefore, to fit plant phenology spatial pattern more effectively, a daily mean air temperatures-based spatial phenology model has been proposed (Chen and Xu 2012a).

5.2 Model Description

Other than plant phenology time series modeling (Chen and Xu 2012b), the basic hypothesis for plant phenology spatial series modeling is that the station-to-station variation of a phenological event occurrence date in a geographic region is controlled by the station-to-station variation of daily mean air temperature within a particular length period (LP, days) during and before the phenological event occurrence date in the geographic region. The computation process of the daily mean air temperature-based spatial phenology model includes following steps. First, the entire interval between the earliest and latest date of a phenological spatial series across all sites in a year is defined as the basic LP (bLP). Then, the daily mean temperature spatial series during bLP + mLP are computed. Here, mLP is a moving length period prior to the earliest date of the phenological spatial series, which moves with a step length of 1 day. The maximum mLP is restricted to 90 days because the station-to-station variation of daily mean temperature prior to this period does not have any effects on the station-to-station variation of *Ulmus pumila* first leaf unfolding and leaf fall end dates over 46 stations in China's temperate zone from 1986 to 2005 (Chen and Xu 2012a). Thus, the LP is defined as follows:

$$LP = bLP + mLP \tag{6.1}$$

Moreover, correlation coefficients between plant phenological spatial series and daily mean temperature spatial series during the different LPs are computed across all sites during the year, and the optimum LP corresponding to the largest correlation coefficient between plant phenological spatial series and daily mean

temperature spatial series in the year is obtained. The above computation steps to find the optimum LP in a year can be also used to determine the multi-year mean optimum LP of the entire study period. In that case, the multi-year mean plant phenological spatial series and multi-year mean daily temperature spatial series across all sites should be used (Chen and Xu 2012a). Taking the daily mean air temperature during the optimum LP as the independent variable and phenological event occurrence date as the dependent variable, the daily mean air temperature-based spatial phenology model can be expressed as follows:

$$Phenodate = a + bT_{optimum} \tag{6.2}$$

where *Phenodate* denotes the phenological event occurrence date at different sites in a year; $T_{optimum}$ denotes the daily mean air temperatures during the optimum LP at different sites in the year; a is the intercept; b is the regression coefficient.

Model performance in the spatial simulation and extrapolation are evaluated using Root Mean Square Error (RMSE) between predicted and observed phenological occurrence dates, and explained variance (R^2). RMSE is calculated by the following formula:

$$RMSE = \sqrt{\frac{\sum_{i=1}^{n} (Pre_i - Obs_i)^2}{n}} \tag{6.3}$$

where Obs_i represents the observed phenological event occurrence date at the site i; Pre_i represents the predicted phenological event occurrence date at the site i; n is the number of sites.

5.3 Model Applications

For assessing reliability and feasibility of the phenology model in detecting spatial responses of plant phenology to daily mean air temperature, the optimum spatial LPs were calculated for the *Ulmus pumila* first leaf unfolding date (beginning date of the growing season, BGS) and leaf fall end date (end date of the growing season, EGS) across 46 stations within China's temperate zone with time series lengths of at least 16 years from 1986 to 2005. In addition, model performance was validated by means of the spatial extrapolation based on *Ulmus pumila* BGS and EGS data at 62 external stations with time series lengths less than 16 years during 1986–2005 (Chen and Xu 2012a; Fig. 5.1).

For the multi-year mean *Ulmus pumila* BGS modeling, a significant negative response of mean BGS date to mean daily temperature during the optimum spring LP (123 days) was detected ($P < 0.001$) across the 46 stations from 1986 to 2005. That is, a higher location-specific mean daily temperature during the optimum spring LP resulted in an earlier location-specific mean BGS date across China's temperate zone. The explained variance of mean spring spatial phenology model to

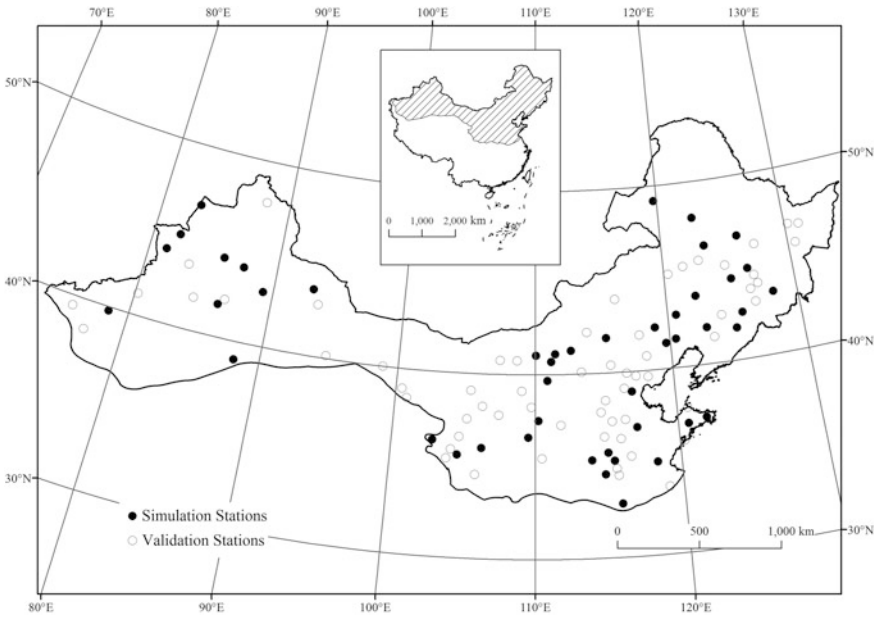

Fig. 5.1 Spatial distribution of phenological stations of *Ulmus pumila* in China's temperate zone [Reprinted from Chen and Xu (2012a), with permission from Elsevier]

BGS date is 90 % ($P < 0.001$) and the RMSE for differences between observed and simulated BGSs is 4.6 days. On average, a 1 °C spatial shift in multi-year mean daily temperature within the optimum spring LP may induce a spatial shift of –3.1 days in multi-year mean BGS date (Fig. 5.2a). Contrast to BGS, a significant positive response of mean EGS date to mean daily temperature during the optimum autumn LP (66 days) was found ($P < 0.001$) across the 46 stations during 1986-2005, namely, a higher location-specific mean daily temperature during the optimum autumn LP caused a later location-specific mean EGS date across China's temperate zone. The explained variance of mean autumn spatial phenology model to EGS date is 82 % ($P < 0.001$) and the RMSE for differences between observed and simulated EGSs is 5.6 days. On average, a 1 °C spatial shift in multi-year mean daily temperature within the optimum autumn LP may result in a spatial shift of 2.6 days in multi-year mean EGS date (Fig. 5.2b).

Spatial extrapolation tests of the mean spring and autumn spatial phenology models (Fig. 5.2) were carried out using multi-year mean daily temperatures during the optimum spring and autumn LPs and observed multi-year mean BGS and EGS dates at the 16 external stations. The accuracies of predicted BGS and EGS dates, measured by RMSEs for differences between observed and predicted BGS/EGS dates were 5.8 days and 4.8 days, respectively (Fig. 5.3). Comparing external validation accuracy (Fig. 5.3) with internal simulation accuracy (Fig. 5.2) of mean spatial phenology models, RMSE of external validation for BGS is 1.2 days larger than that of internal simulation, while RMSE of external validation for EGS is

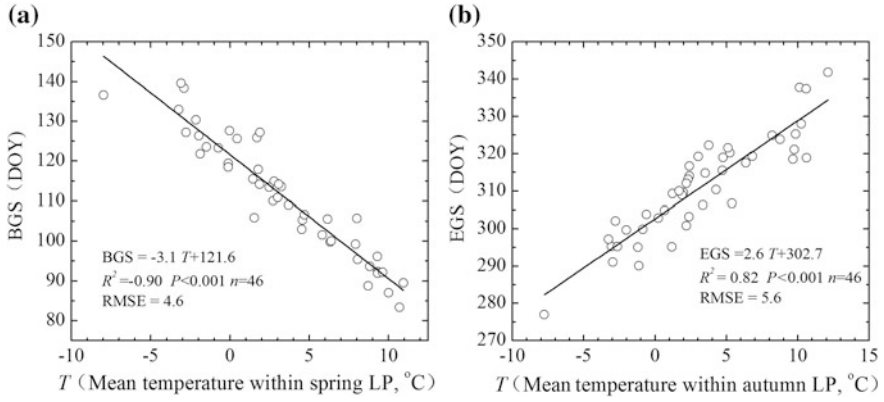

Fig. 5.2 Spatial regression analyses, **a** between multi-year mean daily temperature during the optimum spring LP and multi-year mean BGS date (day of year, DOY) of *Ulmus pumila* and **b** between multi-year mean daily temperature during the optimum autumn LP and multi-year mean EGS date (DOY) of *Ulmus pumila* over the 46 stations [Reprinted from Chen and Xu (2012a), with permission from Elsevier]

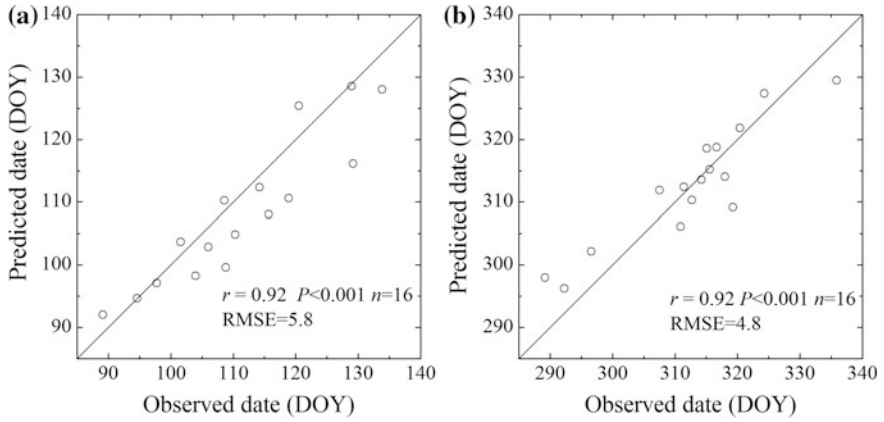

Fig. 5.3 External validation of mean spatial phenology models by means of the spatial extrapolation of mean *Ulmus pumila* (**a**) BGS and (**b**) EGS at 16 external stations [Reprinted from Chen and Xu (2012a), with permission from Elsevier]

0.8 days smaller than that of internal simulation. Therefore, spatial patterns of multi-year mean *Ulmus pumila* BGS and EGS dates can be effectively simulated and predicted by spatial patterns of multi-year mean daily temperatures during the optimum spring and autumn LPs.

Similar to the multi-year mean *Ulmus pumila* BGS modeling, significant negative responses of yearly BGS dates to yearly mean daily temperatures during the optimum spring LP ($P < 0.001$) were also detected across the 46 stations during 1986–2005. Regression analyses showed that the yearly spring spatial phenology

models explained 73–86 % of BGS variances and the RMSEs for differences between yearly observed and simulated BGSs ranged from 5.4 to 9.8 days. On average, a 1 °C spatial shift in yearly mean daily temperature within the optimum spring LP may cause a spatial shift between −4.28 and −2.75 days in yearly BGS dates. Contrarily, significant positive responses of yearly EGS dates to yearly mean daily temperatures during the optimum autumn LP ($P < 0.001$) were found across the 46 stations during 1986–2005. The yearly autumn spatial phenology models explained 49–77 % of EGS variances and the RMSEs for differences between yearly observed and simulated EGSs ranged from 7.4 to 11.2 days. The regression equations denote that a 1 °C spatial shift in yearly mean daily temperature within the optimum autumn LP may induce a spatial shift between 2.17 and 3.16 days in yearly EGS dates. The average RMSE of yearly BGS simulations is 1.5 days smaller than that of yearly EGS simulations (Table 5.1).

Spatial extrapolation tests of the yearly spring and autumn spatial phenology models at the 12–39 external stations during 1986 to 2005 show that the mean

Table 5.1 Spatial regression analyses between daily temperature within optimum spring/autumn LP and *Ulmus pumila* BGS/EGS date in each year (Chen and Xu 2012a)

Year	BGS simulation				EGS simulation			
	Number of stations	Slope (days °C^{-1})	R^2	RMSE (days)	Number of stations	Slope (days °C^{-1})	R^2	RMSE (days)
1986	35	−3.07	0.78*	6.1	35	2.83	0.69*	7.7
1987	40	−3.06	0.86*	5.5	40	2.77	0.54*	9.8
1988	41	−3.08	0.81*	6.2	39	2.46	0.61*	8.0
1989	40	−3.36	0.87*	5.4	40	3.00	0.69*	8.2
1990	45	−3.30	0.79*	6.6	45	2.44	0.49*	9.9
1991	46	−2.75	0.73*	7.2	46	2.17	0.58*	8.7
1992	46	−3.01	0.80*	6.6	46	2.17	0.51*	8.9
1993	46	−3.12	0.81*	7.0	46	2.56	0.59*	9.8
1994	46	−2.94	0.79*	6.5	46	3.14	0.68*	9.0
1995	46	−3.25	0.82*	6.9	46	2.70	0.50*	11.2
1996	46	−3.39	0.76*	7.9	46	2.55	0.73*	7.4
1997	45	−3.43	0.85*	6.1	46	2.89	0.66*	9.2
1998	46	−3.71	0.79*	7.0	45	2.58	0.71*	7.9
1999	46	−2.93	0.78*	7.5	46	2.84	0.73*	8.2
2000	46	−3.04	0.79*	7.3	46	2.34	0.73*	7.6
2001	46	−3.43	0.80*	8.1	46	3.09	0.70*	8.4
2002	46	−4.28	0.79*	9.3	46	2.95	0.77*	7.6
2003	46	−3.71	0.72*	9.8	45	2.41	0.67*	8.0
2004	46	−3.33	0.83*	7.6	46	2.98	0.68*	8.5
2005	45	−2.85	0.82*	6.9	45	3.16	0.74*	7.8
Average	–	–	–	7.1	–	–	–	8.6

*$p < 0.001$

accuracy of predicted BGS/EGS date, measured by the average value of RMSEs for differences between yearly observed and predicted BGS/EGS dates was 7.5 and 8.7 days, respectively (Table 5.2), which is approximately the same with the mean accuracy of simulated BGS/EGS date (Table 5.1). Thus, spatial patterns of yearly *Ulmus pumila* BGS and EGS dates can be effectively simulated and predicted by spatial patterns of yearly mean daily temperatures during the optimum spring and autumn LPs.

Further analysis shows that yearly BGS-temperature spatial regression slope (Table 5.1) correlates significantly negative with yearly regional February-April mean temperature ($P < 0.01$). Thus, a 1 °C spatial shift in daily mean temperature within the optimum spring LP in warmer years with higher regional February-April mean temperatures may induce a larger spatial shift in BGS date than that in colder years with lower regional February-April mean temperatures (Fig. 5.4). However, yearly EGS-temperature spatial regression slope (Table 5.1) does not correlate significantly with yearly regional September-November mean temperature ($P > 0.05$). The dependence of yearly spatial phenology model regression slope on

Table 5.2 External validation of yearly spatial phenology models by spatial extrapolation of yearly *Ulmus pumila* BGS and EGS at the 12–39 external stations (Chen and Xu 2012a)

Year	BGS validation			EGS validation		
	Number of stations	*r*	RMSE (days)	Number of stations	*r*	RMSE (days)
1986	30	0.86**	6.3	28	0.90**	8.6
1987	32	0.78**	8.9	31	0.70**	9.4
1988	32	0.87**	5.7	32	0.87**	8.5
1989	35	0.78**	7.8	34	0.83**	11.0
1990	39	0.76**	7.9	39	0.78**	11.1
1991	38	0.83**	7.4	37	0.87**	8.7
1992	37	0.90**	6.4	36	0.79**	8.5
1993	33	0.92**	5.8	33	0.83**	8.5
1994	18	0.90**	6.0	19	0.66*	11.9
1995	20	0.92**	5.5	19	0.72**	9.0
1996	17	0.90**	5.2	17	0.88**	7.7
1997	16	0.90**	7.0	16	0.84**	6.9
1998	14	0.91**	7.3	16	0.92**	5.0
1999	15	0.91**	6.3	16	0.86**	7.3
2000	12	0.90**	6.7	15	0.89**	6.0
2001	12	0.89**	9.2	14	0.93**	7.7
2002	12	0.89**	11.4	15	0.92**	6.3
2003	13	0.88**	7.2	16	0.64*	11.9
2004	12	0.80*	11.5	15	0.77**	10.2
2005	13	0.73*	11.0	16	0.81**	10.6
Average	–	–	7.5	–	–	8.7

*$p < 0.01$; **$p < 0.001$

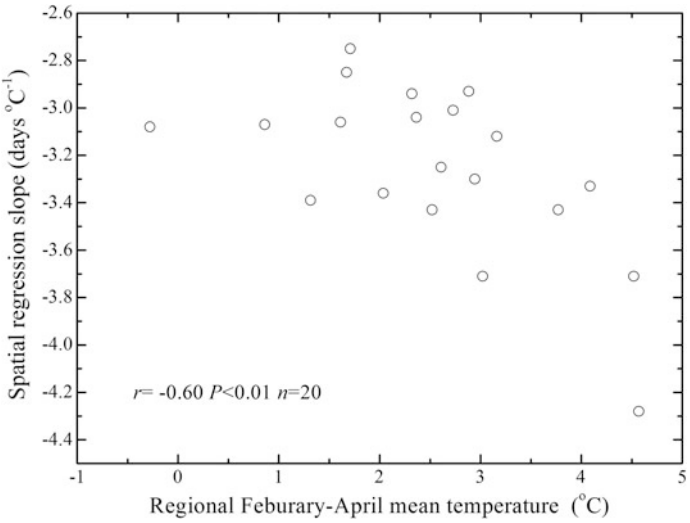

Fig. 5.4 Correlation analysis between regional February-April mean temperature and spring spatial phenology model regression slope (days $°C^{-1}$) across China's temperate zone from 1986 to 2005 [Reprinted from Chen and Xu (2012a), with permission from Elsevier]

yearly regional mean temperature implies that future climate warming in late winter and spring may enhance sensitivity of the spatial response of BGS to temperature, namely, a 1 °C spatial shift in daily mean temperature within the optimum spring LP in the future may induce a larger spatial shift in BGS date than at the present.

The dependence of yearly spatial phenology model regression slope on yearly regional mean temperature can be decomposed into two parts, namely, the dependences of yearly BGS spatial variation (dependent variable of yearly spatial phenology model) and yearly optimum spring LP temperature spatial variation (independent variable of yearly spatial phenology model) on yearly regional mean temperature. A correlation analysis indicates that the spatial standard deviation of yearly BGS correlates significantly positive with yearly regional February-April mean temperature over the 46 stations during 1986–2005 ($P < 0.01$). That is, the higher the regional February-April mean temperature in a year, the larger the spatial standard deviation of BGS in the year (Fig. 5.5). Contrarily, the spatial standard deviation of yearly optimum spring LP temperature does not correlate significantly with yearly regional February-April mean temperature ($P > 0.05$). Thus, the spatial difference of BGS shifted noticeably as the interannual variation of regional mean temperature, while the spatial difference of optimum spring LP temperature did not fluctuate obviously with the interannual variation of regional mean temperature. In other words, sensitivity of the spatial response of yearly BGS to optimum spring LP temperature (yearly BGS-temperature spatial regression slope) is determined mainly by spatial difference of yearly BGS. In this context, future climate warming may enhance sensitivity of the spatial response of BGS to temperature through enlarging BGS spatial difference. As regional climate warming may significantly

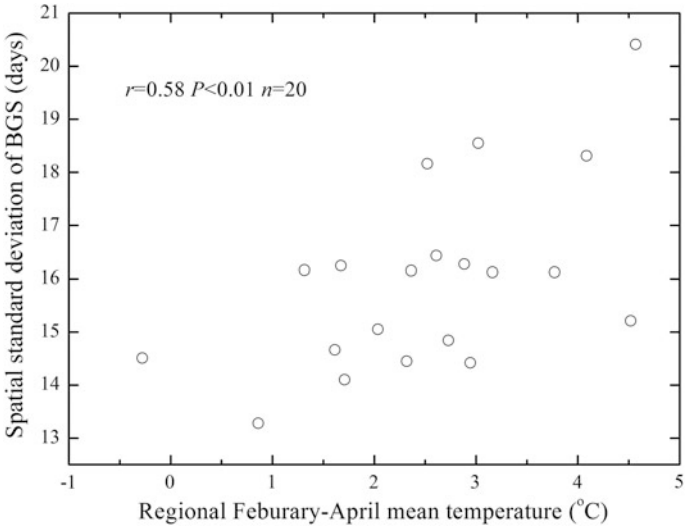

Fig. 5.5 Correlation analysis between regional February-April mean temperature and spatial standard deviation of BGS across China's temperate zone from 1986 to 2005 [Reprinted from Chen and Xu (2012a), with permission from Elsevier]

increase the spatial difference of *Ulmus pumila* BGS and subsequently speed up the spatial response of BGS to temperature, the vegetation dynamics under global climate change scenarios may become more heterogeneous in spatial variation and sensitive in spatial response than at present.

Daily mean air temperature-based spatial phenology models were also created to simulate multi-year mean and yearly spatial patterns of *Robinia pseudoacacia* flowering dates at 26 stations, and validated by extensive spatial extrapolation at 29 stations in eastern China's warm temperate zone during 1986–2005 (Xu et al. 2013). Similar to *Ulmus pumila* leaf unfolding date, a significant negative response of *Robinia pseudoacacia* flowering dates to mean daily temperature during the optimum spring LP was detected ($P < 0.05$–0.001) across the 26 stations from 1986 to 2005. The multi-year mean spatial phenology models explained 87 % of variance in first flowering date with a root mean square error (RMSE) of 2.5 days, 86 % of variance in 50 % flowering date with a RMSE of 2.7 days, and 77 % of variance in the end date of flowering with a RMSE of 4.1 days. The explained variances of yearly spatial phenology models to *Robinia pseudoacacia* flowering dates are between 44–94 % for first flowering date, 57–92 % for 50 % flowering date, and 39–84 % for the end date of flowering, respectively. The corresponding mean RMSEs for differences between observed and simulated flowering dates are 3.9, 4.0 and 5.4 days, respectively. The spatial extrapolation accuracies of the multi-year mean and yearly spatial phenology models for *Robinia pseudoacacia* flowering dates are similar to those for *Ulmus pumila* leaf unfolding date. Overall, the daily mean air temperature-based spatial phenology model can be used to simulate and estimate both growth and reproductive phenology of trees.

References

Chen XQ, Xu L (2012a) Temperature controls on the spatial pattern of tree phenology in China's temperate zone. Agric For Meteorol 154–155:195–202

Chen XQ, Xu L (2012b) Phenological responses of *Ulmus pumila* (Siberian Elm) to climate change in the temperate zone of China. Int J Biometeorol 56:695–706

Chen XQ, Hu B, Yu R (2005) Spatial and temporal variation of phenological growing season and climate change impacts in temperate eastern China. Global Change Biol 11(7):1118–1130

Gong G, Jian W (1983) On the geographical distribution of phenodate in China. Acta Geographica Sinica 38(1):33–40

Nakahara M (1948) Phenology (in Japanese). Kawadesyobo Press, Tokyo

Park-Ono HS, Kawamura T, Yoshino M (1993). Relationships between flowering date of cherry blossom (*Prunus yedoensis*) and air temperature in East Asia. In: Proceedings of the 13th international congress of biometeorology, Calgary

Rötzer T, Chmielewski FM (2001) Phenological maps of Europe. Clim Res 18:249–257

Xu L, Chen XQ, Du X (2013) Simulation and prediction of spatial patterns of *Robinia pseudoacacia* flowering dates in eastern China's warm temperate zone (in Chinese). Acta Ecologica Sinica 33:3584–3593

Chapter 6
Process-Based Simulation and Prediction of Plant Phenology Spatiotemporal Variations

Abstract Using tree first leaf unfolding and grass green-up data, and daily air temperature and precipitation data, local and regional unified phenology models were fitted and validated in northern China and the Inner Mongolian Grassland, respectively. Based on the regional phenology models, spatiotemporal patterns of first leaf unfolding dates and green-up dates were reconstructed over the continuous geographic coverage. Within the 250 optimum local first leaf unfolding models for the four tree species at 136 stations, the unified forcing and chilling models account for 83 and 17 %, respectively. Thus, forcing temperature predominantly influence first leaf unfolding dates in most parts of northern China, while the affect of chilling temperature was stronger for earlier than later first leaf unfolding species. Spatial and temporal validation confirmed the capability and reliability of the 16 regional unified species-specific models in predicting leaf unfolding dates in the four climate regions. The reconstructed leaf unfolding dates show a significant advancement in most parts of northern China over 1960–2009, which is stronger for earlier than later first leaf unfolding species. For grass green-up modeling, previous temperature accumulation controls green-up dates of the three grass species at three stations, while both previous temperature and precipitation accumulations control green-up dates of these grass species at another three stations. The accumulated precipitation plays a more important role as the precondition of forcing temperature than as the supplementary condition of forcing temperature in triggering green-up of grasses. The accuracy of the regional unified models in simulating and predicting green-up dates of grasses at internal and external stations is at acceptable levels overall. The reconstructed mean green-up dates for the three grass species represented a similar spatial pattern across the Inner Mongolian Grassland, which is aligned approximately along the thermal and moisture gradient. Spatial patterns of green-up date linear trends indicate a significant advancement at 40.3–71.4 % of all grids over the Inner Mongolian Grassland during 1983–2009.

Keywords *UniForc* model · *UniChill* model · Traditional thermal time model · Air temperature-precipitation parallel model · Air temperature-precipitation sequential model · Regional unified model · Spatiotemporal patterns

X. Chen, *Spatiotemporal Processes of Plant Phenology*,
SpringerBriefs in Geography, DOI 10.1007/978-3-662-49839-2_6

6.1 Introduction

Statistical phenology models are probabilistic and based on statistical hypotheses. Parameters of statistical models are estimated from empirical data using various statistical fitting methods (Chuine et al. 2003). Because these models may not consider biological processes, they can only fit the specific sample dataset of a given phenological occurrence date by means of climatic factors, but normally cannot be used to extrapolate and predict the phenological occurrence date beyond the time period of model fitting. By contrast, mechanistic (or process-based) phenology models are causal and based on physiological and ecological hypotheses. The known or assumed cause-effect relationships between biological processes and driving factors in the plant's environment should be included in a mechanistic model only if information on its impacts on the process is available. Although parameters of mechanistic models have physical dimensions that can theoretically be measured directly instead of being estimated by fitting, this is rarely possible in the practice (Chuine et al. 2003). Generally speaking, this type of phenology models may not only simulate the specific sample dataset of a given phenological occurrence date by means of climatic factors but also predict phenological occurrence dates beyond the time period of model fitting.

So far, most of mechanistic phenology models have been created for fitting and predicting spring phenology of individual trees at station scales, such as budburst, leaf unfolding and flowering dates (Landsberg 1974; Cannell and Smith 1983; Murray et al. 1989; Hänninen 1990; Kramer 1994a; Chuine et al. 1998; Linkosalo et al. 2008; Morin et al. 2009; Fu et al. 2012; Xu and Chen 2013). The basic hypothesis of local species-specific phenology models is that spring tree phenology is triggered mainly by chilling temperatures during the previous autumn and winter, and forcing temperatures during the current spring (Chuine 2000). The simplest models are only based on the accumulation of forcing temperatures that induce plant growth and reproduction after bud dormancy has been broken in spring (Cannell and Smith 1983; Hunter and Lechowicz 1992; Chuine et al. 1999). More sophisticated models are based on the accumulation of both chilling temperatures and forcing temperatures. Because chilling temperatures may influence bud dormancy and accelerate bud growth from the state of quiescence to the state of budburst, the negative relationship between the state of forcing and the state of chilling has been considered in these models, namely, the less chilling temperatures are received, the more forcing temperatures are subsequently needed to trigger budburst (Cannell and Smith 1983; Murray et al. 1989; Kramer 1994b; Chuine 2000).

Applications of these spring phenology models have been restricted to the relevant phenological event occurrence date at given locations (Chuine et al. 1998, 1999). However, as plant phenology has found a renewal in the context of global climate change, there is an urgent need for simulating and predicting phenological event occurrence dates at regional scales (Chuine et al. 2000). For meeting the needs, regional unified species-specific models should be developed by upscaling species-specific phenology models from individual stations to a region. A regional

unified species-specific model assumes that responses of a phenological event occurrence date to temperature at various stations are not significantly different within the same climate region (Xu and Chen 2013).

Moreover, most phenology models were developed for tree species, rather than non-woody species (Chuine et al. 2003). In comparison with forests, grasslands are one of the most widespread vegetation types worldwide, and play a major but poorly defined role in the global carbon cycle and climate change. As seasonal distribution of rainfall is a major determinant of plant development and production in many semiarid and arid regions (Hall et al. 2000), the moisture factors should be taken into account in the grass phenology models. Thus, how to couple seasonal precipitation to temperature-based models is the key difficulty. Unfortunately, there is no a consistent pattern of seasonal precipitation impacts on grass phenology over different grassland ecosystems (Cleland et al. 2006; Sherry et al. 2007; Shinoda et al. 2007; Jentsch et al. 2009; Crimmins et al. 2010, 2011; Lesica and Kittelson 2010). Examining the combined effects of air temperature and precipitation during late winter and early spring on green-up date of the dominant grass species by means of process-based models is crucial not only for revealing ecological mechanisms of grassland phenology, but also for predicting appropriate grazing and harvesting times, as well as estimating net primary productivity and carbon sequestration in grassland ecosystems (Chen et al. 2014).

6.2 Leaf Unfolding Simulation and Prediction Across Northern China

6.2.1 Study Area and Tree Species

The study area is located in northern China's temperate zone, which includes cold temperate, humid/sub-humid middle temperate, humid/sub-humid warm temperate, semi-arid middle/warm temperate, and arid middle/warm temperate regions (Fig. 6.1, China Meteorological Administration 1978). As no phenological stations are located in the cold temperate region, only four climate regions were involved.

Salix matsudana, *Populus simonii*, *Ulmus pumila* and *Prunus armeniaca* were chosen as indicator plant species because they are all native deciduous trees and grow broadly in the study area. To reconstruct phenological time series for the four tree species at grid scales, their possible distribution areas were determined according to species distribution altitude limits and desert boundaries.

6.2.2 Phenological and Climate Data

The first leaf unfolding data for *Salix matsudana*, *Populus simonii*, *Ulmus pumila* and *Prunus armeniaca* were acquired from the China Meteorological Administration

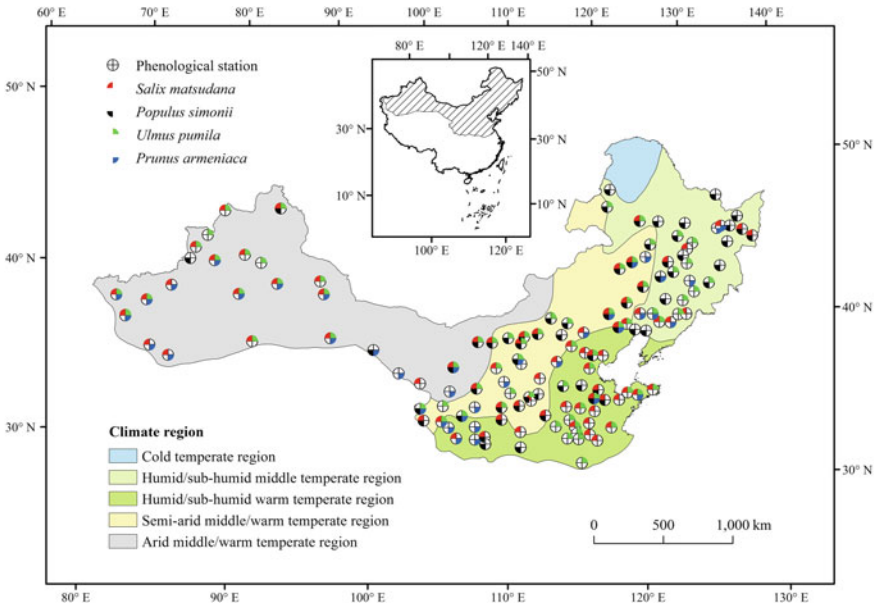

Fig. 6.1 Location of phenological stations with the four tree species observations in different climate regions [Reprinted from Xu and Chen (2013), with permission from John Wiley and Sons]

(Chen 2009). Altogether, 136 stations (with phenological time series of more than 10 years from 1981 to 2005) were selected for first leaf unfolding modeling. The number of stations is different for the four tree species, namely, 77 stations for *Salix matsudana*, 61 stations for *Populus simonii*, 72 stations for *Ulmus pumila*, and 40 stations for *Prunus armeniaca* (Fig. 6.1).

Climate data were obtained from the China Meteorological Data Sharing Service System (http://cdc.cma.gov.cn/), including daily mean air temperature at 343 meteorological stations in the northern China's temperate zone over the 1959-2009 period. For reconstructing spatiotemporal patterns of first leaf unfolding dates at grid scales, daily mean air temperatures were interpolated into 8 km × 8 km grids over the study area using ANUSPLIN 4.2 (Hutchinson 2002) and Digital Elevation Model (DEM) data derived from the United States Geological Survey. Meanwhile, gridded daily mean air temperature data at a few phenological stations without meteorological observations were also produced and used.

6.2.3 Phenology Models

The *UniForc* and *UniChill* models (Chuine 2000) were employed to fit first leaf unfolding time series of the four tree species at each station from 1981 to 2005. The *UniForc* model considers only the effect of forcing temperatures during spring. The

assumption is that first leaf unfolding appears when the state of forcing, S_f, reaches a critical value F^* on the date of y (Eq. 6.1):

$$S_f = \sum_{t_1}^{y} R_f(x_t) = F^* \tag{6.1}$$

The state of forcing is defined as a daily accumulation of the rate of forcing, $R_f(x_t)$, which begins at t_1 (day of year, DOY). The rate of forcing is an exponential function and x_t is the daily mean air temperature (Eq. 6.2):

$$R_f(x_t) = \frac{1}{1 + e^{d(x_t - e)}} \tag{6.2}$$

The *UniForc* model includes four parameters where t_1 is usually set on 1 January and d, e and F^* were fitted, with $d < 0$ and $e > 0$.

The *UniChill* model considers the effect of both chilling temperatures during the dormancy period and forcing temperatures during the growth period. The hypothesis is that dormancy breaks when the state of chilling, S_c, reaches a critical value C^* on the date of t_1 (Eq. 6.3):

$$S_c = \sum_{t_0}^{t_1} R_c(x_t) = C^* \tag{6.3}$$

The state of chilling is defined as a daily accumulation of the rate of chilling, $R_c(x_t)$, which begins at t_0 (DOY). The rate of chilling is also an exponential function and x_t is the daily mean air temperature (Eq. 6.4):

$$R_c(x_t) = \frac{1}{1 + e^{a(x_t - c)^2 + b(x_t - c)}} \tag{6.4}$$

On the date of t_1, forcing units start to accumulate until it reaches a critical value F^* (Eqs. 6.1 and 6.2). The *UniChill* model contains seven fitted parameters, in which a, b, c, C^* pertain to the chilling function and d, e, F^*, belong to the forcing function. t_0 is commonly fixed on 1 September of the preceding year.

The species-specific parameters of *UniForc* and *UniChill* models at a station were determined by the lowest value of the root mean square error (RMSE, Eq. 6.5), while the optimum local model (*UniForc* or *UniChill*) was selected by the lowest value of the Akaike Information Criterion (AIC, Eq. 6.6) (Akaike 1973). In addition, the Nash–Sutcliffe Efficiency index (NSE, Eq. 6.7) (Nash and Sutcliffe 1970) was used to assess the reliability of model validation in the spatial extrapolation in comparison with the null model (mean dates of first leaf unfolding). A negative NSE value denotes that the model performs worse than the null model, whereas a positive NSE value (with a maximum value of 1) indicates that the model

explains more variance than the null model. Moreover, the closer the NSE value to 1, the higher the model reliability, while the closer the NES value to 0, the lower the model reliability.

$$\mathrm{RMSE} = \sqrt{\frac{\sum_{i=1}^{n} (obs_i - pre_i)^2}{n}} \tag{6.5}$$

$$\mathrm{AIC} = n \times \ln\left(\frac{\sum_{i=1}^{n} (obs_i - pre_i)^2}{n}\right) + 2(k+1) \tag{6.6}$$

$$\mathrm{NSE} = 1 - \frac{\sum_{i=1}^{n} (obs_i - pre_i)^2}{\sum_{i=1}^{n} \left(obs_i - \overline{obs}\right)^2} \tag{6.7}$$

where obs_i is the observed value in year i; pre_i is the simulated (or predicted) value in year i; $\overline{obs}$ is mean observed value in the validation period; n is the number of years; k is the number of parameters (Xu and Chen 2013).

6.2.4 Local First Leaf Unfolding Modeling

Within the selected 250 optimum models for the four tree species at 136 stations, the *UniForc* model accounts for 83 % (207 models), which implies that forcing temperature predominantly influence first leaf unfolding date of the four tree species in most parts of northern China's temperate zone. For the rest 43 optimum models (17 % of total) in the form of *UniChill*, the number and percentage of stations with effective chilling temperature steadily decreases from earlier first leaf unfolding tree species (such as *Salix matsudana* and *Populus simonii*) to later first leaf unfolding tree species (such as *Ulmus pumila* and *Prunus armeniaca*), namely, 18 stations (23 % of 77) for *Salix matsudana*, 13 stations (21 % of 61) for *Populus simonii*, 11 stations (15 % of 72) for *Ulmus pumila* and 1 station (3 % of 40) for *Prunus armeniaca*. This indicates that the influence of chilling temperature on first leaf unfolding date was stronger for earlier first leaf unfolding species than later first leaf unfolding species in northern China. The RMSEs for differences between observed and simulated first leaf unfolding dates range from 0.7 days to 10.2 days for the 250 optimum models, and the mean RMSE is 3.7 days (Xu and Chen 2013).

6.2.5 Regional Unified First Leaf Unfolding Modeling

Regional unified models were selected from optimum local species-specific models based on their capability in the spatial extrapolation. For achieving this goal, each

optimum local species-specific model was employed to extrapolate first leaf unfolding dates of corresponding species at all other stations within its located climate region during 1981–2005. The extrapolation errors were evaluated by NES and RMSE, and the best local species-specific model with effective extrapolation (NSE > 0) and the lowest value of the RMSE was determined as the regional unified model for each species and each climate region (Table 6.1). Within the 16 regional unified models, only the model for *Salix matsudana* first leaf unfolding in the humid/sub-humid middle temperate region contains both chilling and forcing temperature accumulations (*UniChill* model), while the other 15 models require only forcing temperature accumulation (*UniForc* model). The mean RMSE of each regional unified model at stations with effective extrapolation ranges from 3.3 to 6.0 days (Table 6.1).

The temporal validation of the 16 regional unified models in years beyond the time period of model fitting shows that the observed first leaf unfolding date correlates significant positively ($P < 0.01$) with the predicted first leaf unfolding date

Table 6.1 Regional unified models and their assessments in spatial extrapolation over 1981–2005 for the four tree species in the four climate regions (Xu and Chen 2013)

Species	Climate region	Number of stations	Regional unified models	Number of stations with NSE > 0	Percentage (%)	Mean RMSE*
Salix matsudana	HSMT	10	*UniChill*	8	80	5.44
	HSWT	25	*UniForc*	16	64	6.01
	SMWT	22	*UniForc*	12	55	5.79
	AMWT	20	*UniForc*	14	70	3.57
Populus simonii	HSMT	19	*UniForc*	12	63	4.45
	HSWT	13	*UniForc*	11	85	5.80
	SMWT	24	*UniForc*	17	71	4.33
	AMWT	5	*UniForc*	3	60	3.43
Ulmus pumila	HSMT	11	*UniForc*	9	82	5.97
	HSWT	19	*UniForc*	14	74	5.70
	SMWT	24	*UniForc*	14	58	5.17
	AMWT	18	*UniForc*	8	44	4.95
Prunus armeniaca	HSMT	7	*UniForc*	7	100	4.94
	HSWT	8	*UniForc*	6	75	4.91
	SMWT	10	*UniForc*	6	60	3.80
	AMWT	15	*UniForc*	10	67	3.32

HSMT humid/sub-humid middle temperate region, *HSWT* humid/sub-humid warm temperate region, *SMWT* semi-arid middle/warm temperate region, *AMWT* arid middle/warm temperate region

*Mean RMSE at stations with NSE > 0

during 2006–2009 in 15 of 16 models. The RMSE of each regional unified model in the temporal validation ranges from 2.0 and 10.6 days (Fig. 6.2). As the mean RMSEs of temporal validation for each tree species in the four climate regions (Fig. 6.2) are only slightly larger (0.4–1.6 days) than those of spatial validation for each tree species in the four climate regions (Table 6.1), the process-based regional unified models provide a robust tool for predicting first leaf unfolding dates of the four tree species in northern China's temperate zone.

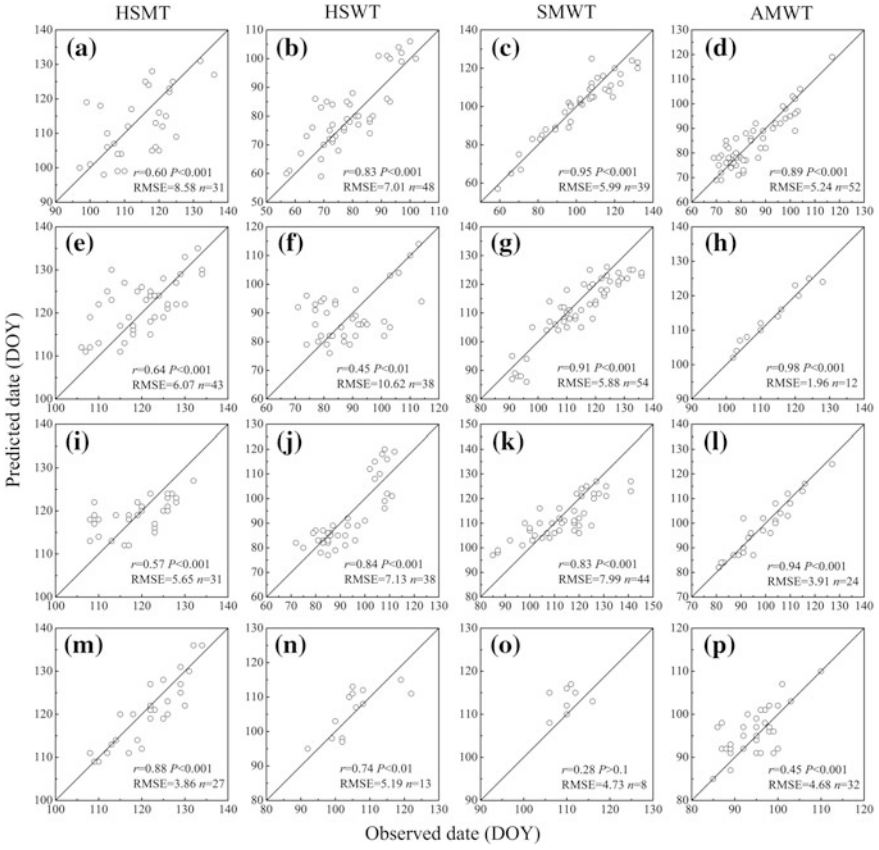

Fig. 6.2 Comparison between observed first leaf unfolding date and predicted first leaf unfolding date based on regional unified species-specific models in the four climate regions during 2006–2009. **a–d** *Salix matsudana*, **e–h** *Populus simonii*, **i–l** *Ulmus pumila*, **m–p** *Prunus armeniaca* [Reprinted from Xu and Chen (2013), with permission from John Wiley and Sons]

6.2.6 Spatiotemporal Patterns of First Leaf Unfolding Dates

Based on the 16 regional unified species-specific models, long-term first leaf unfolding dates for the four tree species across northern China have been reconstructed using gridded daily mean temperature data from 1959 to 2009. At the grid level, a significantly advancing trend in first leaf unfolding dates was detected in most parts of the possible distribution area of each tree species over 1960–2009. It should be noted that the spatial differentiation in linear trends of first leaf unfolding dates decreases gradually from the earlier to the later first leaf unfolding species (Fig. 6.3).

At the climate region level, first leaf unfolding dates of the four tree species display a synchronously significant advancement ($P < 0.001$) from 1960 to 2009 with trend values ranging from −1.2 days per decade to −2.2 days per decade (Fig. 6.4).

Across northern China's temperate zone, regional mean first leaf unfolding dates advanced significantly ($P < 0.001$) at a slowing rate from earlier first leaf unfolding species to later first leaf unfolding species, namely, –1.61 days per decade for *Salix matsudana*, –1.59 days per decade for *Populus simonii*, –1.41 days per decade for *Ulmus pumila*, and –1.39 days per decade for *Prunus armeniaca* during 1960–2009.

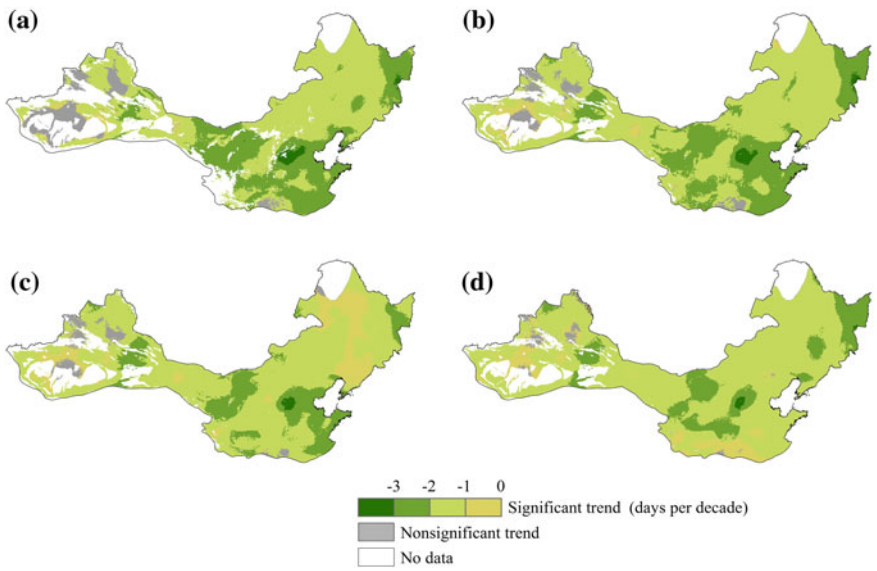

Fig. 6.3 Spatial pattern of linear trends in first leaf unfolding dates in northern China's temperate zone over 1960–2009. **a** *Salix matsudana*, **b** *Populus simonii*, **c** *Ulmus pumila*, **d** *Prunus armeniaca* [Reprinted from Xu and Chen (2013), with permission from John Wiley and Sons]

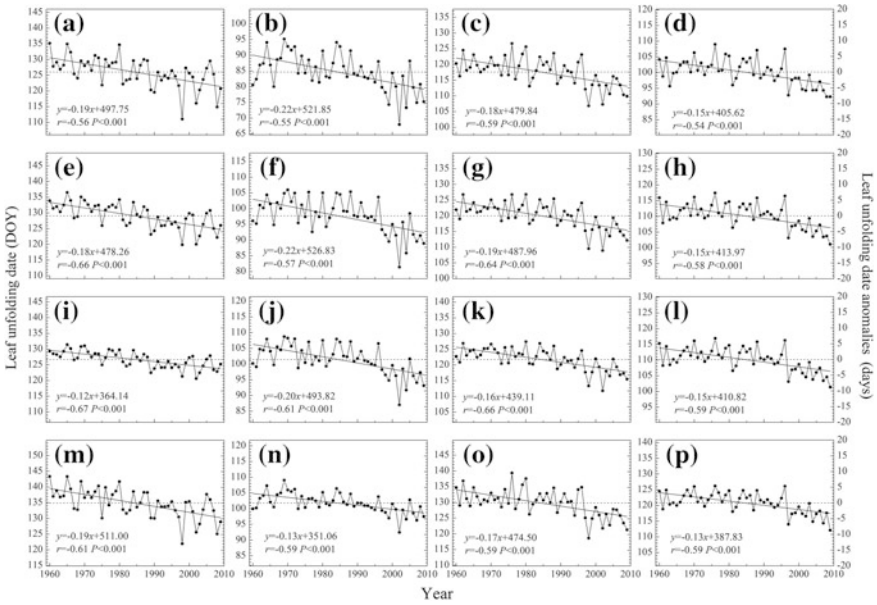

Fig. 6.4 Linear trends in first leaf unfolding dates of the four tree species in the humid/subhumid middle temperate region (HSMT, first column), humid/subhumid warm temperate region (HSWT, second column), semiarid middle/warm temperate region (SMWT, third column), and arid middle/warm temperate region (AMWT, fourth column) over 1960–2009. **a–d** *Salix matsudana*, **e–h** *Populus simonii*, **i–l** *Ulmus pumila*, **m–p** *Prunus armeniaca* [Reprinted from Xu and Chen (2013), with permission from John Wiley and Sons]

6.3 Green-up Simulation and Prediction in the Inner Mongolian Grassland

6.3.1 Study Area and Grass Species

The Inner Mongolia Autonomous Region is located in temperate northern China (Fig. 6.5). Influenced by both East Asian monsoon along the east coast and inland drought in the west, the climate can be divided into temperate subhumid, semiarid and arid regions from east to west (China Meteorological Administration 1978). The topographical structure is composed of the Inner Mongolian Plateaus with an average height of 1000 m above sea level and the surrounding catenulate mountains at 1000–2500 m above sea level. The annual mean air temperature increases from −5 °C in the northeast to 10 °C in the southwest, while the annual mean total precipitation decreases from 530 mm in the east to 35 mm in the west. Along with the thermal-moisture gradient, the vegetation contains six belts from northeast to southwest, namely, coniferous forest, deciduous broadleaf forest, forest steppe,

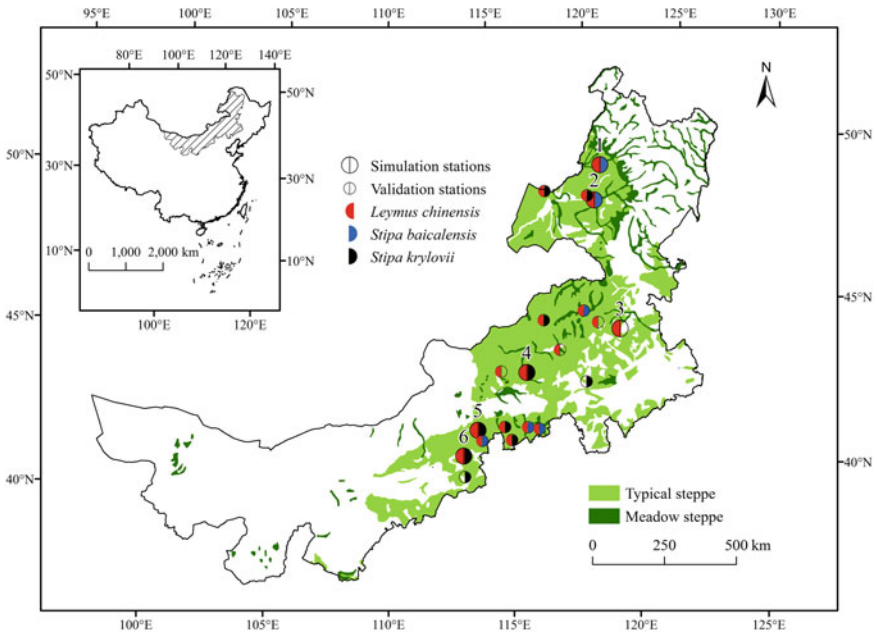

Fig. 6.5 Location of phenological stations with the three dominant grass species observations in the Inner Mongolian Grassland

typical steppe, desert steppe, and desert (Editorial Board of the Inner Mongolian Grassland 1991). In addition, some intrazonal vegetation types are distributed across lowland, sand plain and mountainous areas, such as meadow steppe and subshrubs. Because typical steppe and meadow steppe are characterized by good nutritional quality, high productivity, mowing suitability, and strong palatability, they are the most important pasture in the temperate zone of China. Six grassland meteorological experiment stations were selected for process-based modeling, in which E'ergunayouqi, Ewenkeqi and Bayartuhushuo are located in the meadow steppe areas, while Xilinhot, Xianghuangqi and Chaharyouyihouqi lie in the typical steppe areas (Fig. 6.5). Geo-location parameters and thermal-moisture conditions of the six stations are listed in Table 6.2. At these stations, three dominant grass species in the Inner Mongolian Grassland (*Leymus chinensis*, *Stipa baicalensis* and *Stipa krylovii*) were chosen as indicator species for process-based modeling.

6.3.2 Phenological and Climate Data

The phenological data include green-up dates of the three grass species at six grassland meteorological experiment stations from 1983 to 2009 and at 14 ecological stations from 2005 to 2009. The phenological observation was carried out in

Table 6.2 Geo-location parameters and thermal-moisture conditions at each station (Chen et al. 2014)

Station	Number[a]	North latitude	East longitude	Elevation (m a.s.l)	Annual mean temperature (°C)	Annual precipitation (mm)
E'ergunayouqi	1	50°15′	121°11′	582	−2.0	375.9
Ewenkeqi	2	49°09′	119°45′	621	−1.0	344.9
Bayartuhushuo	3	45°04′	120°20′	629	3.8	438.9
Xilinhot	4	43°57′	116°04′	991	3.0	269.9
Xianghuangqi	5	42°14′	113°50′	1323	3.9	272.0
Chaharyouyihouqi	6	41°27′	113°11′	1425	4.2	325.7

[a] The station number is the same as in Fig. 6.5

natural pastures with an area of 10000 m^2 at each station. The green-up of a grass species is identified when 10 % of individual grasses display green leaves and grow up to one centimeter in spring or early summer (China Meteorological Administration 1993; Study Group of Animal Husbandry Climate Regionalization for China's Pastoral Areas 1988). As different species have different distribution ranges, observed green-up data of the three grass species are not identical at each station. Namely, *Leymus chinensis* has been observed at the six grassland meteorological experiment stations in both typical and meadow steppe areas, while *Stipa baicalensis* and *Stipa krylovii* have been observed at E'ergunayouqi and Ewenkeqi in meadow steppe areas, and at Xilinhot, Xianghuangqi and Chaharyouyihouqi in typical steppe areas, respectively (Fig. 6.5).

Statistical analysis shows that mean green-up dates of *Leymus chinensis* occurred during 17 April to 6 May with standard deviations (SD) between 4.5 and 6.9 days over the six stations, while mean green-up dates of *Stipa baicalensis* and *Stipa krylovii* appeared during 1 May to 7 May with a SD of 5.0 days at E'ergunayouqi and Ewenkeqi, and during 15 April to 28 April with SDs between 4.5 and 7.1 days at Xilinhot, Xianghuangqi and Chaharyouyihouqi, respectively. A significant advancement in green-up date ($P < 0.01$–0.001) was detected at Chaharyouyihouqi for *Leymus chinensis* and *Stipa krylovii* from 1983 to 2009, while a significant delay ($P < 0.05$) was found at Xilinhot for *Stipa krylovii* (Table 6.3).

Daily mean air temperature and daily precipitation data at 118 meteorological stations during 1983–2009 were collected for green-up modelling. In order to reconstruct time series of grass green-up dates over a continuous geographic coverage, the climate data interpolation package ANUSPLIN 4.2 (Hutchinson 2002) and Digital Elevation Model (DEM) data derived from the US Geological Survey were used to interpolate the daily mean air temperature and daily precipitation into 8 km × 8 km grids over the Inner Mongolia Autonomous Region.

Table 6.3 Statistical characteristic values of green-up dates of the three grass species at each station during 1983–2009 (Chen et al. 2014)

Station number[a]	Species	Number of years	Mean date (day of year)	Standard deviation (days)	Linear trends (days per decade)
1	*L. chinensis*	22	126	4.5	1.98
	S. baicalensis	24	127	5.0	–0.63
2	*L. chinensis*	21	120	4.5	0.30
	S. baicalensis	19	121	5.0	1.35
3	*L. chinensis*	16	112	4.9	–1.83
4	*L. chinensis*	17	109	5.1	–1.23
	S. krylovii	21	105	6.5	4.85*
5	*L. chinensis*	23	107	5.0	–0.09
	S. krylovii	23	106	4.5	1.69
6	*L. chinensis*	24	118	6.9	–5.45***
	S. krylovii	24	118	7.1	–4.63**

*$P < 0.05$, ** $P < 0.01$, *** $P < 0.001$

[a]The station number is the same as in Fig. 6.5

6.3.3 Phenology Models

To examine the combined effects of air temperature and precipitation on green-up date of the dominant grass species, traditional thermal time model and two revised thermal time models coupling air temperature and precipitation were employed to fit green-up dates of *Leymus chinensis*, *Stipa baicalensis* and *Stipa krylovii*.

The traditional thermal time model considers only the effect of forcing air temperatures during spring. The hypothesis is that green-up appears when the state of forcing, S_T, reaches a critical value F^* on the date of y (Eq. 6.8):

$$S_T = \sum_{t_0}^{y} R_T(T_t) = F^* \tag{6.8}$$

The state of forcing is defined as a daily accumulation of the rate of forcing above a base air temperature T_b, $R_T(T_t)$, which starts at t_0 (DOY) and T_t is the daily mean air temperature. The rate of forcing in the traditional thermal time model is defined by Eq. 6.9:

$$R_T(T_t) = \begin{cases} 0 & T_t \le T_b \\ T_t - T_b & T_t > T_b \end{cases} \tag{6.9}$$

This model contains three parameters where the starting date of the temperature accumulation (t_0) was fixed on 1 January, and the base temperature (T_b) and the critical value of state of forcing (F^*) were fitted.

The revised thermal time model considers the effects of both forcing air temperatures and precipitations from 1 January to green-up date. According to the field observations during 2004–2006 in Ewenkeqi, accumulated late winter and early spring precipitation, usually falling as snow, is at least as important as spring temperature in triggering green-up of grass species (Chen et al. 2008). A statistical analysis in the Mongolian Grasslands has also shown that precipitation or snow melt events in spring could trigger grass to start growing (Shinoda et al. 2007). One possible explanation for this association is that grass roots cannot start to grow until the ground has been warmed and humidified above 0 °C, after snow melt. Namely, more snow fall during late winter and early spring can mean more soil moisture storage as spring temperature increases, and induce earlier green-up, whereas less snow fall during late winter and early spring can create a soil moisture shortage coupling with rapid spring temperature increases, and force later green-up. The revised thermal time model assumes therefore that green-up of grasses is triggered by accumulated spring air temperature and accumulated late winter and early spring precipitation in the form of snow. This model contains two approaches.

The air temperature-precipitation parallel model assumes that accumulated air temperature and precipitation are equivalently important in triggering green-up of grasses. That is, green-up occurs when the state of forcing air temperature, S_T and the state of forcing precipitation, S_P, achieve critical values F^* and P^*on the date of y (Eqs. 6.8 and 6.10):

$$S_P = \sum_{t_0}^{y} R_P(P_t) = P^* \tag{6.10}$$

The state of precipitation is defined as a daily accumulation of the rate of precipitation, R_p (P_t), which starts at t_0 (DOY) and P_t is the daily precipitation (mm). Here, the starting date of precipitation accumulation was also set as 1 January (t_0). The rate of precipitation in the air temperature-precipitation parallel model is defined by Eq. 6.11:

$$R_P(P_t) = P_t \tag{6.11}$$

There are three fitted parameters in the air temperature-precipitation parallel model, namely, T_b, F^* and P^*.

The air temperature-precipitation sequential model assumes that air temperature and precipitation trigger green-up of grasses sequentially, namely, the effect of

forcing air temperature on green-up occurs when the state of forcing precipitation, S_P, achieves critical value P^*on the date of t_1 (Eq. 6.12):

$$S_P = \sum_{t_0}^{t_1} R_P(P_t) = P^* \tag{6.12}$$

The state of precipitation is defined as a daily accumulation of the rate of precipitation, R_p (P_t), which starts at t_0 (DOY) and terminates at t_1 (DOY). The rate of precipitation in the air temperature-precipitation sequential model is also defined by Eq. 6.11. The time point t_1 represents not only the end date of precipitation accumulation but also the starting date of temperature accumulation. The air temperature-precipitation sequential model contains also three fitted parameters T_b, $F^*$and P^*. Because grass green-up appeared after the date daily mean air temperature rose above 0 °C and before the date daily mean air temperature surpassed 5 °C (Study Group of Animal Husbandry Climate Regionalization for China's Pastoral Areas 1988), a candidate range of T_b was set between daily mean air temperatures of 0 and 5 °C (Chen et al. 2014).

The species-specific parameters of the traditional thermal time model and the revised thermal time models coupling air temperature and precipitation were determined by the lowest value of the RMSE (Eq. 6.5), while the optimum local model (traditional thermal time model or one of the revised thermal time models coupling air temperature and precipitation) was selected by the lowest value of AIC (Eq. 6.6).

To assess performances of the regional unified models in spatial extrapolation, these models were validated by predicting green-up dates of the three grass species from 2005 to 2009 at the 14 external stations within the research region (Fig. 6.5). The precision of the spatial validation was evaluated by correlation coefficient and RMSE between observed and predicted green-up dates.

6.3.4 Local Green-up Modeling

Within the 11 optimum models for the three grass species at six stations, six models belong to the traditional thermal time model. They were created at E'ergunayouqi, Ewenkeqi and Chaharyouyihouqi (Table 6.4). This indicates that late winter and early spring precipitation did not significantly influence green-up dates of the three grass species at these three locations. The RMSEs for *Leymus chinensis* green-up modeling ranged from 3.6 to 5.8 days, whereas the RMSEs for *Stipa baicalensis* and *Stipa krylovii* green-up modeling were between 4.0 and 5.6 days. Moreover, the traditional thermal time model can explain 48 % (R^2, $P < 0.001$) and 47 % ($P < 0.001$) of the observed interannual variations in *Leymus chinensis* and *Stipa baicalensis* green-up dates at Ewenkeqi, and 57 % ($P < 0.001$) and 40 %

($P < 0.001$) of the observed interannual variations in *Leymus chinensis* and *Stipa krylovii* green-up dates at Chaharyouyihouqi, respectively. In contrast, coefficients of determination (R^2) between observed and predicted *Leymus chinensis* green-up dates and between observed and predicted *Stipa baicalensis* green-up dates are only 4 and 14 % ($P > 0.05$), respectively at E'ergunayouqi, which implies that the traditional thermal time model cannot effectively explain the observed interannual variations in *Leymus chinensis* and *Stipa baicalensis* green-up dates there (Table 6.4).

The green-up dates of *Leymus chinensis* and *Stipa krylovii* at Bayartuhushuo, Xilinhot and Xianghuangqi were best fitted by the revised thermal time models coupling air temperature and precipitation, including four air temperature-precipitation sequential models and one air temperature-precipitation parallel model. The RMSEs for *Leymus chinensis* green-up modeling ranged from 3.1 to 6 days over the three stations, whereas the RMSEs for *Stipa krylovii* green-up modeling were 6.3 days at both Xilinhot and Xianghuangqi. Thus, accumulated late winter and early spring precipitation might be the precondition (sequential model) or supplementary condition (parallel model) of the dominant effect of forcing temperature in triggering green-up of grass species at these three locations. Coefficients of determination (R^2) show that the optimum revised thermal time models can explain 68 % ($P < 0.001$) of the observed interannual variation in *Leymus chinensis* green-up date at Bayartuhushuo, and 63 % ($P < 0.001$) and 23 % ($P < 0.05$) of the observed interannual variations in *Leymus chinensis* and *Stipa*

Table 6.4 Parameters and simulation accuracies of optimum local species-specific models (Chen et al. 2014)

Station number	Species	Optimum model[a]	T_b (°C)	F^* (°C)	P^* (mm)	R^2	RMSE (days)
1	*L. chinensis*	M_t	0.0	119.1	–	0.04	5.8
	S. baicalensis	M_t	0.2	135.3	–	0.14	5.2
2	*L. chinensis*	M_t	0.0	105.8	–	0.48^{***}	3.6
	S. baicalensis	M_t	0.1	117.9	–	0.47^{***}	4.0
3	*L. chinensis*	$M_{t\text{-}p2}$	0.2	97.0	2.0	0.68^{***}	3.1
4	*L. chinensis*	$M_{t\text{-}p1}$	2.5	42.5	5.9	0.63^{***}	3.6
	S. krylovii	$M_{t\text{-}p2}$	0.1	52.6	5.1	0.23^{*}	6.3
5	*L. chinensis*	$M_{t\text{-}p2}$	0.0	105.1	2.5	0.07	6.0
	S. krylovii	$M_{t\text{-}p2}$	0.1	89.8	3.0	0.01	6.3
6	*L. chinensis*	M_t	0.0	185.6	–	0.57^{***}	4.5
	S. krylovii	M_t	0.2	170.1	–	0.40^{***}	5.6

[a]M_t traditional thermal time model, $M_{t\text{-}p1}$ air temperature-precipitation parallel model, $M_{t\text{-}p2}$ air temperature-precipitation sequential model

$^*P < 0.05$, $^{**}P < 0.01$, $^{***}P < 0.001$

krylovii green-up dates at Xilinhot. However, R^2 values between observed and predicted *Leymus chinensis* green-up dates and between observed and predicted *Stipa krylovii* green-up dates are only 7 and 1 % ($P > 0.05$), respectively at Xianghuangqi, which means that the air temperature-precipitation sequential model cannot effectively explain the observed interannual variation in *Leymus chinensis* and *Stipa krylovii* green-up dates at that location (Table 6.4).

Overall, parameter estimates of the optimum local species-specific models show that T_b and F^* ranged from 0 to 2.5 °C and from 42.5 to 185.6 °C, respectively, while P^* ranged from 2 to 5.9 mm (Table 6.4). As F^* values of the traditional thermal time model are generally larger than those of the air temperature-precipitation parallel and sequential models, precipitation has compensation effects to air temperature in triggering green-up of grass species. Simulation errors for the 11 optimum local species-specific models, as measured by RMSE are between 3.1 and 6.3 days, and the mean RMSE is 4.9 days.

6.3.5 Regional Unified Green-Up Modeling

The basic hypothesis for regional green-up modeling is that local model estimates of green-up response to climatic factors for a grass species are not significantly different within its distribution range, based on which regional models can be constructed by pooling time series of species-specific green-up dates from different sample stations (García-Mozo et al. 2008; Delpierre et al. 2009). For *Leymus chinensis* green-up modeling, time series of green-up dates from all six sample stations within the research region were combined. For *Stipa baicalensis* and *Stipa krylovii* green-up modeling however, time series of green-up dates from E'ergunayouqi and Ewenkeqi within meadow steppe areas, and from Xilinhot, Xianghuangqi and Chaharyouyihouqi within typical steppe areas were merged, respectively. Results show that the traditional thermal time model has higher simulation parsimony and efficiency than the revised thermal time models coupling air temperature and precipitation for *Stipa baicalensis*. By contrast, the revised thermal time models coupling air temperature and precipitation has higher simulation parsimony and efficiency than the traditional thermal time model for *Leymus chinensis* (air temperature-precipitation parallel model) and *Stipa krylovii* (air temperature-precipitation sequential model). Simulation errors for the three optimum regional species-specific models, as measured by RMSE range from 5 to 9.2 days (Table 6.5), and the mean RMSE is 7 days.

To validate performances of the three regional models in spatial extrapolation, daily mean air temperature and daily precipitation data at the 14 external stations during 2005–2009 were substituted into regional species-specific models and the predicted green-up dates were compared with field observations. As sample sizes of

Table 6.5 Parameters and simulation accuracies of optimum regional species-specific models

Species	Number of observation	Optimum model	T_b (°C)	F^* (°C)	P^* (mm)	RMSE (days)
L. chinensis	123	$M_{t\text{-}p1}$	0.0	119.7	2.5	6.8
S. baicalensis	43	M_t	0.2	129.4	–	5.0
S. krylovii	68	$M_{t\text{-}p2}$	0.3	106.8	2.6	9.2

green-up data for *Stipa baicalensis* and *Stipa krylovii* at external stations are relatively small, the precision of the spatial validation was evaluated based on the mixed sample of green-up data for the two species at Stipa. Results show that the observed green-up dates of *Leymus chinensis* and *Stipa baicalensis*/*Stipa krylovii* correlate significantly positive with the predicted green-up dates of *Leymus chinensis* and *Stipa baicalensis*/*Stipa krylovii*, and the RMSEs are 9.8 and 10.4 days, respectively (Fig. 6.6). The RMSEs of the spatial validation are 3.0 days larger than the RMSE of the regional modeling for *Leymus chinensis*, and 3.3 days larger than the average RMSE of the regional modeling for *Stipa baicalensis* and *Stipa krylovii*, respectively (Table 6.5).

6.3.6 Spatiotemporal Patterns of Green-up Dates

For reconstructing spatial patterns of green-up dates of the three grass species across the Inner Mongolian Grassland, daily mean air temperature and daily precipitation data at 8 km × 8 km grids from 1983 to 2009 were substituted into the

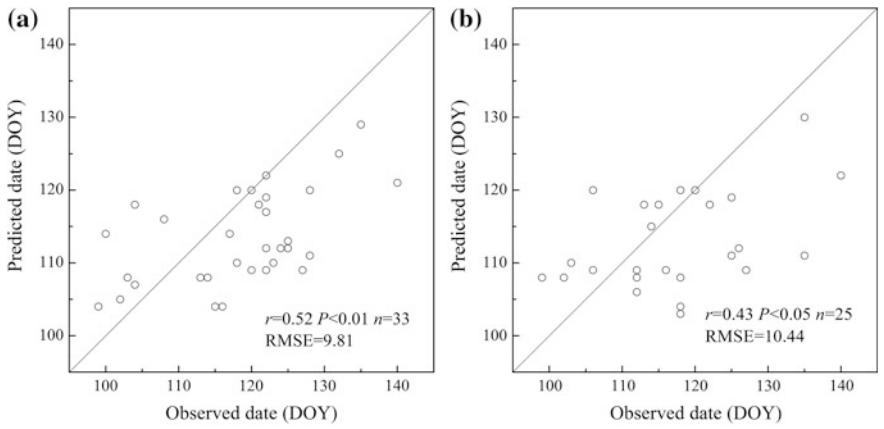

Fig. 6.6 Comparison between observed and predicted green-up dates for **a** *Leymus chinensis* and **b** *Stipa baicalensis*/*Stipa krylovii* at external stations during 2005–2009

three regional models. Because the regional models of *Stipa baicalensis* and *Stipa krylovii* were created within meadow steppe areas and typical steppe areas, respectively, time series of gridded green-up dates for *Stipa baicalensis* within meadow steppe areas and *Stipa krylovii* within typical steppe areas were reconstructed separately, and then merged together for illustrating spatial patterns of green-up dates and their linear trends during 1983–2009 for the two grass species at Stipa. Generally speaking, the spatial pattern of mean green-up dates for *Leymus chinensis* is similar to that for *Stipa baicalensis*/*Stipa krylovii*. Green-up dates represented a spatial progression from southwest and southeast to north in the southern part and from west to east in the northern part of the Inner Mongolian Grassland, which is aligned approximately along the thermal and moisture gradient. The spatial differences in mean green-up dates for *Leymus chinensis* and *Stipa baicalensis*/*Stipa krylovii* were between 91 DOY (1 April) and 142 DOY (22 May) and between 89 DOY (30 March) and 143 DOY (23 May), respectively (Fig. 6.7).

With regard to spatial patterns of green-up date linear trends, a significant advancement in *Leymus chinensis* green-up dates was detected at 71.4 % of all grids during 1983–2009, and trend values are between 2.2 and 6.0 days per decades. The largest advancing trends appear in southwestern parts of the Inner Mongolian Grassland. Nonsignificant trends are mainly located in the central and eastern parts of the Inner Mongolian Grassland (Fig. 6.8a). By contrast, a significant advancement in green-up dates of *Stipa baicalensis*/*Stipa krylovii* was only found at 40.3 % of all grids, and trend values range from 2.3 and 6.2 days per decades, which are mainly distributed in the northeastern and southwestern parts of the Inner Mongolian Grassland (Fig. 6.8b).

At regional scales, green-up dates of *Leymus chinensis*, *Stipa baicalensis* and *Stipa krylovii* have significantly advanced at rates of 2.9 days per decade across the Inner Mongolian Grassland, 3.0 days per decade in meadow steppe areas, and 2.2 days per decade in typical steppe areas over 1983–2009, respectively (Fig. 6.9).

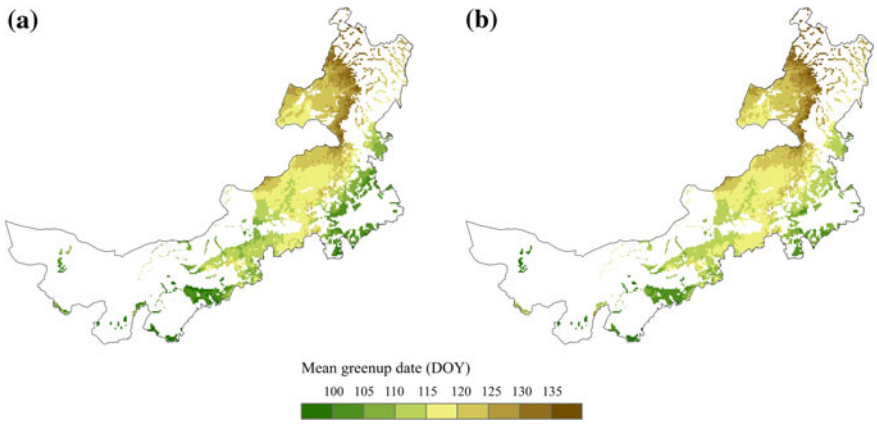

Fig. 6.7 Reconstructed spatial patterns of mean green-up dates for **a** *Leymus chinensis* and **b** *Stipa baicalensis*/*Stipa krylovii* in the Inner Mongolian Grassland during 1983–2009

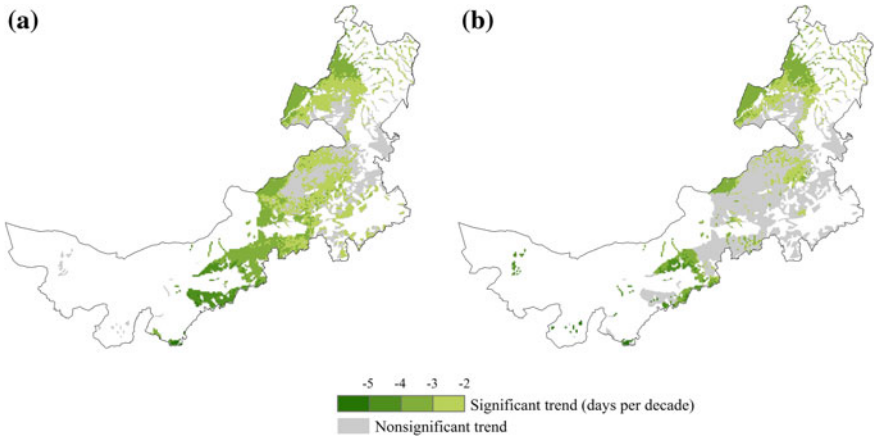

Fig. 6.8 Reconstructed spatial patterns of linear trends of green-up dates for **a** *Leymus chinensis* and **b** *Stipa baicalensis*/*Stipa krylovii* in the Inner Mongolian Grassland during 1983–2009

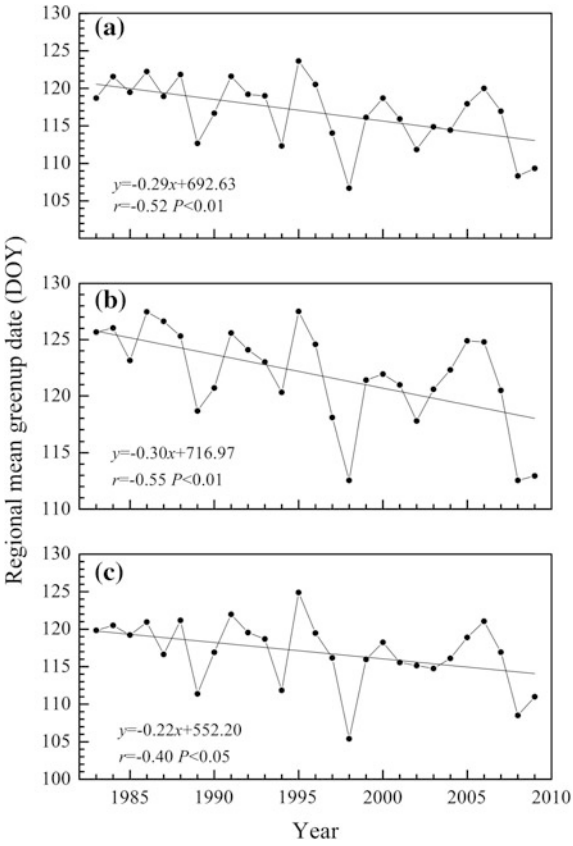

Fig. 6.9 Reconstructed linear trends of green-up dates for **a** *Leymus chinensis* over the Inner Mongolian Grassland **b** *Stipa baicalensis* in meadow steppe areas, and **c** *Stipa krylovii* in typical steppe areas during 1983–2009

References

Akaike H (1973) Information theory and an extension of the maximum likelihood principle. In: Petrov BN, Csaki F (eds) Proceedings of the second international symposium on information theory. Akademiai Kiado, Budapest, pp 267–281

Cannell MGR, Smith RI (1983) Thermal time, chill days and prediction of budburst in *Picea sitchensis*. J Appl Ecol 20:951–963

Chen XQ (2009) Phenological obseration in China. In: Hudson IL, Keatley MR (eds) Phenological research: Methods for environmental and climate change analysis. Springer, Dordrecht, pp 35–38

Chen XQ, Zhou M, Zheng T, Zhang RJ (2008) Examining seasonal variations of *Leymus chinensis* photosynthetic rates in the Hulunbeier Grassland: a case study of a grassland meteorological experiment station in Ewenke (in Chinese with English Abstract). Acta Ecol Sinica 28:2003–2012

Chen XQ, Li J, Xu L, Liu L, Ding D (2014) Modeling greenup date of dominant grass species in the Inner Mongolian Grassland using air temperature and precipitation data. Int J Biometeorol 58:463–471

China Meteorological Administration (1978) Atlas of the climate of China (in Chinese). Sinomaps Press, Beijing

China Meteorological Administration (1993) Observation criterion of agricultural meteorology (in Chinese). China Meteorological Press, Beijing

Chuine I (2000) A unified model for budburst of trees. J Theoret Biol 207:337–347

Chuine I, Cour P, Rousseau DD (1998) Fitting models predicting dates of flowering of temperate-zone trees using simulated annealing. Plant, Cell Environ 21:455–466

Chuine I, Cour P, Rousseau DD (1999) Selecting models to predict the timing of flowering of temperate trees: implications for tree phenology modelling. Plant, Cell Environ 22:1–13

Chuine I, Cambon G, Comtois P (2000) Scaling phenology from the local to the regional level: advances from species-specific phenological models. Global Change Biol 6:943–952

Chuine I, Kramer K, Hänninen H (2003) Plant development models. In: Schwartz MD (ed) Phenology: An integrative environmental science. Kluwer Academic Publishers, Dordrecht, pp 217–235

Cleland EE, Chiariello NR, Loarie SR, Mooney HA, Field CB (2006) Diverse responses of phenology to global changes in a grassland ecosystem. Proc Natl Acad Sci USA 103:13740–13744

Crimmins TM, Crimmins MA, Bertelsen CD (2010) Complex responses to climate drivers in onset of spring flowering across a semi-arid elevation gradient. J Ecol 98:1042–1051

Crimmins TM, Crimmins MA, Bertelsen CD (2011) Onset of summer flowering in a 'SkyIsland' is driven by monsoon moisture. New Phytol 191:468–479

Delpierre N, Dufrêne E, Soudani K, Ulrich E, Cecchini S, Boé J, François C (2009) Modelling interannual and spatial variability of leaf senescence for three deciduous tree species in France. Agric For Meteorol 149:938–948

Editorial Board of the Inner Mongolian Grassland (1991) The Inner Mongolian Grassland (in Chinese). Renmin Press of Inner Mongolia, Huhehot

Fu YH, Campioli M, Van Oijen M, Deckmyn G, Janssens IA (2012) Bayesian comparison of six different temperature-based budburst models for four temperate tree species. Ecol Modelling 230:92–100

García-Mozo H, Chuine I, Aira MJ, Belmonte J, Bermejo D, Díaz de la Guardia C, Elvira B, Gutiérrez M, Rodríguez-Rajo J, Ruiz L, Trigo MM, Tormo R, Valencia R, Galán C (2008) Regional phenological models for forecasting the start and peak of the *Quercus* pollen season in Spain. Agric For Meteorol 148:372–380

Hall DO, Scurlock JMO, Ojima DS, Parton WJ, Wigley TML, Schimel D (2000) Grasslands and the global carbon cycle: modeling the effects of climate change. In: Wigley TML, Schimel DS (eds) The carbon cycle. Cambridge University Press, Cambridge, pp 102–114

Hänninen H (1990) Modelling bud dormancy release in trees from cool and temperate regions. Acta For Fenn 213:1–47

Hunter AF, Lechowicz MJ (1992) Predicting the timing of budburst in temperate trees. J Appl Ecol 29:597–604

Hutchinson MF (2002) Anusplin Version 4.2 User Guide. Centre for Resource and environmental studies. The Australian National University, Canberra

Jentsch A, Kreyling J, Boettcher-Treschkow J, Beierkuhnlein C (2009) Beyond gradual warming: extreme weather events alter flower phenology of European grassland and heath species. Global Change Biol 15:837–849

Kramer K (1994a) A modeling analysis of the effects of climatic warming on the probability of spring frost damage to tree species in the Netherlands and Germany. Plant, Cell Environ 17:367–377

Kramer K (1994b) Selecting a model to predict the onset of growth of *Fagus sylvatica*. J Appl Ecol 31:172–181

Landsberg JJ (1974) Apple fruit bud development and growth; analysis and an empirical model. Ann Bot 38:1013–1023

Lesica P, Kittelson PM (2010) Precipitation and temperature are associated with advanced flowering phenology in a semi-arid grassland. J Arid Environ 74:1013–1017

Linkosalo T, Lappalainen HK, Hari P (2008) A comparison of phenological models of leaf bud burst and flowering of boreal trees using independent observations. Tree Physiol 28:1873–1882

Morin X, Lechowicz MJ, Augspurger C, O'Keefe J, Viner D, Chuine I (2009) Leaf phenology in 22 North American tree species during the 21st century. Global Change Biol 15:961–975

Murray MB, Cannell MGR, Smith RI (1989) Date of budburst of fifteen tree species in Britain following climatic warming. J Appl Ecol 26:693–700

Nash JE, Sutcliffe JV (1970) River flow forecasting through conceptual models part I—a discussion of principles. J Hydrol 10:282–290

Sherry RA, Zhou XH, Gu SL, Arnone JA, Schimel DS, Verburg PS, Wallace LL, Luo YQ (2007) Divergence of reproductive phenology under climate warming. Proc Natl Acad Sci USA 104:198–202

Shinoda M, Ito S, Nachinshonhor GU, Erdenetsetseg D (2007) Phenology of Mongolian grasslands and moisture conditions. J Meteorol Soc Jap 85:359–367

Study Group of Animal Husbandry Climate Regionalization for China's Pastoral Areas (1988) Animal husbandry climate for China's pastoral areas (in Chinese). China Meteorological Press, Beijing

Xu L, Chen XQ (2013) Regional unified model-based leaf unfolding prediction from 1960 to 2009 across northern China. Global Change Biol 19:1275–1284

Chapter 7
Spatial and Temporal Validation of Remote Sensing Phenology

Abstract To validate remote sensing vegetation phenology in the deciduous broadleaf forest of northern China, monthly and daily mean air temperature-based spatial phenology models were employed to establish yearly gridded spatial datasets of first leaf unfolding (beginning of the growing season, BGS) and leaf fall end (end of the growing season, EGS) dates of dominant tree species at spatial scales commensurate with satellite data. Two separate approaches were conducted for validating satellite-derived growing season parameters by means of ground-based growing season parameters (BGS and EGS). First, a spatial validation of the satellite-derived BGS and EGS retrieved from Normalized Difference Vegetation Index (NDVI) data of Moderate Resolution Imaging Spectroradiometer (MODIS) was implemented in northeastern China from 2001 to 2005. Results show that satellite-derived BGS might be a better indicator than EGS in monitoring spatial variation of ground-based growing season parameters, whereas satellite-derived EGS might be a better indicator than BGS in measuring occurrence time of ground-based growing season parameters. Then, spatial, temporal and spatiotemporal validations of the satellite-derived start of season (SOS) generated from NDVI data of Advanced Very High Resolution Radiometer (AVHRR) were carried out in northern China during 1986–2006. Results indicate that the yearly spatial series of SOS correlates significantly positive ($P < 0.001$) with the yearly spatial series of BGS over all pixels, while the time series of SOS correlates significantly positively ($P < 0.05$) with the time series of BGS at 65.8 % of all pixels during 1986–2006. Moreover, the spatiotemporal series of SOS correlate also significantly positive ($P < 0.001$) with the spatiotemporal series of BGS. The spatial, temporal and spatiotemporal differences between SOS and BGS are all at acceptable levels overall. Thus, the satellite-derived start of season can effectively monitor spatial, temporal and spatiotemporal variations of the ground-based growing season beginning.

Keywords First leaf unfolding · Leaf fall end · Normalized difference vegetation index · Growing season · Spatial and temporal correlation · Error estimate

X. Chen, *Spatiotemporal Processes of Plant Phenology*,
SpringerBriefs in Geography, DOI 10.1007/978-3-662-49839-2_7

7.1 Introduction

A true growing season may be defined as the number of days in a year in which a plant can grow (Wang 1963). In practice, the vegetation growing season is determined by plant budburst or leaf unfolding date in spring (beginning of the growing season, BGS) and leaf coloration or leaf fall date in autumn (end of the growing season, EGS) (Chen 1994; Chmielewski and Rötzer 2001; Matsumoto et al. 2003; Menzel 2003; Chen and Xu 2012). Because the vegetation growing season shifts influenced by climate change control seasonal CO_2, water, and energy exchanges between vegetation and low atmosphere and their feedbacks to regional and global climate change (Churkina et al. 2005; Barr et al. 2009; Migliavacca et al. 2012; Richardson et al. 2012), detecting the vegetation growing season and its spatiotemporal variations is crucial for revealing two-way feedback mechanisms among climate change, vegetation dynamics and biogeochemical cycles. There are mainly two types of data sources for identifying the vegetation growing season. The ground visually observed phenological data are usually applied to determine the growing season of individual plants and plant communities at local scales, while satellite remote sensing data are mainly used to estimate the land surface growing season at regional and global scales (Reed et al. 1994; Zhou et al. 2001; Zhang et al. 2003; Jeong et al. 2011). Due to spatial scale and temporal resolution differences, remotely sensed vegetation indices may not directly reflect ground-based phenological stages, such as leaf unfolding and leaf fall (Reed et al. 1994). Thus, a spatial and temporal comparison of these coarse resolution satellite measures with point-based field phenological events is necessary (Schwartz 1998; Chen et al. 2000, 2013; Fisher et al. 2006; Luo et al. 2013). However, this kind of surface validation of remote sensing phenology was commonly restricted by a lack of in situ phenological data at spatial scales commensurate with satellite data (Fisher et al. 2006; Liang et al. 2011; Zhang and Goldberg 2011; Chen et al. 2013; Luo et al. 2013). Reliable validation is possible by up-scaling intensive field phenology measurements to pixel scales (Liang et al. 2011). In this chapter, monthly and daily mean air temperatures-based spatial phenology models were employed to build gridded spatial datasets of first leaf unfolding date and leaf fall end date of indicator tree species for validating the remotely sensed BGS and EGS.

7.2 Spatial Validation of Satellite-Derived Phenology in Northeastern China's Deciduous Broadleaf Forest

7.2.1 Study Area and Indicator Tree Species

The deciduous broadleaf forest is a dominant forest vegetation type in northern China's temperate zone, which is mainly distributed in mountainous areas, including middle part of the Da Hinggan Ling mountains, southeast part of the Xiao

Hinggan Ling mountains, the Changbai Shan mountains, the Yan Shan mountains, and the Qin Ling mountains from north to south (Fig. 7.1). The plant community is consisted of broadleaf trees and shrubs, such as *Quercus*, *Betula*, *Carpinus*, *Ulmus*, *Celtis*, *Acer*, *Populus*, *Malus*, etc. (Compilation Committee of the Vegetation of China 1980). Because *Ulmus pumila* is one of the major deciduous trees that grow widely on plains, hills, low mountains, and sand hills, it can serve as an indicator species (Chen and Xu 2012) for spatial validation of satellite-derived vegetation phenology. The *Ulmus pumila* growing season was defined as the period between first leaf unfolding date and leaf fall end date. First leaf unfolding was identified as when a few leaves are fully open in spring, whereas leaf fall end was identified as when almost all leaves have fallen to the ground during late autumn or early winter.

7.2.2 Materials and Methods

Using *Ulmus pumila* first leaf unfolding and leaf fall end data and air temperature data collected at 46 stations in China's temperate zone during 1986–2005, monthly mean air temperature-based spatial phenology models were created for each year (Xu and Chen 2012). These models can be employed to calculate yearly spatial patterns of *Ulmus pumila* growing season beginning and end dates on the basis of

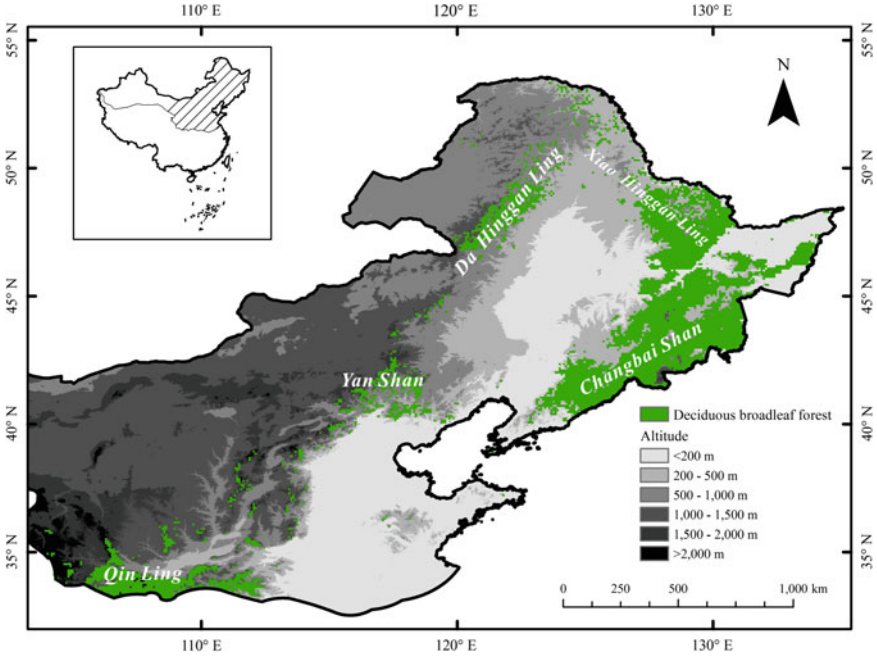

Fig. 7.1 Distribution of the deciduous broadleaf forest in northeastern China [Reprinted from Chen et al. (2013), with permission from Taylor & Francis]

yearly spatial patterns of February–April and September–November mean temperatures in the deciduous broadleaf forest areas. To achieve this goal, monthly mean air temperature data at 343 stations in China's temperate zone from 2001 to 2005 were interpolated into gridded monthly mean air temperature data using the climate data interpolation package ANUSPLIN 4.2 (Hutchinson 2002) and Digital Elevation Model data derived from the US Geological Survey with a grid size of 8 km. Then, yearly February–April and September–November mean temperatures during 2001–2005 at all 8 km × 8 km grids within the deciduous broadleaf forest areas were substituted into the corresponding yearly spring and autumn spatial phenology models, and yearly gridded ground-based growing season beginning (BGS_{gb}) and end (EGS_{gb}) dates were calculated.

The MODIS-NDVI data were acquired from the dataset MOD13A2 with a spatial resolution of 1 km and temporal interval of 16 days during 2001 and 2005 (http://reverb.echo.nasa.gov/reverb/). A typical NDVI curve can be divided into four phenological phases, namely, green-up, maturity, senescence, and dormancy (Zhang et al. 2003). Here, green-up and dormancy dates were defined as beginning (BGS_{sat}) and end (EGS_{sat}) dates of the satellite-derived growing season. As the NDVI data have to be time-stamped on a particular day-of-year (DOY) for curve fitting, the center DOY in each 16-day window was used to represent the particular day-of-year. Then, the logistic model was employed to simulate the discrete NDVI values on these particular days-of-year, and the transition dates of BGS_{sat} and EGS_{sat} were determine by calculating turning points with maximum change rates of curvature on the logistic curve (Zhang et al. 2003).

Because the spatial resolutions are different between satellite-derived growing season parameters (1 km × 1 km) and ground-based growing season parameters (8 km × 8 km), mean dates of BGS_{sat} and EGS_{sat} at all 1 km × 1 km pixels within an 8 km × 8 km grid were calculated as the corresponding BGS_{sat} and EGS_{sat} dates at the 8 km × 8 km grid. Thus, the spatially commensurate BGS_{sat}/EGS_{sat} and BGS_{gb}/EGS_{gb} datasets were obtained.

7.2.3 *Spatial Pattern Comparison of Satellite-Derived and Ground-Based Growing Seasons*

With respect to geographical distributions of satellite-derived and ground-based growing season parameters, spatial patterns of *Ulmus pumila* growing season beginning and end dates are similar to those of satellite-derived growing season beginning and end dates, respectively. Generally speaking, the beginning dates of both growing seasons displayed a spatial progression from south to north and from east to west during 2001–2005. Namely, the growing season started first in the Qin Ling mountains, then in the Yan Shan mountains and the Changbai Shan mountains, and at last in the Xiao Hinggan Ling mountains and the Da Hinggan Ling mountains. On average, the satellite-derived growing season beginning dates appeared between the first ten-day period of March in south and the first ten-day

period of June in north, whereas the *Ulmus pumila* growing season beginning dates occurred between the last ten-day period of March in south and the mid-month of June in north (Fig. 7.2a, b). By contrast, the end dates of both growing seasons showed a spatial progression from north to south and from west to east. That is, the growing season terminated first in the Da Hinggan Ling mountains and the Xiao Hinggan Ling mountains, then in the Changbai Shan mountains and the Yan Shan mountains, and at last in the Qin Ling mountains. On average, the satellite-derived growing season end dates appeared between the mid-month of September in north and the mid-month of December in south, while the *Ulmus pumila* growing season end dates occurred between the last ten-day period of September in north and the last ten-day period of November in south (Fig. 7.2c, d).

Across the deciduous broadleaf forest areas, regional mean BGS_{sat} was obviously earlier than regional mean BGS_{gb} during 2001–2005. The difference ranged from 8 days (in 2005) to 18 days (in 2002). In contrast, regional mean EGS_{sat} was slightly later than regional mean EGS_{gb} during 2001–2005 and the difference was between 1 day (in 2004) and 6 days (in 2005). Therefore, the mean satellite-derived growing season duration was longer than the mean ground-based growing season

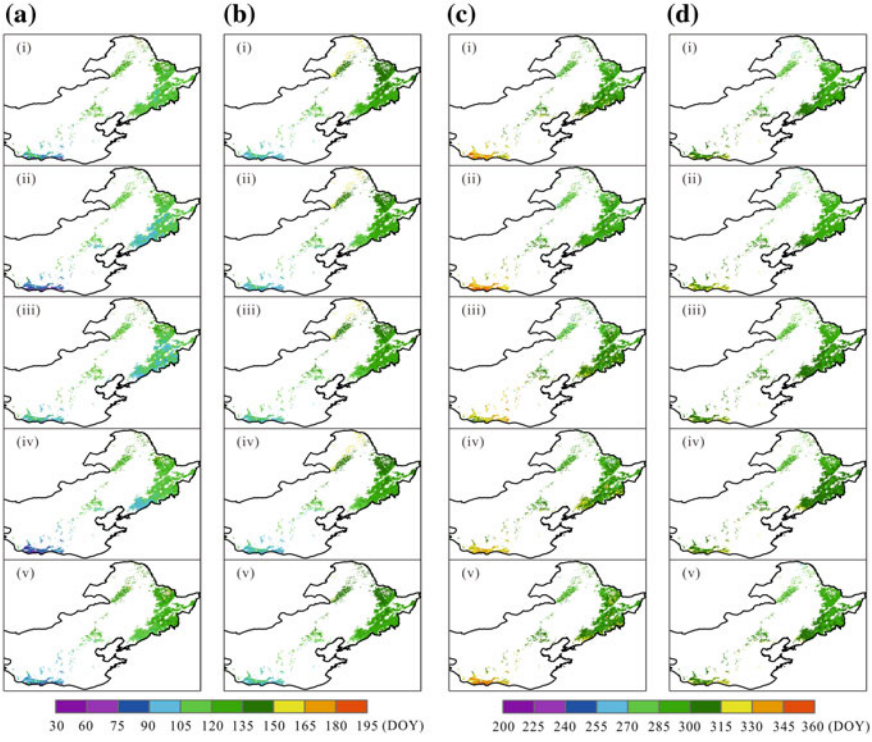

Fig. 7.2 Spatial patterns of satellite-derived and ground-based growing season beginning and end dates. **a** BGS_{sat}; **b** BGS_{gb}; **c** EGS_{sat}; **d** EGS_{gb}; *i* 2001; *ii* 2002; *iii* 2003; *iv* 2004; *v* 2005 [Reprinted from Chen et al. (2013), with permission from Taylor & Francis]

duration. Moreover, the spatial standard deviation of BGS_{sat} was larger than that of BGS_{gb} in three of five years, whereas the spatial standard deviation of EGS_{sat} was larger than that of EGS_{gb} in all five years (Table 7.1). Namely, satellite-derived growing season parameters have a larger spatial heterogeneity than ground-based growing season parameters.

7.2.4 Spatial Relationship Between Satellite-Derived and Ground-Based Growing Seasons

In order to precisely assess the spatial consistency between satellite-derived and ground-based growing season parameters, a correlation and regression analysis was implemented between spatial series of BGS_{sat} and BGS_{gb} and between spatial series of EGS_{sat} and EGS_{gb} across the study areas year-by-year. BGS_{sat} correlates positively with BGS_{gb} over all pixels during 2001–2005 ($p < 0.001$), namely, the earlier the BGS_{gb} at a pixel in a year, the earlier the BGS_{sat} at the pixel in the year. The explained variances (R^2) of yearly spatial regression equations between BGS_{sat} and BGS_{gb} range from 22 to 62 %, and the Root Mean Square Errors (RMSEs) of yearly BGS_{sat} simulations range from 9.4 to 11.7 days. Slopes of yearly spatial regression equations indicate that a spatial shift (advance or delay) in BGS_{gb} by 1 day corresponds to a spatial shift (advance or delay) in BGS_{sat} between 0.49 and 0.99 days (Fig. 7.3a). Similarly, EGS_{sat} correlates also positively with EGS_{gb} over all pixels during 2001–2005 ($p < 0.001$). That is, the earlier the EGS_{gb} at a pixel in a year, the earlier the EGS_{sat} at the pixel in the year. The explained variances (R^2) of yearly spatial regression equations between EGS_{sat} and EGS_{gb} range from 29 to 54 %, and the RMSEs of yearly EGS_{sat} simulations range from 12.6 to 12.9 days. On average, a spatial shift (advance or delay) in EGS_{gb} by 1 day corresponds to a spatial shift (advance or delay) in EGS_{sat} between 0.85 and 1.21 days (Fig. 7.3b).

Table 7.1 Regional mean value (RM, DOY) and spatial standard deviation[a] (SSD in days) of satellite-derived and ground-based growing season beginning and end dates from 2001 to 2005 (Chen et al. 2013)

Year	BGS_{sat}		BGS_{gb}		EGS_{sat}		EGS_{gb}	
	RM	SSD	RM	SSD	RM	SSD	RM	SSD
2001	116	13.1	129	14.5	301	16.2	297	10.1
2002	107	13.2	125	14.7	297	18.5	295	11.2
2003	111	13.2	127	12.6	303	16.4	300	9.1
2004	112	16.0	127	14.9	304	15.1	303	8.5
2005	119	15.3	127	12.2	305	15.6	299	10.3

[a]Spatial standard deviation (SSD) measures variation of a spatial variable (such as BGS_{sat} at all pixels in the study areas in a year) using the formula: $SSD = \sqrt{\sum_{i=1}^{n} (X_i - \bar{X})^2 / n}$, where X_i denotes the value of the spatial variable at pixel i; $\bar{X}$ denotes the regional mean value of the spatial variable at all pixels; n is the total number of pixels in the study areas

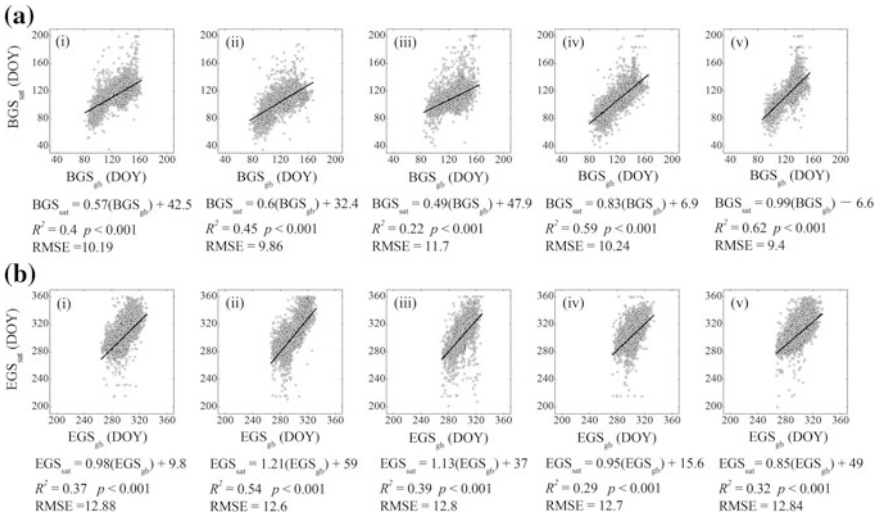

Fig. 7.3 Spatial correlation and regression analysis **a** between BGS_{sat} and BGS_{gb} and **b** between EGS_{sat} and EGS_{gb} over all pixels. *i* 2001; *ii* 2002; *iii* 2003; *iv* 2004; *v* 2005. R^2 denotes the coefficient of determination [Reprinted from Chen et al. (2013), with permission from Taylor & Francis]

It is noteworthy that the explained variances of spatial BGS models are larger than those of spatial EGS models in three of five years, whereas the RMSEs of BGS_{sat} simulations are smaller than those of EGS_{sat} simulations in all five years. Therefore, the spatial consistency between BGS_{sat} and BGS_{gb} is better than that between EGS_{sat} and EGS_{gb}. However, because the slopes of the regression equations between EGS_{sat} and EGS_{gb} are close to 1 in all five years but the slopes of the regression equations between BGS_{sat} and BGS_{gb} are much smaller than 1 in three of five years, the spatial synchronism between EGS_{sat} and EGS_{gb} is better than that between BGS_{sat} and BGS_{gb}.

7.3 Spatial and Temporal Validation of Satellite-Derived Phenology in Northern China's Deciduous Broadleaf Forest

7.3.1 Study Area and Indicator Tree Species

In this section, the temperate deciduous broadleaf forest areas across all of northern China (Fig. 7.4) were selected to analyze the spatial and temporal relationships between ground-based beginning date of the growing season (BGS) and remotely sensed starting date of season (SOS). The BGS was defined as the mean first leaf unfolding date of *Ulmus pumila*, *Salix matsudana*, *Populus simonii* and *Prunus*

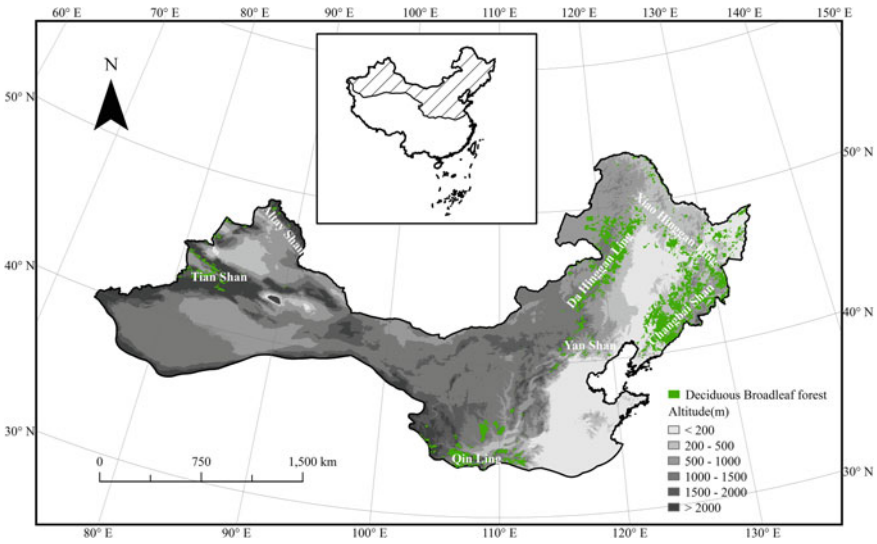

Fig. 7.4 Distribution of the temperate deciduous broadleaf forest areas in northern China

armeniaca. Because these trees are all native species and grow widely in temperate northern China, they can serve as representative tree species of local plant community.

7.3.2 Materials and Methods

The first leaf unfolding dates of the four tree species during 1986–2006 were used as the dependent variable of the daily mean air temperature-based spatial phenology model (Chap. 5). The first leaf unfolding data with a time series length of at least 10 years were obtained from 77 stations for *Salix matsudana*, 61 stations for *Populus simonii*, 72 stations for *Ulmus pumila*, and 40 stations for *Prunus armeniaca* (Fig. 7.5).

Using spatial series of first leaf unfolding dates and daily mean air temperatures within the optimum length period over corresponding stations in each year, the daily mean air temperature-based spatial leaf unfolding models were created for each tree species and in each year. Then, the species-specific daily mean air temperatures during the optimum length period at all 8 km × 8 km grids (interpolated also by the climate data interpolation package ANUSPLIN 4.2 and Digital Elevation Model data derived from the US Geological Survey, see Sect. 7.2.2) across the deciduous broadleaf forest areas in each year were substituted into the corresponding yearly spatial leaf unfolding models of the four tree species, respectively. As a result, gridded first leaf unfolding dates of the four tree species were estimated across the deciduous broadleaf forest areas in each year. Based on the gridded first leaf unfolding dates of each species in each year, the gridded mean

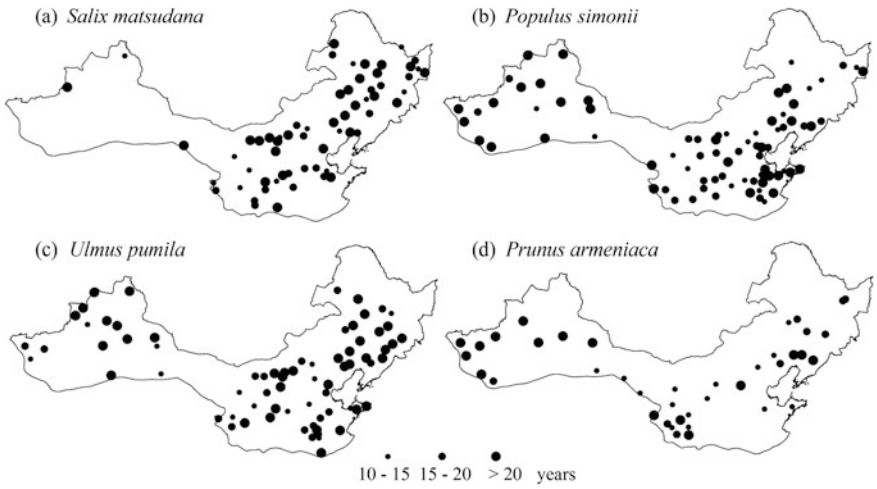

Fig. 7.5 Location of phenological stations and time series length of first leaf unfolding data for the four tree species

first leaf unfolding dates of the four tree species in each year were calculated. Thus, the spatially commensurate BGS datasets with satellite data were established.

Remotely sensed AVHRR NDVI data with the spatial resolution of 8 km and temporal interval of 15 days from 1986 to 2006 were used for retrieving SOS across the deciduous broadleaf forest areas. The computation process was implemented through following steps. First, the Savitzky–Golay filter was employed to smooth the original NDVI time series so that abnormal high and low values could be eliminated (Chen et al. 2004). Then, the midpoint model (White et al. 1997) was applied to extract the satellite-derived SOS at each pixel and in each year.

7.3.3 Spatial Relationship Between Satellite-Derived SOS and Ground-Based BGS

Similar to the results in Sect. 7.2.3, the mean BGS and SOS dates displayed a consistent spatial progression from south (earlier) to north (later) and from east (earlier) to west (later) in the eastern part of northern China during 1986–2006. The spatial differences in mean BGS and SOS dates ranged from 90 DOY (the end of March) to 170 DOY (early June) (Fig. 7.6).

With regard to spatial variation consistency between satellite-derived SOS and ground-based BGS at the pixel level, a significantly positive correlation ($P < 0.001$) was detected in each year (Table 7.2). This indicates that the earlier the SOS date at a pixel in a year, the earlier the BGS date at the pixel in the year across the deciduous broadleaf forest areas.

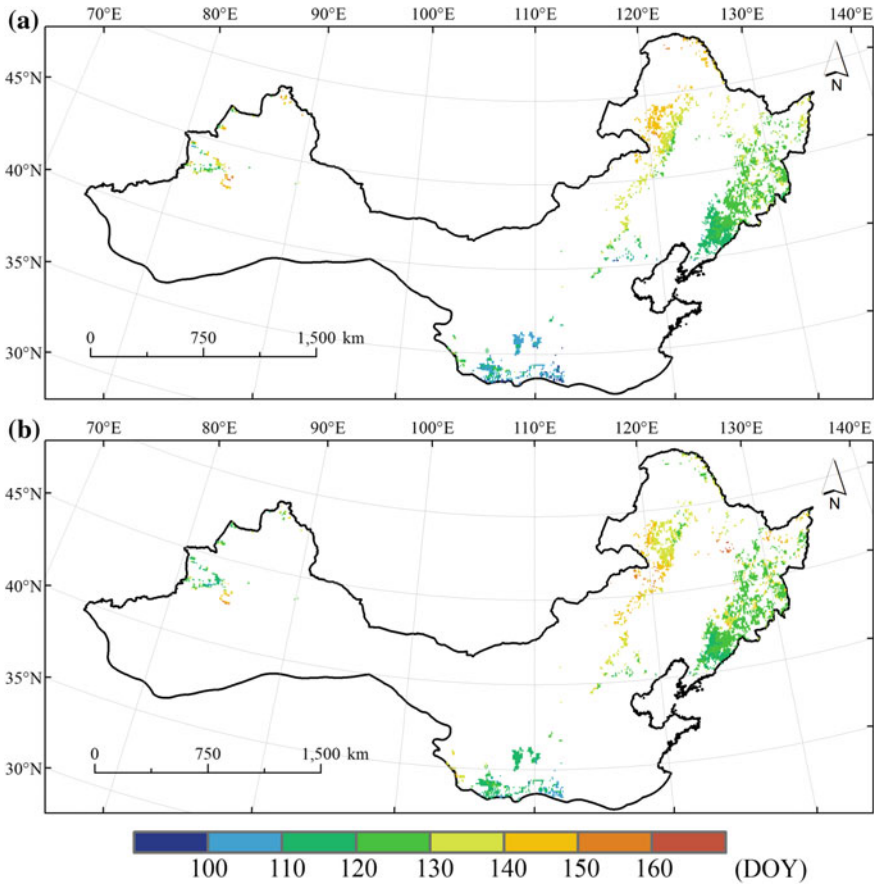

Fig. 7.6 Spatial patterns of mean BGS (growing season beginning) and SOS (start of season) over 1986–2006 in the deciduous broadleaf forest of northern China. **a** BGS; **b** SOS

The yearly mean errors between satellite-derived SOS and ground-based BGS at all pixels range from −2.8 days (1998) to 6.1 days (1990), while the yearly mean absolute errors fall in between 6.6 (1988) days and 11.0 days (2004) (Table 7.2). Overall, spatial patterns of the yearly NDVI-retrieved start of season can effectively reflect spatial patterns of the yearly ground-based growing season beginning across the deciduous broadleaf forest areas.

7.3.4 Temporal and Spatiotemporal Relationship Between Satellite-Derived SOS and Ground-Based BGS

To examine interannual variation consistency between satellite-derived SOS and ground-based BGS at the pixel level, spatial patterns of temporal correlation

Table 7.2 Spatial correlation coefficients (r), mean errors (MEs) and mean absolute errors (MAEs) between SOS and BGS at all pixels in each year (n = 3994) (Luo et al. 2013)

Year	Between SOS and BGS		
	r	ME	MAE
1986	0.46***	1.91	8.63
1987	0.69***	2.98	8.43
1988	0.62***	2.77	6.56
1989	0.41***	5.38	10.19
1990	0.45***	6.08	9.56
1991	0.47***	1.04	7.91
1992	0.47***	−0.87	8.38
1993	0.60***	1.95	7.35
1994	0.61***	4.17	7.99
1995	0.61***	4.90	9.19
1996	0.17***	1.51	9.67
1997	0.58***	1.57	8.06
1998	0.50***	−2.76	10.17
1999	0.64***	2.14	8.68
2000	0.52***	0.25	8.31
2001	0.54***	0.19	9.87
2002	0.51***	1.97	10.44
2003	0.53***	3.14	10.55
2004	0.59***	−0.68	11.01
2005	0.72***	−1.69	7.86
2006	0.62***	1.66	9.8

***$P < 0.001$

coefficients between SOS and BGS at each pixel were established (Fig. 7.7). The results show that SOS correlates significantly positive ($P < 0.05$) with BGS at 65.8 % of all pixels during 1986–2006. The areas with nonsignificant correlation coefficients are predominantly distributed in the south part of the Da Hinggan Ling mountains (Figs. 7.4 and 7.7a). Thus, consistent interannual variation between satellite-derived start of season and ground-based beginning of the growing season were apparent in most parts of the deciduous broadleaf forest areas of northern China from 1986 to 2006.

Meanwhile, spatial patterns of mean differences between SOS and BGS time series at each pixel during 1986–2006 display that the MEs range from +10 to –10 days at 74.3 % of all pixels. Pixels with positive MEs appear mainly in the southern parts of the deciduous broadleaf forest areas, whereas pixels with negative MEs occur mostly in the northern parts. That is, satellite-derived SOS date was normally later than ground-based BGS date in southern areas but earlier in the north (Fig. 7.7b). Similarly, the MAEs are less than 10 days at 70.6 % of all pixels. The smallest MAEs were concentrated in southern part of the Changbai Shan mountains (Figs. 7.4 and 7.7c). In general, interannual variation of the NDVI-retrieved start of season can effectively capture interannual variation of the ground-based growing season beginning in the most part of the deciduous broadleaf forest areas.

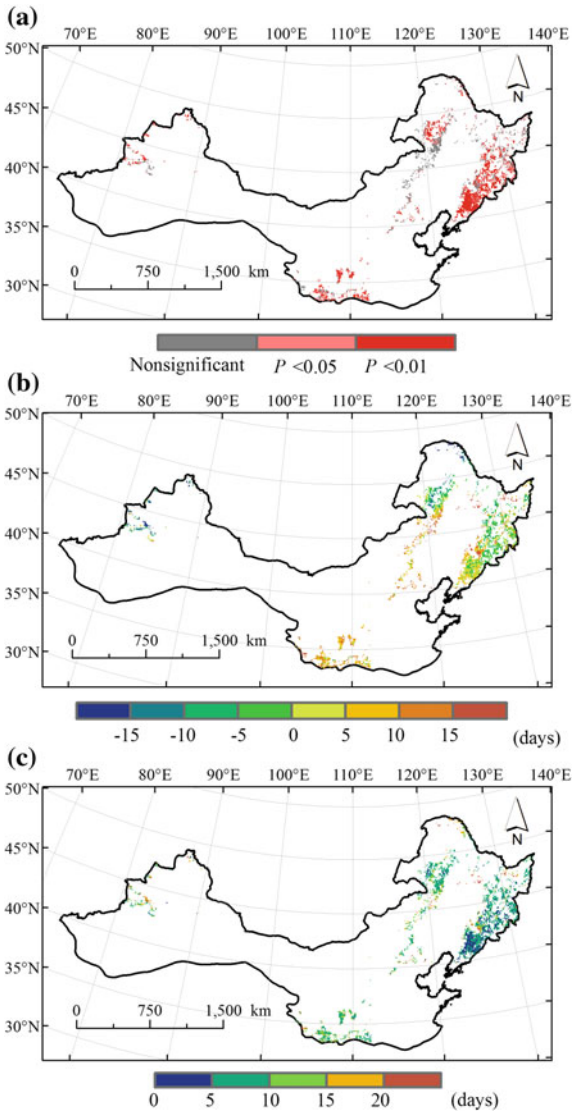

Fig. 7.7 Spatial patterns of temporal correlation coefficients and mean differences between SOS and BGS at each pixel from 1986 to 2006. **a** correlation coefficients between SOS and BGS; **b** MEs between SOS and BGS; **c** MAEs between SOS and BGS

The spatiotemporal relationship between SOS and BGS was analyzed by pooling SOS and BGS dates from all pixels and all years in the deciduous broadleaf forest areas. The results indicate that SOS correlates significantly positive ($P < 0.001$) with BGS, which implies that the earlier the BGS at a pixel in a year, the earlier the SOS at the pixel in the year. The overall average ME and MAE are 1.79 and 8.98 days, respectively (Fig. 7.8). Therefore, spatiotemporal variation of the NDVI-retrieved start of season can effectively monitor spatiotemporal variation of the ground-based growing season beginning in the deciduous broadleaf forest areas of northern China.

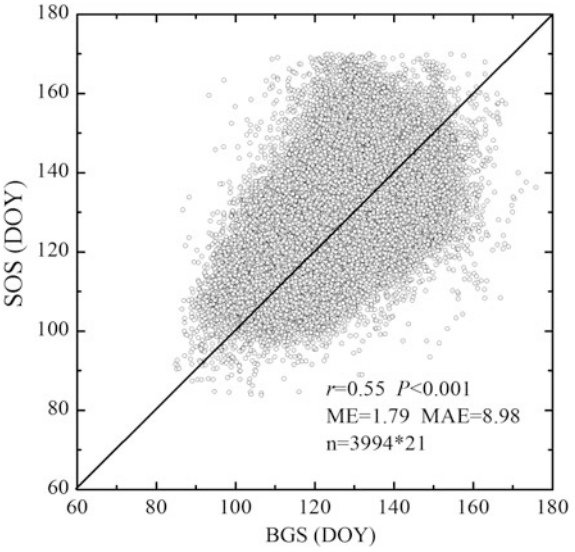

Fig. 7.8 Spatiotemporal correlation coefficients and mean differences between SOS and BGS at each pixel in each year

References

Barr A, Black TA, McCaughey H (2009) Climatic and phenological controls of the carbon and energy balances of three contrasting boreal forest ecosystems in western Canada. In: Noormets A (ed) Phenology of ecosystem processes: Applications in global change research. Springer, Dordrecht, pp 3–34

Chen XQ (1994) Untersuchung zur zeitlich-räumlichen Ähnlichkeit von phänologischen und klimatologischen Parametern in Westdeutschland und zum Einfluß geoökologischer Faktoren auf die phänologische Entwicklung im Gebiet des Taunus. Selbstverlag des Deutschen Wetterdienstes, Offenbach am Main

Chen XQ, Xu L (2012) Phenological responses of *Ulmus pumila* (Siberian Elm) to climate change in the temperate zone of China. Int J Biometeorol 56:695–706

Chen XQ, Tan ZJ, Schwartz MD, Xu CX (2000) Determining the growing season of land vegetation on the basis of plant phenology and satellite data in Northern China. Int J Biometeorol 44:97–101

Chen J, Jonsson P, Tamura M, Gu ZH, Matsushita B, Eklundh L (2004) A simple method for reconstructing a high-quality NDVI time-series data set based on the Savitzky-Golay filter. Remote Sens Environ 91:332–344

Chen XQ, Luo XZ, Xu L (2013) Comparison of spatial patterns of satellite-derived and ground-based phenology for the deciduous broadleaf forest of China. Remote Sens Lett 4:532–541

Chmielewski FM, Rötzer T (2001) Response of tree phenology to climate change across Europe. Agric For Meteorol 108:101–112

Churkina G, Schimel D, Braswell BH, Xiao X (2005) Spatial analysis of growing season length control over net ecosystem exchange. Global Change Biol 11:1777–1787

Compilation Committee of the Vegetation of China (1980) The vegetation of China (in Chinese). Science Press, Beijing

Fisher JI, Mustard JF, Vadeboncoeur MA (2006) Green leaf phenology at Landsat resolution: Scaling from the field to the satellite. Remote Sens Environ 100:265–279

Hutchinson MF (2002) Anusplin Version 4.2 User Guide. Centre for Resource and Environmental Studies, Australian National University, Canberra

Jeong S, Ho C, Gim H, Brown ME (2011) Phenology shifts at start vs. end of growing season in temperate vegetation over the Northern Hemisphere for the period 1982–2008. Global Change Biol 17:2385–2399

Liang L, Schwartz MD, Fei SL (2011) Validating satellite phenology through intensive ground observation and landscape scaling in a mixed seasonal forest. Remote Sens Environ 115:143–157

Luo XZ, Chen XQ, Xu L, Myneni R, Zhu Z (2013) Assessing performance of NDVI and NDVI3g in monitoring leaf unfolding dates of the deciduous broadleaf forest in Northern China. Remote Sens 5:845–861

Matsumoto K, Ohta T, Irasawa M, Nakamura T (2003) Climate change and extension of the Ginkgo biloba L. growing season in Japan. Global Change Biol 9:1634–1642

Menzel A (2003) Plant phenological anomalies in Germany and their relation to air temperature and NAO. Clim Change 57:243–263

Migliavacca M, Sonnentag O, Keenan T, Cescatti A, O'Keefe J, Richardson A (2012) On the uncertainty of phenological responses to climate change, and implications for a terrestrial biosphere model. Biogeosciences 9:2063–2083

Reed BC, Brown JF, Vanderzee D, Loveland TR, Merchant JW, Ohlen DO (1994) Measuring phenological variability from satellite imagery. J Veg Sci 5:703–714

Richardson AD, Anderson RS, Arain MA, Barr AG, Bohrer G, Chen G, Chen JM, Ciais P, Davis KJ, Desai AR (2012) Terrestrial biosphere models need better representation of vegetation phenology: results from the North American Carbon Program Site Synthesis. Global Change Biol 18:566–584

Schwartz MD (1998) Green-wave phenology. Nature 394:839–840

Wang JY (1963) Agricultural meteorology. Pacemaker Press, Milwaukee, p 108

White MA, Thornton PE, Running SW (1997) A continental phenology model for monitoring vegetation responses to interannual climatic variability. Global Biogeochem Cycle 11:217–234

Xu L, Chen XQ (2012) Spatial modeling of the *Ulmus pumila* growing season in China's temperate zone. Sci China Earth Sci 55:656–664

Zhang XY, Goldberg MD (2011) Monitoring fall foliage coloration dynamics using time-series satellite data. Remote Sens Environ 115:382–391

Zhang XY, Friedl MA, Schaaf CB, Strahler AH, Hodges J, Gao F, Reed BC, Huete A (2003) Monitoring vegetation phenology using MODIS. Remote Sens Environ 84:471–475

Zhou LM, Tucker CJ, Kaufmann RK, Slayback D, Shabanov NV, Myneni RB (2001) Variations in northern vegetation activity inferred from satellite data of vegetation index during 1981 to 1999. J Geophys Res 106:20069–20083

Chapter 8
Process-Based Spatiotemporal Simulation and Prediction of Remote Sensing Phenology

Abstract To predict vegetation phenology under global climate change scenarios on continuous and large geographical ranges, satellite-derived start date of season (SOS) retrieved from AVHRR third generation NDVI data from 1982 to 2006 were fitted using *UniForc* and *UniChill* models at all pixels in the deciduous broadleaf forest region of northern China. The pixel-specific optimum models were then validated using daily mean air temperature and SOS data from 2007 to 2011. Further, the pixel-specific optimum models were employed to reconstruct SOS time series from 1950 to 2005 and predict SOS time series from 2006 to 2100 across the research region based on the calibrated historical daily mean air temperature data (1950–2005) and daily mean air temperature data under scenarios of the Representative Concentration Pathway (RCP) 4.5 and 8.5 (2006–2100) from outputs of the Regional Climate Model HadGEM3-RA. Because the *UniForc* model performs better in simulation efficiency than the *UniChill* model at 96.4 % of pixels, it was determined as the optimum model at these pixels. The temporal validation of the pixel-specific *UniForc* models during 2007–2011 confirmed the feasibility of the *UniForc* model in predicting SOS date in most parts of the research region. The predicted regional mean SOS dates show a significantly advancing trend during 2006–2100 at rates of 0.65 days (under RCP 4.5) and 1.79 days (under RCP 8.5) per decade. Taking the mean SOS date during 1961–1990 as the reference value, an overall advancement of decadal mean SOS date was detected in each decade during 2006 and 2100. The advancement amplitude and the spatial standard deviation (under RCP 8.5) of decadal mean SOS dates would increase with time. At the end of 21st century, the predicted regional mean SOS date under the RCP 4.5 and RCP 8.5 scenarios would be 11.8 and 20 days earlier than the regional mean SOS date during 1961–1990, respectively. Meanwhile, the spatial patterns of spring vegetation phenology under global warming would likely turn into more uncertain than at present. Furthermore, SOS dates at each pixel show also an advancement in each decade during 2011–2100 under both RCP 4.5 and RCP 8.5 scenarios. The advancement amplitude of decadal mean SOS dates under the RCP 8.5 scenario would be larger in southern parts of the deciduous broadleaf forest region than in northern parts. Thus, an enhanced sensitivity of spring phenology response to air temperature would be expected under future climate

X. Chen, *Spatiotemporal Processes of Plant Phenology*,
SpringerBriefs in Geography, DOI 10.1007/978-3-662-49839-2_8

warming, especially in colder areas or higher latitudes where the greatest climate warming is predicted.

Keywords Process-based phenology model · Satellite-derived start date of season · Regional climate model · Climate change scenarios · Spatiotemporal prediction

8.1 Introduction

As stated in Chap. 6, process-based phenology models have been usually created for fitting and predicting ground observed spring phenology of individual trees at individual locations. Air temperature is considered as the primary climate driver of spring tree phenology. Because the existing process-based phenology models are species-specific and location-dependent, they can not meet the urgent needs for predicting vegetation phenology under global climate change scenarios on continuous and large geographical ranges. To achieve this goal, developing satellite data-based spring phenology models might be an appropriate option. In this chapter, satellite-derived start date of season (SOS) retrieved from AVHRR third generation NDVI ($NDVI_{3g}$) data during 1982–2006 were fitted using *UniForc* and *UniChill* models (Chuine 2000) at all pixels in the deciduous broadleaf forest region of northern China (Fig. 7.4 in Sect. 7.3.1). The pixel-specific optimum models were then validated using air temperature and SOS data from 2007 to 2011. Further, a spatiotemporal prediction of SOS date were implemented based on the pixel-specific optimum models and the calibrated daily mean air temperature data from outputs of the Regional Climate Model HadGEM3-RA over 1950–2100 (Luo et al. 2014).

8.2 Materials and Methods

The resampled $NDVI_{3g}$ data with the spatial resolution of 8 km and temporal interval of 15 days from 1982 to 2011 were used for extracting SOS date at each pixel across the deciduous broadleaf forest region. The computation process was implemented through the same steps in Sect. 7.3.2.

For fitting process-based phenology models using satellite-derived SOS data and air temperature data at each 8 km × 8 km pixel in the deciduous broadleaf forest region of northern China, daily mean air temperature data at 343 meteorological stations in the northern China's temperate zone over the 1981–2011 period were interpolated into 8 km × 8 km grids using the climate data interpolation package

ANUSPLIN 4.2 (Hutchinson 2002) and Digital Elevation Model (DEM) data derived from the United States Geological Survey. Furthermore, the daily mean air temperature data acquired from outputs of the Regional Climate Model HadGEM3-RA under the project Coordinated Regional Downscaling Experiment (CORDEX)-EAST ASIA (Giorgi et al. 2009) over 1950–2100 were selected as input data of the pixel-specific optimum phenology models for predicting SOS date. The prediction was divided into two parts, namely, the historical reconstruction from 1950 to 2005 and the future estimation from 2006 to 2100 under global climate change scenarios. Two scenarios were chosen for assessing impacts of global warming on SOS date. The Representative Concentration Pathway (RCP) 4.5 was defined as a stabilization scenario, in which total radiative forcing is stabilized before 2100 (Thomson et al. 2011), while the RCP 8.5 scenario is characterized by increasing greenhouse gas emissions over time, which denotes the scenario with the highest greenhouse gas concentration level (Riahi et al. 2011). Because the grids of the daily mean air temperature data acquired from outputs of the Regional Climate Model HadGEM3-RA (0.44° × 0.44°) are much larger than the pixel size of SOS data (8 km × 8 km), the daily mean air temperature data were downscaled into 8 km × 8 km resolution by means of an elevation adjustment approach (Eq. 8.1). The formula is as follows:

$$X_t = -0.64 \times \frac{X_h - Y_h}{100} + Y_t \tag{8.1}$$

where X_t and Y_t denote the daily mean air temperature at 8 km grid and 0.44° grid, respectively; X_h and Y_h denote the average elevation at 8 km grid and 0.44° grid, respectively. The normal lapse rate of air temperature was set to −0.64 °C/100 m.

It is noteworthy that the two types of temperature datasets are different, and thus it is not reasonable to make direct prediction using a temperature dataset differing from the one used for model generation until both temperature datasets are calibrated (Luo et al. 2014). Therefore, historical daily mean air temperatures (1950–2005) and daily mean air temperatures under RCP 4.5 and RCP 8.5 scenarios (2006–2100) from the HadGEM3-RA outputs at each grid were further calibrated based on the mean bias values between monthly mean air temperatures downscaled from HadGEM3-RA outputs (8 km × 8 km) and monthly mean air temperatures interpolated from meteorological stations (8 km × 8 km) during 1961–1990.

The *UniForc* and *UniChill* models' structures as well as their parameterization and evaluation methods can be found in Sect. 6.2.3 of this book. Model validation (2007–2011) and prediction (1950–2100) were carried out by substituting the interpolated daily mean air temperatures from meteorological stations and calibrated daily mean air temperatures from outputs of the Regional Climate Model HadGEM3-RA into the pixel-specific optimum models, respectively (Luo et al. 2014).

8.3 Simulation and Validation of Phenology Models

Fitting root mean square errors (RMSE, Eq. 6.5) of the *UniForc* and *UniChill* models are very similar (ranging from 2.2 to 14.7 days and from 2.2 to 11.8 days, respectively), which are generally larger in southern parts of the deciduous broadleaf forest region than in northern parts (Fig. 8.1a, b). The positive Nash-Sutcliffe Efficiencies (NSE, Eq. 6.7) at more than 97 % of pixels (Fig. 8.1c, d) indicate that both *UniForc* and *UniChill* models can effectively simulate SOS date at almost all pixels.

Comparing the Akaike Information Criterion values (AIC, Eq. 6.6) of the *UniForc* and *UniChill* models at each pixel during 1982–2006, the *UniForc* model performs better in simulation efficiency (lower AIC value) than the *UniChill* model at 96.4 % of pixels, which implies that forcing temperature predominantly influence SOS date in most parts of the research region. Therefore, the *UniForc* model was determined as the optimum model at these pixels. The similar model form of the

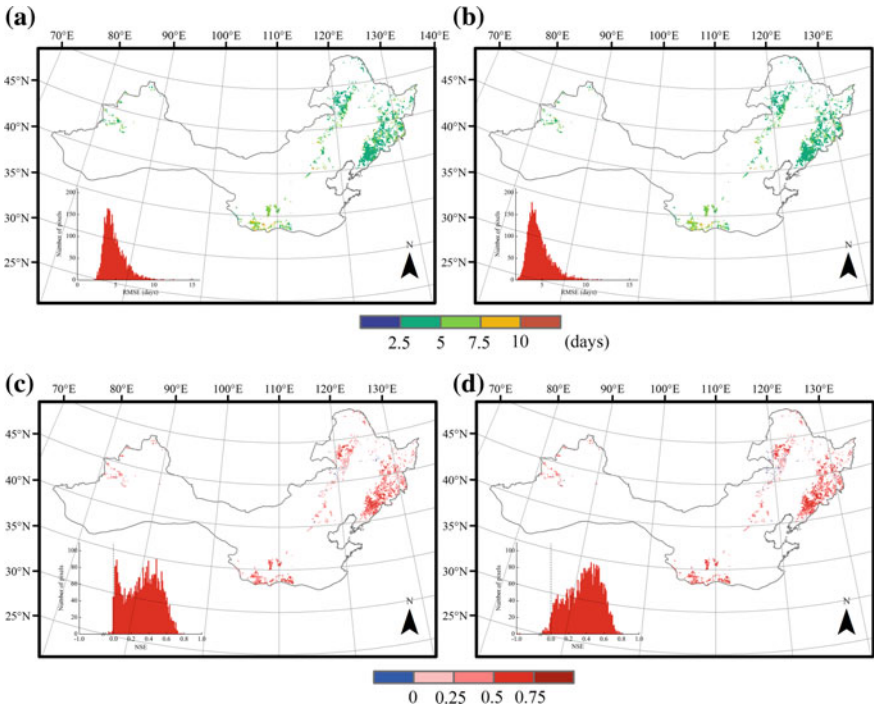

Fig. 8.1 Spatial patterns of simulation error (RMSE) and simulation effectiveness (NSE) of the models. **a** RMSE of the *UniForc* model; **b** RMSE of the *UniChill* model; **c** NSE of the *UniForc* model; **d** NSE of the *UniChill* model [Reprinted from Luo et al. (2014), with permission from Elsevier]

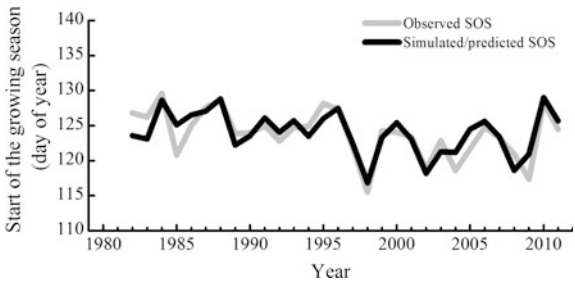

Fig. 8.2 Comparison between regional mean observed growing season start date and regional mean simulated/predicted growing season start date by the *UniForc* model over 1982–2011 [Reprinted from Luo et al. (2014), with permission from Elsevier]

SOS model and the leaf unfolding model (Xu and Chen 2013) in northern China indicate that spring remotely sensed vegetation phenology derived by the $NDVI_{3g}$ data can capture the ground signal of spring tree phenology to some extent.

Temporal extrapolation of the pixel-specific *UniForc* models during 2007–2011 shows that the regional mean RMSE (7.4 days) is only 2.6 days larger than that of model fitting (4.8 days). Over the 1982–2011 period, the largest difference between observed and fitted/predicted SOS dates is 4.3 days (in 1985) and the mean error is −0.2 days. Thus, the *UniForc* model performs pretty well in simulating and predicting SOS dates in most parts of the research region (Fig. 8.2).

8.4 Predicting SOS Dates from 1950 to 2100

The pixel-specific *UniForc* models were employed to reconstruct SOS time series from 1950 to 2005 and predict SOS time series from 2006 to 2100 in the deciduous broadleaf forest region of northern China based on historical daily mean air temperature dataset (1950–2005) and daily mean air temperature dataset under RCP 4.5 and RCP 8.5 scenarios (2006–2100), respectively.

Regional mean SOS time series from 2006 to 2100 show a significantly advancing trend ($P < 0.01$). The advancement rates would be 0.65 days per decade under RCP 4.5 and 1.79 days per decade under RCP 8.5, respectively. By contrast, the significant advancement rates of regional mean SOS dates over the 1950–2100 period increase to 0.85 days per decade under RCP 4.5 but decrease to 1.45 days per decade under RCP 8.5 (Fig. 8.3).

The detailed temporal and spatial characteristics of SOS date can be revealed by computing decadal mean anomalies and decadal mean spatial standard deviations under the RCP 4.5 and RCP 8.5 scenarios over the 2006–2100 period across the deciduous broadleaf forest region (taking the mean SOS date during 1961–1990 as

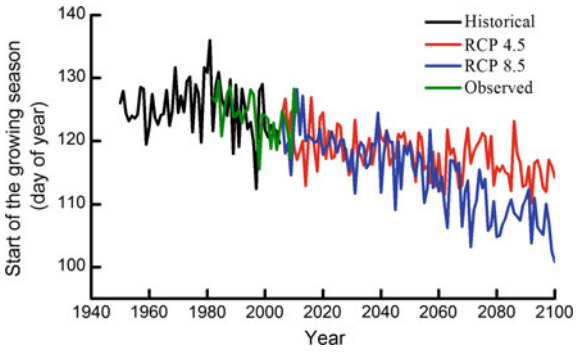

Fig. 8.3 Time series of growing season start date from 1950 to 2100, as predicted by calibrated output daily mean air temperature data from the regional climate model HadGEM3-RA in comparison with observed growing season start date over 1982–2011 across the deciduous broadleaf forest region [Reprinted from Luo et al. (2014), with permission from Elsevier]

the reference value). Because predicted SOS dates are available only from 2006 to 2010, the five-year mean anomaly and the five-year mean spatial standard deviation were calculated for the decade 2001–2010.

Table 8.1 shows that an overall advancement of SOS date would occur in each decade during 2006 and 2100, and the absolute values of the negative decadal mean anomalies under the RCP 8.5 scenario would be generally larger than those under the RCP 4.5 scenario with the exception during 2011–2020 and 2021–2030. In addition, the advancement amplitude of decadal mean SOS dates would increase overall with time. At the end of 21st century, the predicted regional mean SOS date under the RCP 4.5 and RCP 8.5 scenarios would be 11.8 and 20 days earlier than the regional mean SOS date during 1961–1990, respectively. Meanwhile, the spatial standard deviation of decadal mean SOS dates under the RCP 8.5 scenario would also increase with time during 2006–2100, whereas the spatial standard deviation of decadal mean SOS dates under the RCP 4.5 scenario would not indicate an obvious tendency. This finding is consistent with the conclusion from the correlation analysis between regional February-April mean air temperature and spatial standard deviation of the ground-based growing season beginning date across China's temperate zone from 1986 to 2005 (Fig. 5.5). Namely, regional air temperature increase would significantly enhance the spatial variability (measured by spatial standard deviation in days) of spring tree phenology and consequently accelerate the spatial response sensitivity of spring tree phenology to air temperature (in a spatial shift in phenological occurrence date caused by a spatial shift in mean air temperature by 1 °C, days $°C^{-1}$). Therefore, the spatial patterns of spring vegetation phenology under global warming would likely turn into more uncertain than at present (Chen and Xu 2012a).

Table 8.1 Decadal mean anomalies and decadal mean spatial standard deviations of growing season start date under the RCP 4.5 and RCP 8.5 scenarios during 2006–2100 across the deciduous broadleaf forest region (Luo et al. 2014)

Period	RCP 4.5		RCP 8.5	
	Anomaly[a] (days)	Spatial SD[b] (days)	Anomaly (days)	Spatial SD (days)
2006–2010	−3.4	11.2	−6.7	12.8
2011–2020	−6.6	12.4	−4.8	12.6
2021–2030	−8.1	12.6	−7.6	12.7
2031–2040	−7.3	12.4	−9.0	12.9
2041–2050	−7.2	12.7	−8.8	13.8
2051–2060	−9.8	12.8	−11.4	13.6
2061–2070	−10.0	13.2	−13.7	14.1
2071–2080	−8.4	12.5	−17.3	15.8
2081–2090	−10.8	13.2	−18.0	15.9
2091–2100	−11.8	13.6	−20.0	17.1

[a]The reference value is the regional mean growing season start date during 1961–1990
[b]Spatial standard deviation (SD) measures average variability of a spatial variable. In this research, the spatial variable is the SOS date at each pixel across the deciduous broadleaf forest region

Similar to regional mean SOS dates, SOS dates at each pixel show also an advancement in each decade during 2011–2100 under both RCP 4.5 and RCP 8.5 scenarios. Spatial patterns of the negative decadal mean anomalies display that the advancement amplitude of decadal mean SOS dates under the RCP 8.5 scenario would be larger in southern parts of the deciduous broadleaf forest region than in northern parts, whereas the advancement amplitude of decadal mean SOS dates under the RCP 4.5 scenario would not show such a latitudinal differentiation. Namely, decadal mean SOS dates would advance slower with the increase of latitude under the RCP 8.5 scenario (Fig. 8.4), which can be partially explained by the fact that the spring tree phenology sensitivity to air temperature (in days $°C^{-1}$) is stronger at warmer areas than at colder areas (Chen and Xu 2012b). Thus, an enhanced sensitivity of spring phenology response to air temperature would be expected under future climate warming, especially in colder areas or higher latitudes where the greatest climate warming is predicted (IPCC 2007).

Comparing the absolute values of decadal mean anomalies of the SOS date under the RCP 8.5 scenario with those under the RCP 4.5 scenario at the pixel level, the former would not always be larger than the latter. Nevertheless, the percent of pixels with larger advancing anomaly of the SOS date under the RCP 8.5 scenario would gradually increase with time. The number of pixels with larger advancing anomaly under the RCP 8.5 accounts for 7.8 % during 2011–2020 and 76.1 % during 2031–2040, and reaches 96.8 % during 2091–2100 (Fig. 8.4).

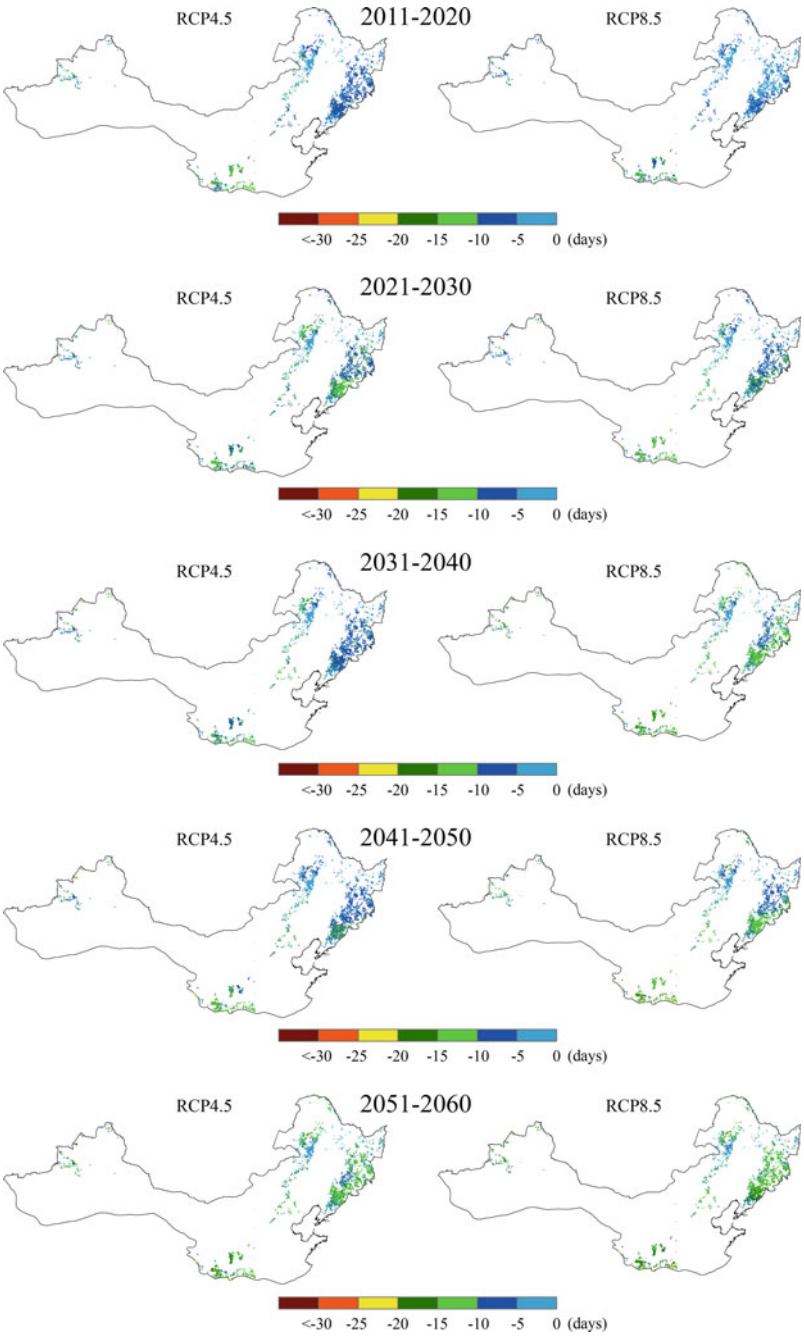

Fig. 8.4 Spatial patterns of decadal mean anomalies of growing season start date under RCP 4.5 and RCP 8.5 scenarios during 2011–2100. The reference value is the mean growing season start date during 1961–1990

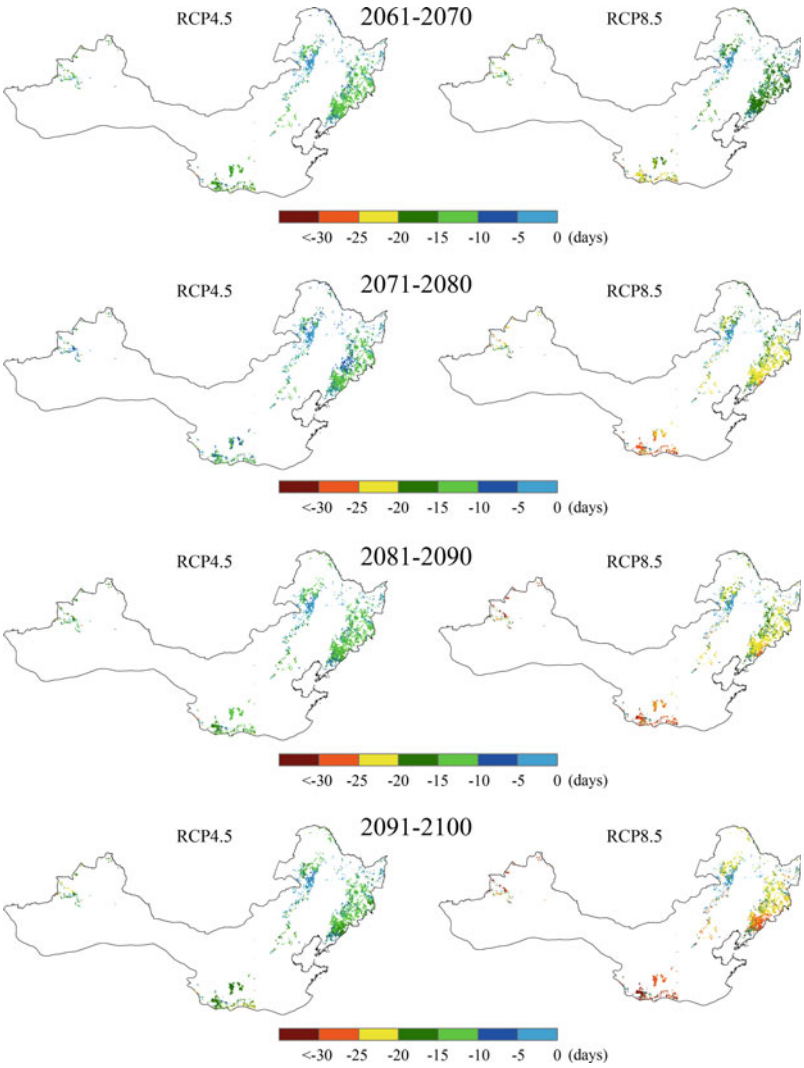

Fig. 8.4 (continued)

References

Chen XQ, Xu L (2012a) Temperature controls on the spatial pattern of tree phenology in China's temperate zone. Agric For Meteorol 154–155:195–202

Chen XQ, Xu L (2012b) Phenological responses of *Ulmus pumila* (Siberian Elm) to climate change in the temperate zone of China. Int J Biometeorol 56:695–706

Chuine I (2000) A unified model for budburst of trees. J. Theoret. Biol 207:337–347

Giorgi F, Jones C, Asrar GR (2009) Addressing climate information needs at the regional level: the CORDEX framework. WMO Bull 58:175–183

Hutchinson MF (2002) Anusplin Version 4.2 User Guide. Centre for Resource and Environmental Studies, Australian National University, Canberra

IPCC (2007) Climate change 2007: the physical science basis. In: Soloman S, Qin D, Manning M, Chen Z, Marquis M, Averyt KB, Tignor M, Miller HL (eds) Contribution of working group I to the fourth assessment report of the intergovernmental panel on climate change. Cambridge University Press, Cambridge, United Kingdom/New York, NY, USA

Luo XZ, Chen XQ, Wang LX, Xu L, Tian YH (2014) Modeling and predicting spring land surface phenology of the deciduous broadleaf forest in northern China. Agric For Meteorol 198–199:33–41

Riahi K, Rao S, Krey V, Cho C, Chirkov V, Fischer G, Kindermann G, Nakicenovic N, Rafaj P (2011) RCP 8.5: a scenario of comparatively high greenhouse gas emissions. Clim Change 109:33–57

Thomson AM, Calvin KV, Smith SJ, Kyle GP, Volke A, Patel P, Delgado-Arias S, Bond-Lamberty B, Wise MA, Clarke LE, Edmonds JA (2011) RCP4.5: a pathway for stabilization of radiative forcing by 2100. Clim Change 109:77–94

Xu L, Chen XQ (2013) Regional unified model-based leaf unfolding prediction from 1960 to 2009 across northern China. Global Change Biol 19:1275–1284

Chapter 9
Spatiotemporal Coupling Effects of Plant Phenology

Abstract From the geographic perspective, spatial differentiation among natural landscape units determines spatial flow and vice versa. Thus, spatial differentiation is not only the cause of natural landscape dynamics but also the result of natural landscape dynamics. As the integrative indicator of natural landscape dynamics at seasonal and interannual scales, spatial and temporal variations of plant phenology are mainly controlled by spatial and temporal variations of thermal and moisture conditions derived from changes of net radiation distributions and atmospheric movements. With regard to spatiotemporal unification of plant phenological variation, spatial movements of heat and moisture flows in each year, and their interannual and long-term changes induce spatial movements of plant phenology flows in each year, and their interannual and long-term dynamics. Spatial flow of phenological event occurrence dates across a region in a specific year demonstrates spatial patterns of phenological event occurrence dates in the year. Interannual shifts of the spatial flow make the spatial patterns vary from year to year, forming temporal variation of spatial patterns. Temporal flow of phenological event occurrence dates at a location during long period of time creates temporal patterns of phenological event occurrence dates at the location. Spatial shifts of the temporal flow make the temporal patterns vary from location to location, presenting spatial patterns of temporal variation. Thus, the temporal variations of spatial patterns of phenological event occurrence dates are converted to the spatial pattern of temporal variations of phenological event occurrence dates. Overall, the nearer the distance between two locations and the shorter the interval between two time slices or between two phenological events, the stronger the coupling and substitutability between spatial and temporal series.

Keywords Natural landscape dynamics · Spatial flow · Plant phenological variation · Temporal variation of spatial pattern · Spatial pattern of temporal variation · Scale conversion · Spatiotemporal unification · Spatiotemporal series substitutability

X. Chen, *Spatiotemporal Processes of Plant Phenology*,
SpringerBriefs in Geography, DOI 10.1007/978-3-662-49839-2_9

9.1 Causality of Natural Landscape Dynamics

Geography's relevance to science and society arises from a distinctive and integrating set of perspectives through which geographers view the world around them (National Research Council 1997). Physical geographic perspectives include mainly three aspects. First, physical geography looks at the natural landscape composition and structure through the lenses of spatial scale, such as location, place, region, and the whole world. Second, physical geography understands natural landscape heterogeneity through spatial differentiation, for instance latitudinal and vertical zonation of natural landscapes. Third, physical geography observes natural landscape dynamics through spatial flow, such as material flow, energy flow, and information flow. Generally speaking, past spatial differentiation, such as in air pressure, elevation, soil moisture and pollen release timing (among natural landscape units) triggers spatial flow, such as air flow (from high air pressure to low air pressure areas), water flow (from high elevation to low elevation areas), dust flow (from high air pressure and dry areas to low air pressure and humid areas) and pollen flow (from high air pressure and early flowering areas to low air pressure and late flowering areas), which are the concrete representations of interactions among different natural landscape units. The spatial flow has altered the past spatial differentiation among natural landscape units and generates the current spatial differentiation among natural landscape units. Similarly, spatial flow will also change the current spatial differentiation and produce the future spatial differentiation (Fig. 9.1). It should be noted that spatial differentiation and spatial flow manifest a continuous interaction process. Therefore, spatial differentiation among natural landscape units is not only the cause of natural landscape dynamics but also the result of natural landscape dynamics.

9.2 Spatiotemporal Unification of Plant Phenological Variation

As the integrative indicator of natural landscape dynamics at seasonal and interannual scales, spatial variations of plant phenology are commonly represented by spatial series of phenological event occurrence dates over a certain region within a particular time unit, such as a day, a month, or a year, while temporal variations of

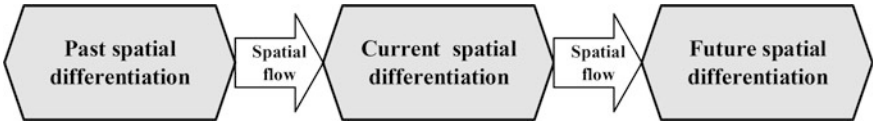

Fig. 9.1 Interaction between spatial differentiation and spatial flow

plant phenology are usually described by time series of phenological event occurrence dates at a specific natural landscape unit, such as a location, a place, or a region. It is well known that spatial differentiation of net radiation controls spatial patterns of air temperature and air pressure, which trigger horizontal and vertical atmospheric movement, and determine spatial patterns of precipitation. The spatial patterns of air temperature and precipitation change over time. Because spatial and temporal variations of plant phenology are mainly controlled by spatial and temporal variations of thermal and moisture conditions derived from changes of net radiation distributions and atmospheric movements, spatial and temporal patterns of plant phenology might be simulated and predicted by means of statistical and process-based models using spatial and temporal datasets of temperature and precipitation (Chen et al. 2005, 2014, 2015a, b; Chen and Xu 2012a, b; Xu and Chen 2013; Luo et al. 2014).

From the perspective of spatiotemporal scales, spatial variations during short period of time are the sections of spatial variation during long period of time, while spatial variation during long period of time is the superposition of spatial variations during short period of time. Spatial variations at different time scales might be unified through scale conversion, namely integration and differentiation. Similarly, temporal variations at small spatial scales form the basis of temporal variation at large spatial scales, while temporal variation at large spatial scales is the integration of temporal variations at small spatial scales. Temporal variations at different spatial scales might be unified through scale conversion, namely upscaling and downscaling. Considering spatiotemporal unification of plant phenological variation, spatial movements of heat and moisture flows (energy and material flows) in each year, and their interannual and long-term changes induce spatial movements of plant phenology flows (information flows) in each year, and their interannual and long-term dynamics. Generally, spatial flow of phenological event occurrence dates across a region in a specific year, such as from south to north and from low elevation to high elevation during spring and summer, or from north to south and from high elevation to low elevation during autumn and winter, demonstrates spatial patterns of phenological event occurrence dates in the year. Meanwhile, interannual shifts of the spatial flow make the spatial patterns vary from year to year (Fig. 7.2) and from decade to decade (Fig. 8.4), forming temporal variation of spatial patterns. If integrating the shorter period of time, such as a year into a longer period of time, spatial patterns of average phenological event occurrence dates can be obtained (Fig. 7.6). Temporal flow of phenological event occurrence dates at a location during long period of time creates temporal patterns of phenological event occurrence dates at the location, which can normally be portrayed by amplitudes, rhythms and trends of phenological time series. At the same time, spatial shifts of the temporal flow make the temporal patterns vary from location to location, presenting spatial patterns of temporal variation. Spatial differentiation of linear trends of local phenological time series can represent spatial patterns of overall phenological temporal variation (Fig. 6.3). That is, phenological time series at different locations have different temporal patterns. Thus, the temporal variations of spatial

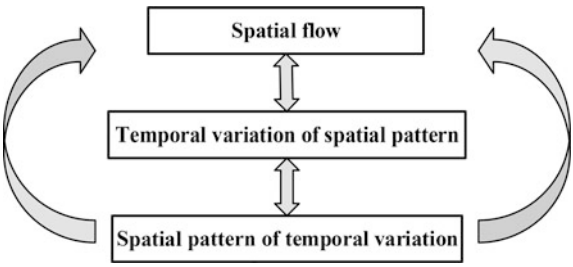

Fig. 9.2 Spatiotemporal unification flow chart of plant phenological variation

patterns of phenological event occurrence dates are converted to the spatial pattern of temporal variations of phenological event occurrence dates. It is worth pointing out that the conversions from spatial flow to temporal variation of spatial pattern, and from temporal variation of spatial pattern to spatial pattern of temporal variation are interacted. Finally, spatial pattern of temporal variation may also influence the speed and direction of spatial flows through feedback loops (Fig. 9.2).

9.3 Spatiotemporal Series Substitutability in Plant Phenology

As plant phenology has found renewal in the context of global climate change, there is an urgent need for predicting plant phenological occurrence dates at regional scales (Chuine et al. 2000). Therefore, regional unified models should be developed (Xu and Chen 2013). There are two types of approaches to create regional unified models for plant phenological simulation and prediction. The top-down approach assumes that model estimates of plant phenological response to climatic fluctuation for individual species are not significantly different at various stations within a similar climate region, based on which regional single species models and multispecies models were constructed by pooling phenological time series from different sample stations, for example, for flowering dates in Germany (Chen 1994) and Spain (García-Mozo et al. 2008), green-up dates in Inner Mongolia, China (see Chap. 6.3), and leaf coloring dates in France (Delpierre et al. 2009). This type of approach for constructing regional unified phenology models may neglect bioclimatic mechanisms. Since spatial phenological variations are not equivalent to temporal phenological variations, pooling time series from different stations is arbitrary, especially when time series length (number of years) are obviously shorter than spatial series length (number of stations), and phenological time series from multispecies and different stations were merged (García-Mozo et al. 2008; Delpierre et al. 2009). Thus, attempting this approach based on highly asymmetrical spatiotemporal datasets may hinder statistical and process-based phenological modeling. Contrarily, the bottom-up approach tries to select the most robust local

species-specific model in predicting the phenological occurrence dates at all external stations within a similar climate region as the regional unified species-specific model in the climate region (Xu and Chen 2013). Obviously, the latter approach may be more rational and reliable. Nevertheless, the former approach can also be more effective when used under the condition of spatiotemporal series substitutability, which can be generally described as follows:

(1) For time series across spatial scales, the temporal consistency of a phenological event between two locations decreases generally with the increasing distance. That is, the nearer the distance between two locations, the more similar the temporal variation causes and the stronger the substitutability between time series, whereas the farther the distance between two locations, the more dissimilar the temporal variation causes and the weaker the substitutability between time series. Therefore, principal characteristics of plant phenological temporal variation and its responses to climate change at regional scales can be captured by phenological and climatic time series at a few representative locations (Xu and Chen 2013).

(2) For spatial series across time scales, the spatial inheritance of a phenological event between two time slices decreases generally with the lengthening interval. Namely, the shorter the interval between two time slices, the more similar the spatial variation causes and the stronger the substitutability between spatial series, whereas the longer the interval between two time slices, the more dissimilar the spatial variation causes and the weaker the substitutability between spatial series. Thus, the main features of plant phenological spatial variation and its climatic controls over the entire time period can be determined by phenological and climatic spatial series at several typical time slices (Chen and Wang 2009).

(3) For time series across time scales, the temporal synchronism between two phenological events at a location decreases generally with the lengthening interval between them. That is to say that the shorter the interval between the two phenological events, the more similar the temporal variation causes and the stronger the substitutability between the two time series, whereas the longer the interval between the two phenological events, the more dissimilar the temporal variation causes and the weaker the substitutability between the two time series. So, temporal variation of a phenological event and its responses to seasonally climatic variability at a location can be replaced by time series of another phenological event with highly sequential and correlative rhythm at the location (Chap. 2.1).

(4) Overall, the nearer the distance between two locations and the shorter the interval between two time slices or between two phenological events, the stronger the coupling and substitutability between spatial and temporal series, while the farther the distance between two locations and the longer the interval between two time slices or between two phenological events, the weaker the coupling and substitutability between spatial and temporal series.

References

Chen XQ (1994) Untersuchung zur zeitlich-räumlichen Ähnlichkeit von phänologischen und klimatologischen Parametern in Westdeutschland und zum Einfluß geoökologischer Faktoren auf die phänologische Entwicklung im Gebiet des Taunus. Selbstverlag des Deutschen Wetterdienstes, Offenbach am Main

Chen XQ, Wang H (2009) Spatial and temporal variations of vegetation belts and vegetation cover degrees in Inner Mongolia from 1982 to 2003 (in Chinese with English abstract). Acta Geographica Sinica 64(1):84–94

Chen XQ, Xu L (2012a) Phenological responses of *Ulmus pumila* (Siberian Elm) to climate change in the temperate zone of China. Int J Biometeorol 56:695–706

Chen XQ, Xu L (2012b) Temperature controls on the spatial pattern of tree phenology in China's temperate zone. Agric For Meteorol 154–155:195–202

Chen XQ, Hu B, Yu R (2005) Spatial and temporal variation of phenological growing season and climate change impacts in temperate eastern China. Global Change Biol 11(7):1118–1130

Chen XQ, Li J, Xu L, Liu L, Ding D (2014) Modeling greenup date of dominant grass species in the Inner Mongolian Grassland using air temperature and precipitation data. Int J Biometeorol 58:463–471

Chen XQ, An S, Inouye D, Schwartz MD (2015a) Temperature and snowfall trigger alpine vegetation green-up on the world's roof. Global Change Biol 21:3635–3646

Chen XQ, Tian YH, Xu L (2015b) Temperature and geographic attribution of change in the *Taraxacum mongolicum* growing season from 1990 to 2009 in eastern China's temperate zone. Int J Biometeorol 59:1437–1452

Chuine I, Cambon G, Comtois P (2000) Scaling phenology from the local to the regional level: advances from species-specific phenological models. Global Change Biol 6:943–952

Delpierre N, Dufrêne E, Soudani K, Ulrich E, Cecchini S, Boé J, François C (2009) Modelling interannual and spatial variability of leaf senescence for three deciduous tree species in France. Agric For Meteorol 149:938–948

García-Mozo H, Chuine I, Aira MJ, Belmonte J, Bermejo D, Díaz de la Guardia C, Elvira B, Gutiérrez M, Rodríguez-Rajo J, Ruiz L, Trigo MM, Tormo R, Valencia R, Galán C (2008) Regional phenological models for forecasting the start and peak of the *Quercus* pollen season in Spain. Agric For Meteorol 148:372–380

Luo XZ, Chen XQ, Wang LX, Xu L, Tian YH (2014) Modeling and predicting spring land surface phenology of the deciduous broadleaf forest in northern China. Agric For Meteorol 198–199:33–41

National Research Council (1997) Rediscovering geography: new relevance for science and society. National Academy Press, Washington DC, pp 28–29

Xu L, Chen XQ (2013) Regional unified model-based leaf unfolding prediction from 1960 to 2009 across northern China. Global Change Biol 19:1275–1284

Index

X. Chen, *Spatiotemporal Processes of Plant Phenology*,
SpringerBriefs in Geography, DOI 10.1007/978-3-662-49839-2